

# Underwater Wireless Video Transmission using Acoustic OFDM

Jordi Ribas, Massachusetts Institute of Technology  
E-mail: ribas@mit.edu

Advisor: Milica Stojanovic, Northeastern University  
E-mail: millitsa@ece.neu.edu

December 27, 2009



# Contents

<b>1</b>	<b>Introduction</b>	<b>19</b>
1.1	Background . . . . .	19
1.2	Approach . . . . .	20
1.3	Objectives . . . . .	20
1.4	Project workplan . . . . .	21
<b>2</b>	<b>The underwater channel</b>	<b>23</b>
2.1	Acoustic propagation . . . . .	23
2.1.1	Attenuation . . . . .	23
2.1.2	Noise . . . . .	24
2.1.3	Propagation delay . . . . .	26
2.1.4	Multipath . . . . .	26
2.1.5	Doppler effect . . . . .	27
2.2	Resource allocation . . . . .	27
2.2.1	The AN product and the SNR . . . . .	27
2.2.2	Optimal frequency . . . . .	27
2.2.3	3 dB bandwidth definition . . . . .	28
2.2.4	Transmission power . . . . .	28
<b>3</b>	<b>Video compression techniques</b>	<b>31</b>
3.1	Compression fundamentals . . . . .	31
3.1.1	Images and video . . . . .	31
3.1.2	Compression approaches . . . . .	33
3.2	MPEG-4 standard . . . . .	35
3.2.1	Functionalities . . . . .	35
3.2.2	Very Low Bit-rate Video core . . . . .	35
3.3	Implementation . . . . .	36
3.3.1	MPEG-4 codec . . . . .	36
3.3.2	Performance . . . . .	36
<b>4</b>	<b>OFDM fundamentals</b>	<b>39</b>
4.1	General description . . . . .	39
4.2	Orthogonality . . . . .	40
4.3	Modulation using FFT . . . . .	41
4.4	Guard time . . . . .	41
4.5	Equalization . . . . .	42
4.6	Advantages . . . . .	42
4.7	Disadvantages . . . . .	42

<b>5 OFDM transmitter</b>	<b>43</b>
5.1 System model . . . . .	43
5.2 Transmitter implementation . . . . .	44
5.2.1 Scrambling . . . . .	44
5.2.2 FEC coding . . . . .	45
5.2.3 Subcarrier mapping . . . . .	47
5.2.4 Frequency interleaving . . . . .	48
5.2.5 IFFT modulation . . . . .	50
5.2.6 Peak to Average Ratio reduction . . . . .	50
5.2.7 Synchronization and guard time . . . . .	56
5.2.8 Frequency adjustment . . . . .	58
<b>6 OFDM receiver</b>	<b>61</b>
6.1 Receiver design . . . . .	61
6.2 FIR filtering . . . . .	62
6.3 Time synchronization . . . . .	62
6.4 FFT demodulation . . . . .	64
6.5 Detection . . . . .	65
6.5.1 Differentially coherent detector . . . . .	65
6.5.2 Coherent detector . . . . .	67
6.6 Performance analysis . . . . .	72
6.6.1 MSE . . . . .	72
6.6.2 Bit and Symbol Error Rates . . . . .	73
<b>7 System deployment</b>	<b>77</b>
7.1 Air tests . . . . .	77
7.1.1 Deployment . . . . .	77
7.1.2 Hardware . . . . .	78
7.1.3 OFDM parameters . . . . .	79
7.2 Underwater tests . . . . .	79
7.2.1 Deployment . . . . .	79
7.2.2 Hardware . . . . .	81
7.2.3 OFDM parameters . . . . .	83
<b>8 Experimental results</b>	<b>85</b>
8.1 Simulation tests . . . . .	85
8.1.1 Description . . . . .	85
8.1.2 Subcarrier modulations . . . . .	86
8.1.3 Distances . . . . .	86
8.2 Air tests . . . . .	90
8.2.1 Multipath . . . . .	90
8.2.2 Motion . . . . .	91
8.2.3 Multiple receivers . . . . .	93
8.3 Underwater tests . . . . .	95
8.3.1 Video detection . . . . .	95
8.3.2 FEC coding . . . . .	95
8.3.3 Subcarrier modulations . . . . .	96
8.3.4 Distances . . . . .	98
8.3.5 Consistency . . . . .	99
<b>9 Conclusions and future work</b>	<b>103</b>
<b>Appendices</b>	<b>107</b>

<b>A User's manual</b>	<b>107</b>
A.1 WAV Generator . . . . .	107
A.1.1 GUI . . . . .	107
A.1.2 Parameters . . . . .	107
A.1.3 Output . . . . .	109
A.1.4 Channel simulator . . . . .	110
A.2 WAV Receiver . . . . .	110
A.2.1 GUI . . . . .	111
A.2.2 Parameters . . . . .	111
A.2.3 Output . . . . .	113
A.3 WAV Plotter . . . . .	114
A.3.1 GUI . . . . .	114
A.3.2 Parameters . . . . .	117
A.3.3 Output . . . . .	117



# List of Figures

1.1	Problem statement . . . . .	21
2.1	Absorption coefficient as a function of frequency . . . . .	24
2.2	Power spectral density of the ambient noise, $N(f)$ [dB re $\mu$ Pa]. The dash-dot line shows the approximation 2.5 . . . . .	25
2.3	Multipath effects. Reflective effects (dashed line) and refractive effects (dotted line) . . . . .	26
2.4	Frequency-dependent part of the SNR, $1/A(l, f)N(f)$ . Practical spreading, $k = 1.5$ , is used for the path loss $A(l, f)$ . The linear approximation is used for the noise p.s.d. $N(f)$ . . . . .	28
2.5	Optimal frequency $f_0(l)$ considering the inverse of the AN product, $1/A(l, f)N(f)$ . The 3 dB bandwidth, $B_{3dB}(l)$ , and the center frequency of this bandwidth, $f_c(l)$ , is also shown . . . . .	29
2.6	Required transmission power for quiet measurements in an oil field . . . . .	30
3.1	Image pixels . . . . .	32
3.2	YUV image representation. (1) Original signal. (2) Luminance Y signal. (3) Chrominance V signal. (4) Chrominance U signal . . . . .	32
3.3	Consecutive images of a video file . . . . .	33
3.4	Division of the image into blocks . . . . .	33
3.5	Image (left) and DCT basis (right) . . . . .	34
3.6	Temporal coding transmission scheme . . . . .	34
3.7	Group Of Pictures (GOP) . . . . .	34
3.8	Hybrid temporal-spatial coding basic scheme . . . . .	35
3.9	Classification of the MPEG-4 image and video coding algorithms and tools . . . . .	36
3.10	Lower quality video (left) and higher quality video (right) . . . . .	36
4.1	Bandwidth utilization for an OFDM signal . . . . .	40
4.2	Efficient transmitter implementation using IFFT . . . . .	41
5.1	Transmitter scheme . . . . .	44
5.2	Scrambler scheme . . . . .	45
5.3	Scrambling effect on PAR reduction: (left) OFDM sample block with non-scrambled bits, and (right) OFDM sample block with scrambled bits . . . . .	45
5.4	Decoded BER vs. SNR for an OFDM system with $K=16384$ , 8-PSK subcarrier modulation, and AWGN . . . . .	47
5.5	PSK modulation constellations . . . . .	48
5.6	QAM modulation constellations . . . . .	48
5.7	Interleaving concept. The data carriers are shown in different colors and the $P$ channels represent pilots . . . . .	49
5.8	Interleaving matrix and interleaving depth . . . . .	49
5.9	PAR reduction idea: original OFDM signal (left), and PAR reduced OFDM signal (right), using the symbol interleaving technique . . . . .	51
5.10	Clipping and filtering block diagram . . . . .	52
5.11	Symbol interleaving technique . . . . .	53
5.12	Interleaver detection. Normalized MSE with $M=32$ interleavers (8-PSK, $K=16384$ ) . . . . .	54

5.13	In-band tone reservation concept. The control tones are circled and marked with a "T" . . . . .	54
5.14	Out of band tone insertion (OTI) block diagram . . . . .	55
5.15	Power Spectral Density (p.s.d.) of an OFDM signal with random OTI . . . . .	55
5.16	CCDF of an OFDM signal for different PAR techniques (8-PSK, $K=16384$ , $B=115$ kHz) . . . . .	57
5.17	Synchronization preamble (left), and its autocorrelation (right) . . . . .	57
5.18	Transmitted time domain signal (top left), received time domain signal (bottom left), transmitted frequency domain signal (top right), and received frequency domain signal (bottom right) . . . . .	58
5.19	OFDM signal p.s.d. ( $K=16384$ , 8-PSK, $B=115$ kHz) before frequency adjustment (left) and after (right) . . . . .	59
5.20	Sample transmitted OFDM signal with $K=16384$ , 8-PSK, and $B=115$ kHz. Synchronization preamble and OFDM blocks . . . . .	59
6.1	Receiver scheme . . . . .	61
6.2	Power spectral density (p.s.d.) of the received signal and the FIR filter response ( $B=115$ kHz). The vertical axis indicates the signal power related to the maximum power in dB . . . . .	63
6.3	Received signal before filtering (top), and after filtering (bottom) with $B=115$ kHz, 8-PSK, $K=16384$ . . . . .	63
6.4	Synchronization preamble followed by a pause (top), received signal after filtering used as the input of the synchronization algorithm (center), and cross-correlation between preamble and signal (bottom). OFDM parameters: $B=115$ kHz, 8-PSK, $K=16384$ . . . . .	64
6.5	Constellation after FFT demodulation. Link: 200m, underwater. OFDM parameters: $B=115$ kHz, 8-PSK, $K=16384$ . . . . .	65
6.6	Differential encoded QPSK constellation (left) and 8-PSK constellation (right) . . . . .	66
6.7	Detected constellation (left) and decided values (right) with differential detection. OFDM parameters: $B=115$ kHz, 8-PSK, $K=16384$ . . . . .	67
6.8	Constellation after FFT (left), and $\hat{d}_{k1}$ estimates (right) for an OFDM signal with $K=16384$ , $B=115$ kHz, and 8-PSK subcarrier modulation . . . . .	68
6.9	$\hat{a}$ estimates for an OFDM signal with $K=16384$ , $B=115$ kHz, and 8-PSK subcarrier modulation . . . . .	69
6.10	$\hat{\theta}_k$ estimates in radians for an OFDM signal with $K=16384$ , $B=115$ kHz, and 8-PSK subcarrier modulation. The plot includes the estimates for $k=0$ , $k=8191$ and $k=16383$ . . . . .	69
6.11	$\hat{d}_{k1}$ estimates (left) and phase corrected $\hat{d}_k$ estimates (right) for an OFDM signal with $K=16384$ , $B=115$ kHz, and 8-PSK subcarrier modulation . . . . .	69
6.12	Phase-corrected $\hat{d}_k$ estimates (left) and symbol decisions (right) for an OFDM signal with $K=16384$ , $B=115$ kHz, and 8-PSK subcarrier modulation . . . . .	70
6.13	Channel frequency-domain estimates $\mathbf{X}_k$ for an OFDM signal with $K=16384$ , $B=115$ kHz, and 8-PSK subcarrier modulation . . . . .	71
6.14	Channel time-domain estimates $\mathbf{x}_l$ (left) and truncated coefficients $\tilde{\mathbf{x}}_l$ (right) for an OFDM signal with $K=16384$ , $B=115$ kHz, and 8-PSK subcarrier modulation . . . . .	71
6.15	Channel updated time-domain estimates $\hat{\mathbf{h}}_l$ (left) and final frequency-domain estimates $\hat{\mathbf{H}}_k$ (right) for an OFDM signal with $K=16384$ , $B=115$ kHz, and 8-PSK subcarrier modulation . . . . .	72
6.16	MSE concept. Detected symbols before decision, $\hat{d}_k$ (grey stars), and transmitted symbols, $d_k$ (blue circles) . . . . .	73
6.17	MSE-time in dB (8-PSK subcarrier modulation, $K=16384$ , BCH(63,18), $B=115$ kHz) . . . . .	73
6.18	MSE-frequency in dB (8-PSK subcarrier modulation, $K=16384$ , BCH(63,18), $B=115$ kHz) . . . . .	74
6.19	Coded sequence BER (left) and decoded sequence BER (right). The black solid line represents the mean BER. OFDM parameters: 8-PSK subcarrier modulation, $K=16384$ , BCH(63,18), $B=115$ kHz . . . . .	74
6.20	SER-time (left) and SER-frequency (right). The black solid line represents the mean SER. OFDM parameters: 8-PSK subcarrier modulation, $K=16384$ , BCH(63,18), $B=115$ kHz . . . . .	75
7.1	System model . . . . .	77
7.2	Air tests transmission block diagram . . . . .	78
7.3	Air tests reception block diagram . . . . .	78

7.4	Underwater tests transmission block diagram . . . . .	80
7.5	Underwater tests reception block diagram . . . . .	80
7.6	Underwater tests deployment . . . . .	81
7.7	Power response of the PA50 APEX power amplifier . . . . .	82
7.8	Directivity pattern (left) and Transmitting Voltage Response (TVR) (right) of the ITC-1042 transducer . . . . .	82
7.9	Horizontal directivity pattern (left) and receiving sensitivity (right) of the Reson TC4032 hydrophone . . . . .	83
7.10	High-pass filter (left) and low-pass filter (right) frequency responses of the Reson VP2000 preamplifier . . . . .	83
8.1	Simulator. Block diagram . . . . .	86
8.2	Simulated PSK constellations at 400 m. QPSK (left), and 8-PSK (right) . . . . .	87
8.3	Simulated QAM constellations at 400 m. 16-QAM (left), 32-QAM (center), and 64-QAM (right) . . . . .	87
8.4	MSE-time for different modulation types at 400 m . . . . .	87
8.5	Coded sequence time BER for different modulation types at 400 m . . . . .	88
8.6	8-PSK constellations for 200 m (left), 400 m (center), and 600 m (right) . . . . .	88
8.7	MSE-time for different distances . . . . .	89
8.8	Time BER for different distances . . . . .	89
8.9	Chanel time-domain estimates (left) and experiment layout (right) . . . . .	90
8.10	Phase estimates in radians for $k=0$ , $k=511$ and $k=1023$ (left) and experiment layout (right), with moderated motion and coherent detection . . . . .	91
8.11	Coded sequence time BER (left) and decoded sequence time BER (right), with moderated motion and coherent detection . . . . .	92
8.12	Phase estimates in radians for $k=0$ , $k=511$ and $k=1023$ (left) and experiment layout (right), with fast motion and coherent detection . . . . .	92
8.13	Decoded sequence time BER, with fast motion and coherent detection . . . . .	92
8.14	Decoded sequence time BER (left) and experiment layout (right), with fast motion and differential detection . . . . .	93
8.15	MSE-time in dB (left) and coded sequence time BER (right) with static conditions . . . . .	94
8.16	MSE-time in dB (left) and decoded sequence time BER (right) with fast motion conditions . . . . .	94
8.17	Sample image detection. BER=0% (left), BER=0.12% (center), and BER=1.17% (right) . . . . .	95
8.18	Decoded sequence time BER for different BCH codes . . . . .	96
8.19	PSK constellations at 200 m with coherent detection. QPSK (left), and 8-PSK (right) . . . . .	96
8.20	QAM constellations at 200 m with coherent detection. 16-QAM (left), 32-QAM (center), and 64-QAM (right) . . . . .	97
8.21	MSE-time in dB for different modulation types at 200 m . . . . .	97
8.22	Coded sequence time BER (left) and decoded sequence time BER (right) for different modulation types at 200 m . . . . .	98
8.23	Average SNR in dB vs. frequency for different transmitter-receiver distances . . . . .	98
8.24	MSE-time in dB for different transmitter-receiver distances . . . . .	99
8.25	Time BER for different transmitter-receiver distances . . . . .	100
8.26	MSE-time in dB for 25 consecutive video transmissions . . . . .	100
8.27	Time BER for 25 consecutive video transmissions . . . . .	101
A.1	WAV Generator GUI . . . . .	108
A.2	Sample <i>sep_tx</i> directory after wavefile generation . . . . .	110
A.3	Sample <i>sep_rx</i> directory after channel simulation . . . . .	111
A.4	WAV Receiver GUI . . . . .	112
A.5	Synchronization plot . . . . .	114
A.6	Detection results (left) and channel estimates (right) . . . . .	115
A.7	MSE results (left) and error performance (right) . . . . .	115
A.8	Sample <i>results</i> directory after detection and saving . . . . .	115
A.9	WAV Plotter GUI . . . . .	116

## LIST OF FIGURES

---

A.10 Plotted OFDM signals . . . . .	118
-------------------------------------	-----

# List of Tables

3.1	Frame rate study . . . . .	37
3.2	OFDM system parameters . . . . .	37
5.1	BCH coding characteristics . . . . .	46
5.2	Clipping and filtering parameters . . . . .	52
6.1	Filter parameters . . . . .	62
7.1	OFDM signal parameters used for the experiment ( $B = 11.025\text{kHz}$ , $Tg = 10\text{ms}$ ) . . . . .	79
7.2	Data bit rates with 1024 subcarriers (in $\text{kbps}$ ) . . . . .	79
7.3	OFDM signal parameters used for the experiment ( $B = 115\text{kHz}$ , $Tg = 10\text{ms}$ ) . . . . .	84
7.4	Data bit rates with 8192 and 16384 subcarriers (in $\text{kbps}$ ) . . . . .	84
8.1	Multipath study . . . . .	90
A.1	WAV Generator input parameters . . . . .	108
A.2	WAV Receiver input parameters . . . . .	111
A.3	WAV Plotter input parameters . . . . .	117



# Acknowledgements

I would like to specially thank the people who have made the experience of working on my Master's thesis at MIT possible. First of all, I would like to mention my professors in my home university, Universitat Politècnica de Catalunya (UPC), without whom I would not have been able to come to MIT. Secondly, but not less important, Prof. Milica Stojanovic and Prof. Chryssostomos Chryssostomidis, who invited me to carry out the research at the MIT Sea Grant College Program. More than that, Prof. Milica Stojanovic, my thesis' advisor, guided me through the research part of the work. I want to thank her for all the constructive discussions and e-mail messages.

Regarding the practical part of the work, none of the successful experiments would have been possible without the invaluable help of Daniel Sura, mechanical and ocean engineer at the MIT Sea Grant College Program, who selected and set up the underwater hardware, and was a key participant in all the underwater experiments. In addition, I want to thank Rameez Ahmed, graduate student at Northeastern University, for his help with the in-air testbed hardware, and for his help with the exciting experiments.

With reference to the amazing personal experience in Boston, I would like to thank all the people that have made of it an unforgettable period of my life: thanks to all the labmates, roommates, and friends I have made during these months. I would also like to mention here the assistants at the MIT Sea Grant College Program Janice Ahern, Trudi Walters and Nancy Adams, for the help and answers to my many questions.

And last but not least, I would like to give a special thanks to all my family, specifically my parents and my sister, who supported me from the beginning of my stay at MIT through endless Skype calls, either in the good or in the bad moments.



# Resumen

El objetivo principal del proyecto es el diseño y la implementación de un sistema acústico OFDM para transmisiones de vídeo submarinas. El trabajo de la tesis combina una parte teórica, cuyo objetivo es el de escoger las técnicas apropiadas para tratar las características del canal submarino, y una parte práctica, que incluye el desarrollo del sistema y las pruebas experimentales.

La investigación teórica se ha dividido en los siguientes puntos: (1) técnicas de compresión de vídeo, (2) técnicas de modulación y detección de señales OFDM, (3) algoritmos para estimación de canal, y (4) técnicas de reducción de la relación potencia de pico a potencia media (PAR, del inglés Peak to Average Ratio) para señales OFDM.

En cuanto a (1), la técnica de compresión estándar MPEG-4 ha sido seleccionada. Específicamente, los métodos para compresión de vídeo para bit rate reducido (Very Low Bit-rate Video, VLBV), proveen algoritmos y técnicas para aplicaciones operando entre 5 y 64 kbps, soportando secuencias de imágenes con baja resolución espacial (típicamente hasta resoluciones CIF) y bajo frame rate (típicamente hasta 15 Hz).

En referencia a (2), las técnicas escogidas han sido un detector coherente para canales acústicos submarinos llamado *Low complexity OFDM detector for underwater acoustic channels* (detector OFDM de baja complejidad para canales acústicos submarinos) y un detector diferencial. El primer algoritmo asume una dependencia bloque a bloque y ha sido demostrado inapropiado para situaciones con alta aceleración y modificación rápida del canal, de manera que el segundo algoritmo ha sido diseñado para eliminar esta dependencia y combatir los canales con rápida variación.

Sobre (3), la decisión ha recaído en la utilización de un algoritmo de reducción de la varianza del ruido, conocido como *Sparse channel estimation*, y que se puede traducir como estimación de canal reducido. La idea principal que permite la implementación de tal técnica en el presente contexto es que la respuesta del canal en el dominio temporal para canales acústicos submarinos es generalmente corta y, de esta manera, algunas muestras de la respuesta estimada pueden ser truncadas en el receptor para reducir ruido.

En cuanto a las técnicas de reducción de PAR (4), éstas tienen como objetivo reducir la relación potencia de pico a potencia media de la señal para evitar grandes variaciones de amplitud en el dominio temporal, de modo que se consigue un mejor uso de la potencia disponible (uno de los principales problemas de los sistemas OFDM), y se mejora la operación de los circuitos de amplificación en el transmisor. Las técnicas utilizadas incluyen: recorte y filtrado de la señal OFDM, entrelazado de símbolos, reserva de tonos dentro de banda, e inserción de tonos fuera de banda.

La parte práctica del proyecto consiste en la implementación de las técnicas seleccionadas y los siguientes grupos de experimentos: simulaciones software, experimentos en aire, y tests submarinos.

El sistema OFDM implementado ha sido desarrollado en MATLAB debido a las ventajas que esta aplicación ofrece para el depurado del programa, el ajuste de ciertos parámetros, y el análisis de resultados. Los scripts de MATLAB generan un fichero con la señal a transmitir por el hardware (desde un ordenador),

## RESUMEN

---

usando una plataforma para la creación de radios definidas por software (Software Defined Radio, SDR), que permite el uso de scripts programados en Python. Tan pronto el script complementario recibe y guarda la señal en el ordenador del receptor, otro conjunto de scripts MATLAB demodula y detecta los datos.

Los principales componentes hardware que han sido utilizados durante los experimentos con el banco de pruebas en aire incluyen un altavoz, un micrófono, el sistema de adquisición de datos, y dos ordenadores portátiles. Los principales componentes necesarios para los experimentos submarinos son el transductor y el hidrófono, el sistema de adquisición de datos, y dos ordenadores portátiles. Vídeos sin compresión han sido utilizados para la aplicación de la técnica MPEG-4 antes de su transmisión.

Las simulaciones desarrolladas tienen como objetivo probar la correcta implementación de todos los algoritmos mediante la combinación de la señal OFDM generada con un canal simulado y algoritmos de adición de ruido, que artificialmente introducen en la señal algunos de los efectos presentes en el canal real.

Los experimentos en aire tienen como intención probar el sistema mediante la adición de otros efectos del canal real, tales como el movimiento, y confirmar que el comportamiento de los algoritmos es el esperado. Además, se persigue una comparación entre las condiciones en aire y las condiciones submarinas.

Por último, los experimentos submarinos han sido desarrollados para finalmente probar la utilidad de las técnicas MPEG-4 para compresión, combinadas con los sistemas de modulación OFDM para transmitir vídeos con alto bit-rate. Los límites del sistema han sido alcanzados mediante el aumento de la distancia de transmisión, y la prueba de diferentes parámetros para el sistema OFDM.

Un bit rate útil de 151 kbps ha sido conseguido con buenas condiciones del canal, y 91 kbps ha sido el límite en otro caso. Ambos valores son suficientes para la transmisión de vídeos de baja calidad en tiempo real, con frame rates de entre 4 y 20 fps, dependiendo de la resolución y de la relación de compresión de la técnica MPEG-4.

# Abstract

The current project aims to design and implement an acoustic OFDM system for underwater video transmissions. The thesis work combines a theoretical part, whose objective is to choose the appropriate techniques to deal with the characteristics of the targeted channel, and a practical part regarding the system deployment and experimental tests.

The theoretical research has focused on (1) video compression techniques, (2) OFDM modulation and detection techniques, (3) channel estimation algorithms, and (4) Peak to Average Ratio (PAR) reduction techniques for OFDM signals.

Considering (1), the standard MPEG-4 compression technique has been chosen. Specifically, the Very Low Bit-rate Video (VLBV) layer provides algorithms and tools for applications operating at bit rates typically between 5 and 64 kbps, supporting image sequences with low spatial resolution (typically up to CIF resolution) and low frame rates (typically up to 15 Hz).

About (2), the chosen techniques have been a coherent detector for underwater acoustic channels, known as *Low complexity OFDM detector for underwater acoustic channels*, and a differential detector. The first algorithm has a block by block dependency and has proved to be inappropriate in situations with high acceleration and channel change over time, so the second algorithm has been designed to eliminate this dependency to deal with fast varying channels.

In the realm of (3), the decision has been to use a noise variance reducing algorithm, known as *Sparse channel estimation*. The main idea that allows the implementation of such technique in the current context is that the channel response in the time domain for underwater acoustic channels is proved to be generally sparse and, as a result, some samples of the estimated response on the receiver side can be truncated to reduce the noise.

The PAR reduction techniques (4) aim at reducing the peak to average power ratio of the signal to avoid spikes in the time domain, so as to make a better use of the power (which is one of the main problems of the OFDM systems) and better operate the amplifying circuitry on the transmitter side. The techniques that have been used include the following: clipping and filtering of the OFDM signal, symbol interleaving, in band tone reservation, and out of band tone insertion.

The practical part of the project consists of the implementation of the selected techniques, and the following sets of experiments: software simulations, in-air experiments, and underwater tests.

The implemented OFDM system has been developed in MATLAB due to the advantages that this application has in order to debug the program, tune the chosen parameters, and analyze results. The MATLAB scripts generate a wavefile which then is transmitted to the hardware from a laptop, using a Software Defined Radio (SDR) platform that allows the use of scripts programmed in Python. Once the complementary script records the wave on the receiving laptop from the receiving side hardware, another set of MATLAB scripts demodulate and detect the data.

## ABSTRACT

---

The key hardware components that have been used during the in-air testbed experiments include a speaker, a microphone, the data acquisition system, and two laptop computers. The main components needed for the underwater experiments are the transducer and the hydrophone, the data acquisition system and two laptop computers. Raw videos have been compressed using the MPEG-4 technique prior to transmission.

The simulations that have been performed aim at proving the correct implementation of all the algorithms by coupling the generated OFDM signal to a channel simulation and noise addition algorithm, that artificially introduces some of the real channel effects into the signal.

The in-air experiments' goal is to further test the system by adding other real channel effects, such as motion, and confirming that the algorithm performance is the expected. In addition, a comparison between the in-air conditions and the underwater ones is pursued.

Finally, the underwater experiments have been performed to finally prove the usefulness of the coupled MPEG-4 compression and OFDM modulation system to convey high data rates for video transmissions. The limits of the system have been reached by increasing the transmission distance and trying different sets of parameters for the OFDM system.

A data rate of 151 kbps has been achieved in good channel conditions, and 91 kbps has been the limit otherwise. Both bit rates are sufficient to allow the transmission of real-time low quality video, at frame rates between 4 and 20 fps depending on the resolution and the MPEG-4 compression ratio.

# Chapter 1

## Introduction

### 1.1 Background

The early efforts at transmitting digital video from remote underwater sites include those by the Japanese scientists, who succeeded in showing a crab crawling at a depth of 1,000 m in an ocean trench [1]. This video was in fact a sequence of independent images, played at about one image every 10 seconds (enough to demonstrate the technology of the day). The frame rate of only a few frames every 10 seconds is not sufficient to capture an arbitrary video, but it may be quite sufficient to capture a remote ocean-floor scene such as that of a slowly crawling animal.

Since the time when this was reported (about a decade ago) progress has been made on both fronts: video compression, which enables transmission of full-resolution video at a much lower bit rate, and acoustic communications and signal processing, which enable the transmission of digital signals at a much greater bit rate and through channels that are much more challenging than the stable vertical link.

In the realm of video compression, the last years have witnessed a proliferation of compression methods that support video transmission at bit rates as low as 64 kbps, and even lower. While 64 kbps corresponds to a standardized MPEG-4 technology, bit rates lower than this have been demonstrated, albeit without the same rigorous quality as that guaranteed by the 64 kbps rate. Today, these methods are commercially available in software, and ready to use.

Another approach to conveying a moving picture is by mosaicing, i.e. piecing together the images transmitted from a moving camera, and reconstructing the video. To help with reconstruction, additional information about the time and position (the motion parameters) must be transmitted along with the image data. Mosaicing of underwater images is a very active field of research, whose major thrust is dealing with the problems of motion parameter estimation. The Deep Submergence Laboratory at the Woods Hole Oceanographic Institution has been at the forefront of this research, engaging in both deep-sea terrain mosaicing, and using the technique for vehicle navigation. Mosaicing has also been used in an underwater pipe-monitoring system, developed by Fortkey, Ltd., a company based in U.K.

Some commercial solutions for underwater communications include the development of digital broadband underwater acoustic modems for offshore oil field applications, environmental monitoring or AUV command and control. As an example, the american company LinkQuest Inc., with headquarters in San Diego, offers a wide variety of models with different distance ranges and data rates.

In addition, Sea-Eye Underwater Ltd. (Ashkelon, Israel) is developing an acoustic modem that it claims

could transmit video images in real time wirelessly for underwater communication. The technology is based on ultrasound and is intended to for the transmission of real-time data, video or sonar images via a modem attached to video cameras or sonar, to be used by both divers and unmanned underwater vehicles (UUVs). The company is aiming to offer wireless real-time communication over a distance of 100 to 200 meters initially and then plans to optimize the technology for communications over 300 to 500 meters.

## **1.2 Approach**

The idea, or rather, the desire to transmit images wirelessly underwater, is a very plausible one with many applications, such as ports and harbor inspection and monitoring, oceanographic surveys, ecological inspection and recording, aqua-culture and fishing, recreational diving, private yacht inspection and homeland security. The existing techniques for underwater acoustic transmissions and video compression algorithms are at this time ripe enough to face the difficulties in terms of data rate needed for real-time video transmissions and bit rate supported by the underwater channel.

It is in this context that the combination of channel treatment techniques with standard compression algorithms allow the transmission of video data at high data rates using a high bandwidth. Moreover, the fact that underwater images and video are of low contrast enables them to be compressed to bit rates below those required for usual, terrestrial images and video.

The latter fact speaks in favor of the possibility to use readily available methods for video compression below 64 kbps, while advanced detection techniques provide the possibility to use a higher bandwidth and, consequently, a higher data rate for the proposed communication.

In the compression field, the standard MPEG-4 techniques can be applied in order to compress the video data to less than the bit rate needed to achieve a real-time transmission; in the communications field, recently developed algorithms for Orthogonal Frequency Division Multiplexing (OFDM) signal modulation and detection, which represent the state-of-the-art in the field, can be used in order to efficiently use the available bandwidth.

## **1.3 Objectives**

The main interest of this project is the advancement of basic research on video underwater communications, by coupling the latest commercially-available video compression methods with advanced signal processing techniques for high-speed underwater acoustic signal transmission. The final goal is to prove that high data rate video transmissions can be completed real-time, while providing appropriate quality for basic video inspection and monitoring, and an appropriate distance range between transmitter and receiver.

The basic problem of video transmission over an underwater acoustic channel is that of matching the bit rate requirements of the signal to the bandwidth of the channel. On the one hand, video signal has a large information content, which requires a large bit rate to be transmitted real-time. On the other hand, an underwater acoustic channel has a limited bandwidth, which only supports transmission at a limited bit rate.

The work will focus on research aspects and an experimental demonstration. Research will address (1) video compression with target bit rates of 64 kbps or less, and (2) bandwidth-efficient acoustic communication methods based on Orthogonal Frequency Division Multiplexing (OFDM) that can support such bit rates.

The experimental part of the work will consist of 3 sets of tests to demonstrate the feasibility of the

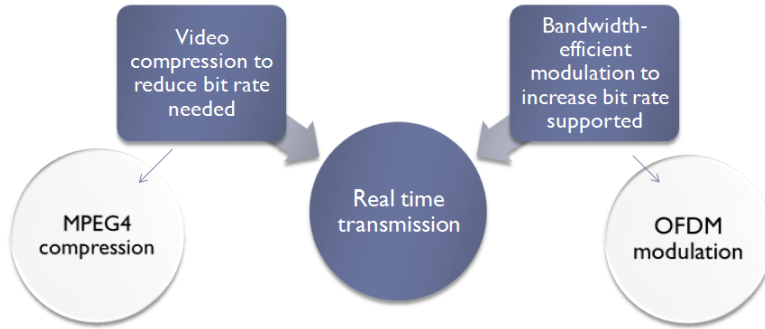


Figure 1.1: Problem statement

implementation: (1) study of the detection results for generated signals applied to simulated channels and recorded background noise, (2) transmission of signals in an in-air acoustic testbed, and (3) underwater transmission of generated video signals at different distance ranges.

## 1.4 Project workplan

The current project approach is eminently practical. An OFDM system implementation is designed in order to modulate the transmitted signal and the complementary demodulation algorithm is coupled to appropriate detection techniques to deal with the distortion present in the signal due to the underwater channel effects and the background noise.

The project workplan has been the one that follows:

- (3 months) Theoretical research:
  - (0.5 month) Study and selection of the required algorithms for the signal transmission and reception
  - (2.5 months) Implementation of the algorithms
- (0.5 month) Simulations:
  - (0.25 month) Channel simulation and noise addition algorithm implementation
  - (0.25 month) Simulations
- (5 months) Experiments:
  - (1 month) In-air testbed experiments
  - (4 months) Underwater experiments
- (1 month) Results analysis and report

The theoretical research is addressed in Chap. 2-6, and Chap. 7 introduces the practical deployment for the experiments. The simulations are included as a part of the experimental work in Chap. 8, along with the information about the experiments. Finally, Chap. 9 concludes the analysis and gives some future work tips.



# Chapter 2

## The underwater channel

The underwater channel is one of the most challenging for communication purposes. Among other characteristics, some major complications are the following: the attenuation is frequency-dependent, the communication bandwidth is dependent on the distance, and the Doppler effect is more accentuated than in radio channels and is non-uniform along the signal bandwidth. In addition, the background noise is non-negligible due to the common low power in the received signals, because of hardware constraints and the high attenuation.

Acoustic waves are used as the typical physical layer for underwater communication systems. Despite that this type of waves propagate at long distances through conductive sea water only at extremely low frequencies (30-300 Hz), higher frequencies can be used at lower distances while reducing the hardware requirements in terms of power and transducer characteristics. Another frequency range that can be used for underwater applications is the optical one, which has lower attenuation. In this case, the scattering and the required precision at pointing the laser beams restrict its use to very short distance (typically 10 m). For the previous reason, in this work the attention is focused on the acoustic channel.

### 2.1 Acoustic propagation

#### 2.1.1 Attenuation

The attenuation or path loss that occurs in an underwater acoustic channel over a distance  $l$  for a signal of frequency  $f$  is given by the following equation:

$$A(l, f) = l^k a(f)^l \quad (2.1)$$

where  $k$  is the spreading factor, which describes the geometry of propagation (typically 1.5 is used for practical spreading), and  $a(f)$  is the absorption coefficient. Expressed in dB:

$$10\log A(l, f) = k \cdot 10\log l + l \cdot 10\log a(f) \quad (2.2)$$

The absorption coefficient for frequencies above a few hundred Hz can be expressed empirically, using the Thorp's formula [2] which gives  $a(f)$  in dB/km for  $f$  in kHz as:

$$10\log a(f) = 0.11 \frac{f^2}{1+f^2} + 44 \frac{f^2}{4100+f} + 2.75 \cdot 10^{-4} f^2 + 0.003 \quad (2.3)$$

For lower frequencies, the following formula may be used:

$$10\log a(f) = 0.002 + 0.11 \frac{f^2}{1+f^2} + 0.011 f^2 \quad (2.4)$$

The absorption coefficient is the major factor that limits the maximal usable frequency of an underwater system. As it rapidly increases with frequency (see Fig. 2.1), the path loss will also increase, and therefore only the frequencies below a threshold may be used when deploying an underwater communication link.

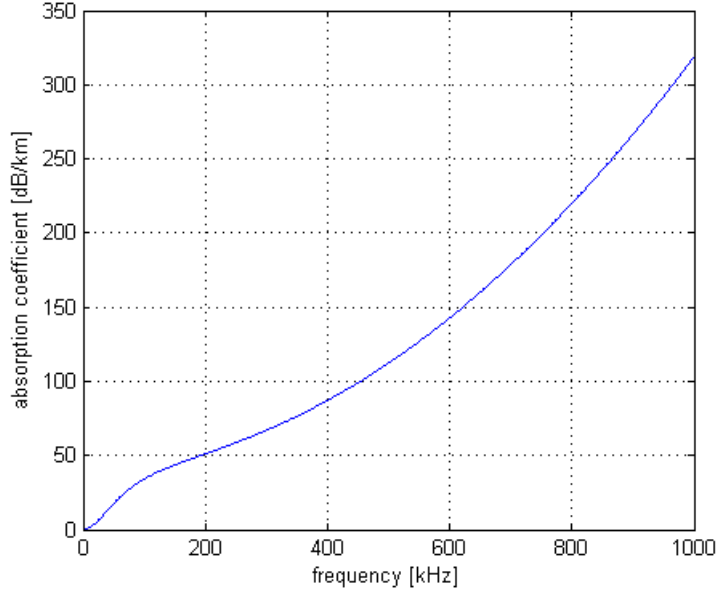


Figure 2.1: Absorption coefficient as a function of frequency

### 2.1.2 Noise

The ambient noise in the ocean can be modeled using four sources: turbulence, shipping, waves, and thermal noise. The majority of the ambient noise sources can be described by Gaussian statistics and a continuous power spectral density (p.s.d.). The following empirical formulae give the p.s.d. of the four noise components in dB re  $\mu$  Pa per Hz as a function of frequency in kHz [3]:

$$\begin{aligned}
10\log N_t(f) &= 17 - 30\log f \\
10\log N_s(f) &= 40 + 20(s - 0.5) + 26\log f - 60\log(f + 0.03) \\
10\log N_w(f) &= 50 + 7.5w^{1/2} + 20\log f - 40\log(f + 0.4) \\
10\log N_{th}(f) &= -15 + 20\log f
\end{aligned} \tag{2.5}$$

Turbulence noise influences only the very low frequency region,  $f < 10$  Hz. Noise caused by distant shipping is dominant in the frequency region 10 Hz - 100 Hz, and it is modeled through the shipping activity factor  $s$ , whose value ranges between 0 and 1 for low and high activity, respectively. Surface motion, caused by wind-driven waves ( $w$  is the wind speed in m/s) is the major factor contributing to the noise in the frequency region 100 Hz - 100 kHz (which is the operating region used by the majority of acoustic systems). Finally, thermal noise becomes dominant for  $f > 100$  kHz.

The overall p.s.d. of the ambient noise,  $N(f) = N_t(f) + N_s(f) + N_w(f) + N_{th}(f)$ , is illustrated in Fig. 2.2, for the cases of no wind (solid) and wind at a moderate 10 m/s (dotted), with varying degrees of shipping activity in each case. The noise increases at the low frequency range, thus limiting the useful acoustic bandwidth from below. Due to the linear decayment of the noise p.s.d. on the logarithmic scale (in a certain frequency range), the following approximation may then be useful:

$$10\log N(f) \approx N_1 - \eta \log f \tag{2.6}$$

The approximation is shown in the Fig. 2.2 with  $N_1 = 50$  dB re  $\mu$  Pa and  $\eta = 18$  dB/decade.

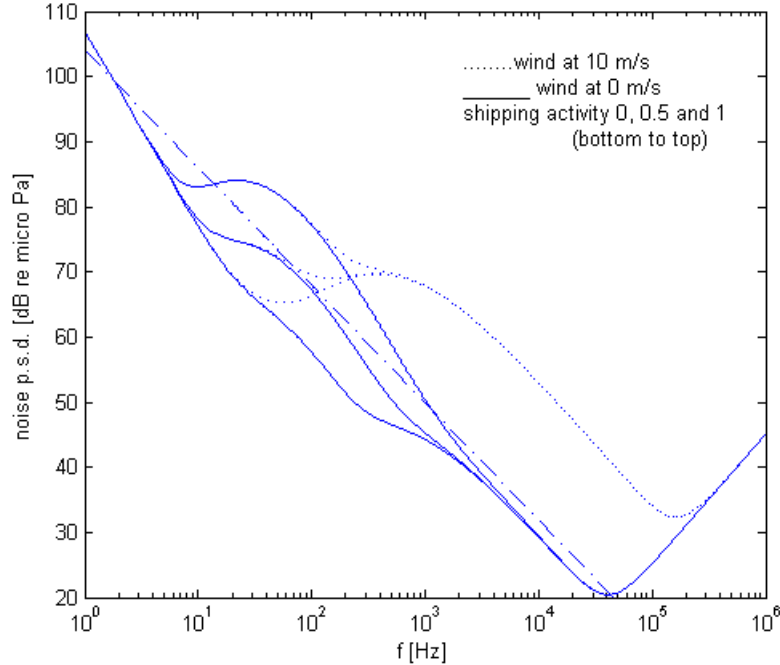


Figure 2.2: Power spectral density of the ambient noise,  $N(f)$  [dB re  $\mu$  Pa]. The dash-dot line shows the approximation 2.5

### 2.1.3 Propagation delay

The experienced delays in an underwater acoustic communication link are much higher than in an open-air link. The nominal speed of sound in water is 1,500 m/s, which is 200,000 lower than the speed of electromagnetic waves in open-air ( $3,000 \cdot 10^5$  m/s). This causes long propagation delays, which becomes a major complication for the application of feedback to correct the channel distortions. As an example, typical propagation delays in acoustic underwater links can be of several seconds, while the measured coherence time in an underwater channel can be of 100 milliseconds. In contrast with the propagation delays in underwater channels, the open-air propagation delay is typically of some microseconds.

### 2.1.4 Multipath

Multipath propagation is one of the common problems in communications through underwater acoustic links. This propagation phenomenon results in communication signals reaching the receiving antenna by two or more paths. At the receiver, due to the presence of multiple paths, more than one pulse will be received, and each one of them will arrive at different times. Thus, the channel impulse response will be expressed by:

$$h(t) = \sum_{p=1}^N h_p \delta(t - \tau_p) = \sum_{p=1}^N \rho_p e^{j\phi_p} \delta(t - \tau_p) \quad (2.7)$$

where the channel taps,  $h_p$ , arriving at  $\tau_p$ , can be described by an amplitude component  $\rho_p$  and a phase shift  $\phi_p$ .

Underwater multipath can be caused either by reflection or refraction of the acoustic waves. Reflection of the acoustic waves occurs when the wave bounces either at the surface or the bottom and reaches the receiver. It is most common in shallow water environments. Refraction of the communication waves is a typical phenomenon in deep water links, where the speed of sound changes at different depths. An explanatory scheme is shown in Fig. 2.3.

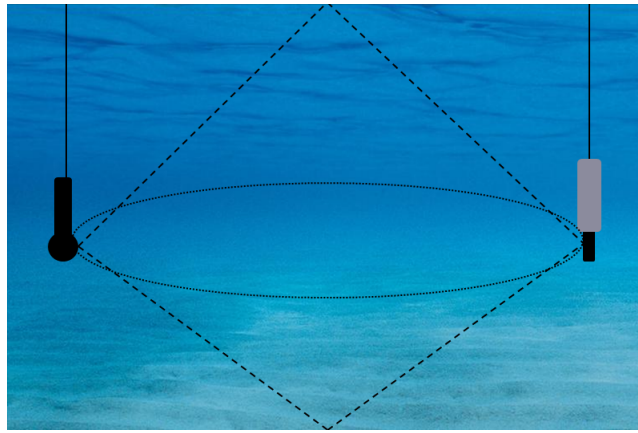


Figure 2.3: Multipath effects. Reflective effects (dashed line) and refractive effects (dotted line)

The distortions caused by multipath must be equalized in the receiver. In addition, ways to avoid Inter-Symbol Interference (ISI) must be designed in order to correctly demodulate and detect the transmitted data. Later on in Chap. 6 a receiver algorithm for underwater acoustic channels that deals with multipath effects will be explained.

### 2.1.5 Doppler effect

Another common problem of underwater acoustic communication systems is the fact that they have to deal with a non-negligible Doppler effect of the acoustic waves. The Doppler effect is caused by the relative motion of the transmitter-receiver pair, and it causes a shift in the frequency components of the transmitted signal. The frequency shift is mainly described by the factor  $v_r/c$ , where  $v_r$  is the relative velocity between transmitter and receiver, and  $c$  is the signal propagation speed (the speed of sound underwater in this case). In underwater environments  $c$  is much lower than in open-air, and so the Doppler effect is not ignorable. In addition, the fact that underwater systems are wideband causes much different Doppler shifts for different frequency components of the transmitted signal. This is typically known as frequency spreading.

It is of key importance that underwater acoustic systems deal with non-uniform Doppler effect. As an example, a bad Doppler effect correction in a multicarrier system could cause Inter-Carrier Interference (ICI), which happens when some distortion due to other subcarriers' information is present in a selected channel. Although no Inter-Carrier Interference compensation technique has been considered necessary in this study, further information can be found in [4].

## 2.2 Resource allocation

Taking into account the physical models of acoustic propagation loss and ambient noise, the optimal frequency allocation for communication signals can be calculated. Considering optimal signal energy allocation, such frequency band is defined so that the channel capacity is maximized [5, 6].

The results that are assessed suggest that, despite the frequency spectrum is not yet regulated by the Federal Commission of Communications (FCC) for underwater acoustic communications, the possibilities in terms of usable frequency bands are not numerous, due to acoustic path propagation and noise characteristics.

### 2.2.1 The AN product and the SNR

The narrow-band Signal to Noise Ratio (SNR) observed at a receiver over a distance  $l$  when the transmitted signal is a tone of frequency  $f$  and power  $P$  is given by

$$SNR(l, f) = \frac{P/A(l, f)}{N(f)\Delta f} = \frac{S(f)}{N(f)A(l, f)} \quad (2.8)$$

where  $\Delta f$  is a narrow band around the frequency  $f$ , and  $S(f)$  is the power spectral density of the transmitted communication signal. Directivity indices and losses other than the path loss are not counted. The AN product,  $A(l, f)N(f)$ , determines the frequency-dependent part of the SNR. The inverse of the AN product,  $1/A(l, f)N(f)$ , is illustrated in Fig. 2.4.

### 2.2.2 Optimal frequency

Observing the inverse of the AN product,  $1/A(l, f)N(f)$  (Fig. 2.4), it can be concluded that for each distance  $l$  there clearly exists an optimal frequency  $f_0(l)$  for which the maximal narrow-band SNR is obtained at the receiver. The optimal frequency is plotted in Fig. 2.5 as a function of the transmitter-receiver distance.

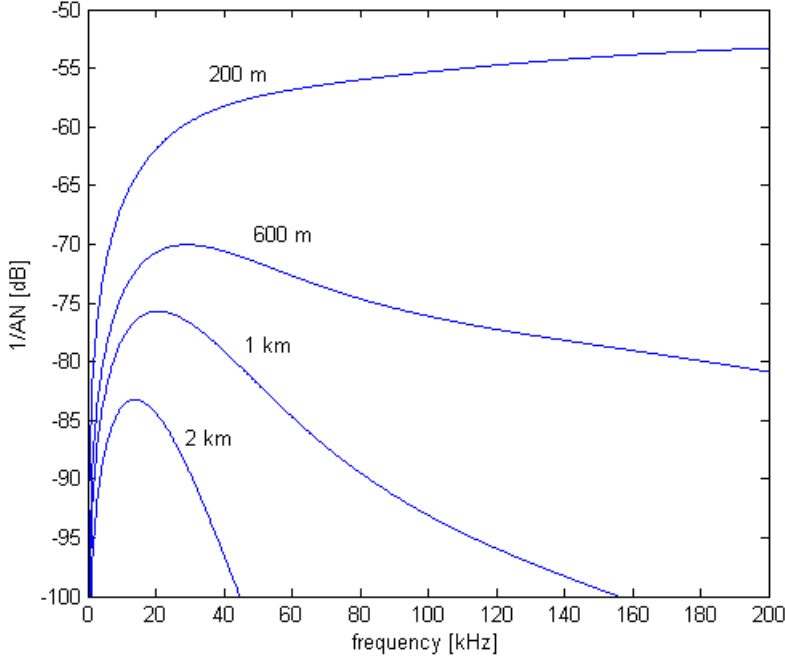


Figure 2.4: Frequency-dependent part of the SNR,  $1/A(l, f)N(f)$ . Practical spreading,  $k = 1.5$ , is used for the path loss  $A(l, f)$ . The linear approximation is used for the noise p.s.d.  $N(f)$

Ideally, when implementing a communication system, some transmission bandwidth around  $f_0(l)$  is chosen. The transmission power is adjusted so as to achieve the desired SNR level throughout the selected frequency band. Practically, the response of the transducers and hydrophones must be taken into account and the optimal transmission frequency may vary.

### 2.2.3 3 dB bandwidth definition

A common definition for the system bandwidth in communications is the 3 dB bandwidth one. We define the 3 dB bandwidth  $B_{3dB}(l)$  as that range of frequencies around the optimal frequency  $f_0(l)$  for which  $SNR(l, f) > SNR(l, f_0(l))/2$ . From (2.8) and considering a constant p.s.d. of the transmitted signal,  $S(f)$ , the previous relation can be expressed as  $A(l, f)N(f) < 2A(l, f_0(l))N(f_0(l)) = 2AN_{min}(l)$ . The 3 dB bandwidth,  $B_{3dB}(l)$ , and the center frequency of the frequency band,  $f_c(l)$ , are shown in Fig. 2.5. Similar trends are observed for these two parameters and the optimal frequency,  $f_0(l)$ , as it is expected.

### 2.2.4 Transmission power

Once the transmission bandwidth is set, the transmission power  $P(l)$  can be adjusted to achieve a desired narrow-band SNR level corresponding to the 3 dB bandwidth  $B_{3dB}(l)$ . If we denote by  $S_l(f)$  the p.s.d. of the transmitted signal chosen for the distance  $l$ , then the total transmitted power is

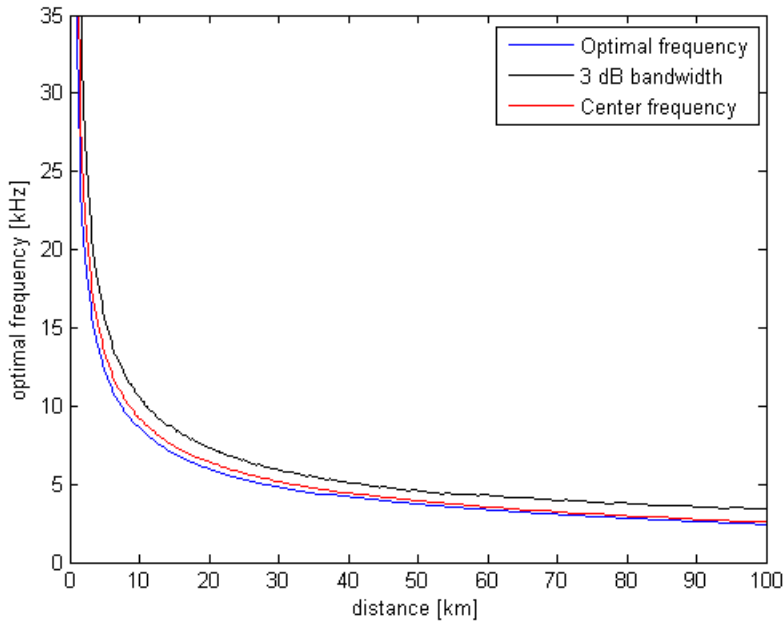


Figure 2.5: Optimal frequency  $f_0(l)$  considering the inverse of the AN product,  $1/A(l, f)N(f)$ . The 3 dB bandwidth,  $B_{3dB}(l)$ , and the center frequency of this bandwidth,  $f_c(l)$ , is also shown

$$P(l) = \int_{B_{3dB}(l)} S_l(f) df = SNR_0 B_{3dB}(l) \frac{\int_{B_{3dB}(l)} N(f) df}{\int_{B_{3dB}(l)} A^{-1}(l, f) df} \quad (2.9)$$

where the transmitted signal p.s.d. is considered constant in the signal bandwidth.

As a practical impact of the center frequency,  $f_c(l)$ , and the transmission bandwidth to the required transmission power for the successful reception of communication signals, some experimental results are shown in Fig. 2.6.

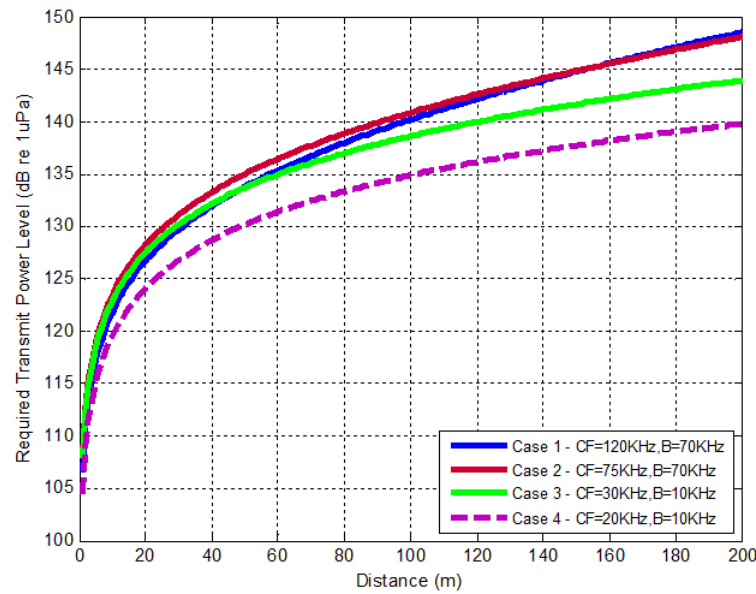


Figure 2.6: Required transmission power for quiet measurements in an oil field

# Chapter 3

## Video compression techniques

In the realm of video compression, better visual quality with higher compression rates are the main goals that must be met by the techniques to be successful in the marketplace. In the underwater channel, the transmission link has a limited bit rate capacity, which can be of about tenths of kbps (typical bit rates are 10-30 kbps). This fact makes it even more important to find powerful compression techniques that can reduce the requirements for real-time video transmissions. For instance, a very low resolution video (QCIF) with a frame rate of about 5 fps will require about 1.5 Mbps for its uncompressed transmission. Even in this case, a compression factor of about 1:100 is needed to achieve the targeted reduction in data rate.

Today, compression methods exist that can be used to transmit video at 64 kbps. In particular, the commercially-available MPEG-4 encoders provide compression at this rate, by combining spatial and temporal techniques. Existing efforts at applying MPEG-4 compression for acoustic underwater video transmission include [7], where a single carrier modulation scheme operates over a short range (300 m).

### 3.1 Compression fundamentals

#### 3.1.1 Images and video

To understand how a compression technique works, a few words must be said about common concepts such as *image* and *video*. In the image processing field, an image is considered to be a two-dimensional array of samples that are called pixels (picture elements, Fig. 3.1). Each picture element can be a vector of any dimension that represents the visual information that it contains. It can be just a one-dimensional vector which represents luminance (or luminous intensity) for grey-scale images, or three-dimensional vectors which represent color components for color images.

Many techniques have been designed to accurately represent color images. The easiest one, but less used, is the RGB (Red Green Blue) components system, in which an image is represented by 3 vectors, each of which containing the intensity of red, green and blue that the image has.

Another popular way to represent the color images is using the YUV space components system, where an image is defined by its luminance Y, and two color difference components (U,V). These two color difference components are defined as  $U=B-Y$  and  $V=R-Y$ . The main advantage of this representation system is that grey-scale images can be represented by black and white devices by just choosing the Y component. In addition, the human visual system is more sensitive to luminance than color, and using this representation

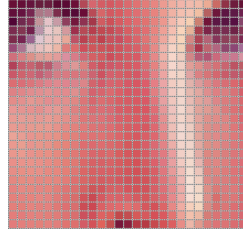


Figure 3.1: Image pixels

a higher resolution can be given to the Y component despite sacrificing some resolution for color difference components (U,V). An example image decomposition is shown in Fig. 3.2.

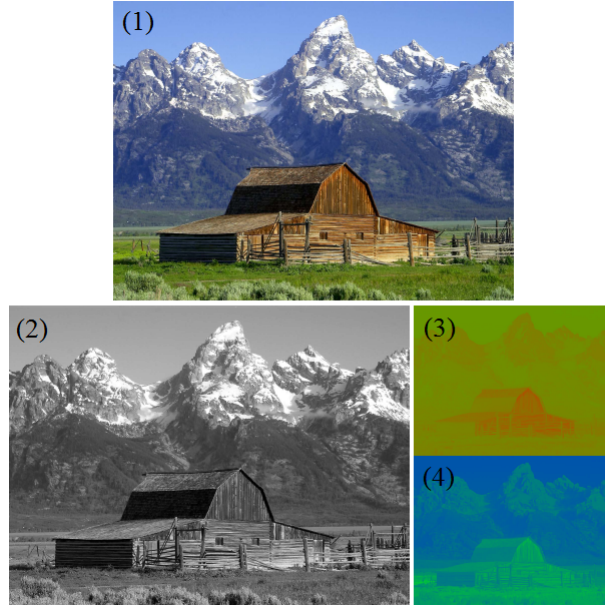


Figure 3.2: YUV image representation. (1) Original signal. (2) Luminance Y signal. (3) Chrominance V signal. (4) Chrominance U signal

The quality of an uncompressed digital picture depends on two important parameters: resolution (width  $\times$  height) and color depth (number of bits used to represent each pixel). The picture is finer with higher resolution, or in other words, more pixels are used. As a result, the edges become smoother and the image more natural. Some standard resolutions include 1920  $\times$  1080 for full high definition television systems (HDTV) or 640  $\times$  480 for conventional VGA systems. Typical color depths are 1 bit (2 colors), 8 bits (256 colors), 16 bits (65536 colors), 24 bits (true color), etc.

A video consists of a sequence of still images that are captured from a recording device and that, correctly timed and displayed, convey not only the picture information, but also the motion in a scene (Fig. 3.3).

Some words must be said about the timing of the individual images in a video. Nowadays time-stamps are transmitted to accurately indicate the exact moment when an image should be displayed, so that the targeted frame rate is achieved. The frame rate in a video is another quality measurement as from it depends the subjective motion sensation. With higher frame rate the motion becomes smoother but it requires the transmission of more data, as more images are sent for each second of video. It is well known that about 25 fps are required to correctly show the motion in a general purpose video, although a lower frame rate might

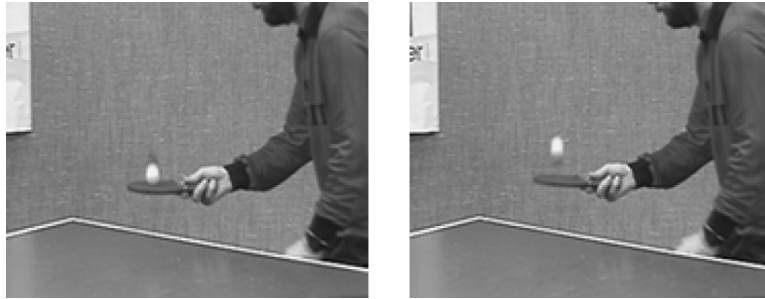


Figure 3.3: Consecutive images of a video file

be used for low motion sequences. Fortunately, underwater video imagery can be included in this last group, and even some images each 5 or 10 seconds may suffice for some applications.

### 3.1.2 Compression approaches

Video compression becomes possible since there are mainly two types of redundancies: spatial and temporal. Spatial redundancy exists between nearby regions of an image where the color components don't change much. Temporal redundancy exists as, given a proper frame rate, there is not much change between a frame and the next. There are two basic approaches to video compression, depending on what type of redundancy within the video sequence is exploited.

In the first approach, video is treated as a sequence of independent images, each of which is individually compressed and transmitted over the channel (*intra mode*). This approach has been favored in almost all existing attempts at video transmission over underwater acoustic channels [8–13].

The majority of these efforts used the standard JPEG compression, which is based on the Discrete Cosine Transform (DCT). Its basic steps are the following:

1. Division of the image into blocks (usually 8x8 pixel blocks) (see Fig. 3.4)



Figure 3.4: Division of the image into blocks

2. Every block is compared to the DCT basis (see Fig. 3.5)

In the second approach, the images in a video sequence are not encoded independently. Instead, only the first image in a sequence is fully encoded, while from there on, the *difference* between successive images is encoded. Since the images do not change rapidly, their difference can be represented by fewer bits than the full image, and, hence, the required bit rate can be reduced.

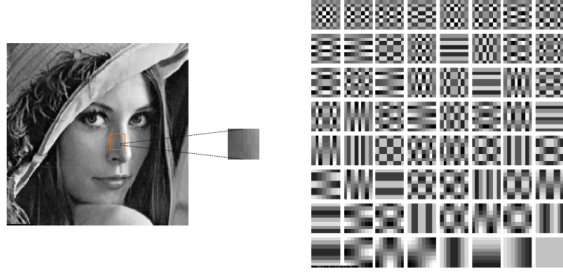


Figure 3.5: Image (left) and DCT basis (right)

The practical implementations include the transmission of motion vectors that represent the motion in the scene, along with the prediction error after the application of the calculated motion vectors (*inter mode*). The transmission of the prediction error is necessary to avoid error propagation in the receiver. A transmitter scheme is shown in Fig. 3.6.

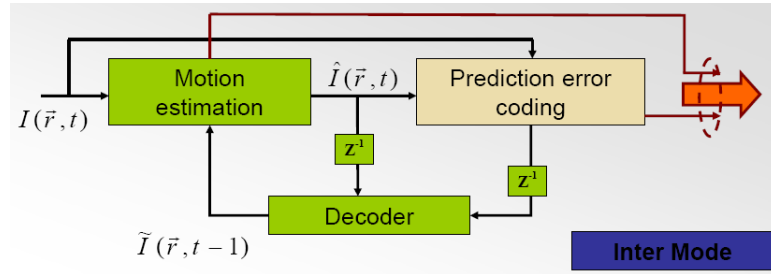


Figure 3.6: Temporal coding transmission scheme

The best performance for motion compensation algorithms is achieved when a combination of forward predicted pictures from a past image, and bi-directional predicted pictures from both a past image and a future image is transmitted.

The main drawback of temporal coding is the error propagation. Due to that, the standards define the Group Of Pictures (GOP), which include *Intra* frames (which do not depend on other images), forward predicted frames (*P* frames), and bi-directional predicted frames (*B* frames). A sample GOP is shown in Fig. 3.7.

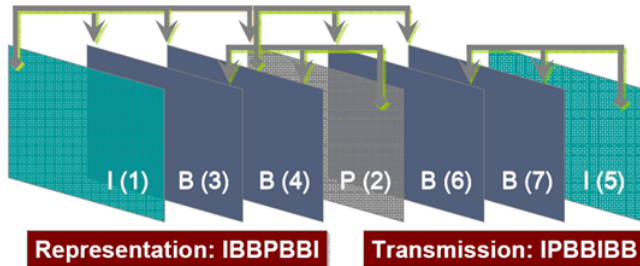


Figure 3.7: Group Of Pictures (GOP)

## 3.2 MPEG-4 standard

Moving Picture Experts Group (MPEG) is an experts group formed by the International Organization for Standardization (ISO) to set standards for audio and video compression and transmission. MPEG standards consist of certain *Parts* that cover different aspects of the specification. The standards also define *Profiles* and *Levels* that define a set of tools and parameters for practical systems.

MPEG-4 (1998) provides more complex coding tools and higher compression factors than its predecessors MPEG-1 and MPEG-2. Its main feature is the definition of the concept Audio-Visual Object (AVO), oriented to manipulation.

### 3.2.1 Functionalities

MPEG-4 was initially designed for audiovisual encoding at very low bit rates (< 64 kbps, 64 - 384 kbps, 384 kbps - 4 Mbps) with attention to error resilience. Later on, its focus shifted to an *object oriented* approach, with multiple audiovisual objects encoded using different techniques and composited in the decoder.

It uses a hybrid temporal-spatial coder (basic scheme shown in Fig. 3.8) for natural and synthetic data coding, with improved temporal random access and coding efficiency, and high robustness in challenging environments.

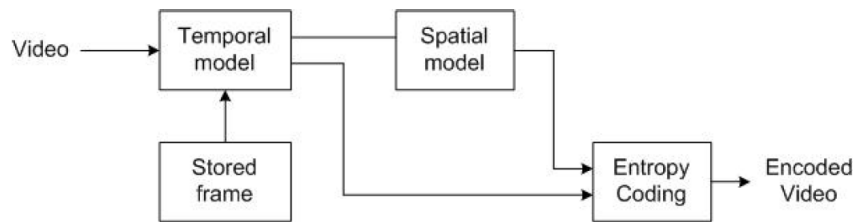


Figure 3.8: Hybrid temporal-spatial coding basic scheme

### 3.2.2 Very Low Bit-rate Video core

In the MPEG-4 standard, besides content-based functionalities for modern interactive multimedia systems, there are specified functionalities for very low bit rate video in error prone environments.

As it can be seen in Fig. 3.9, *VLBV Core* (Very Low Bit-rate Video) provides algorithms and tools for applications operating at bit rates typically between 5 and 64 kbps. They support image sequences with low spatial resolution (typically up to CIF resolution) and low frame rates (typically up to 15 Hz). The basic applications' specific functionalities supported by the VLBV Core include coding of conventional rectangular size image sequences with high coding efficiency and high error robustness/resilience, low latency and low complexity for real-time multimedia communication applications.

For the current project, with limited available bit rate due to the characteristics of the underwater channel, MPEG-4 VLBV Core is a good candidate.

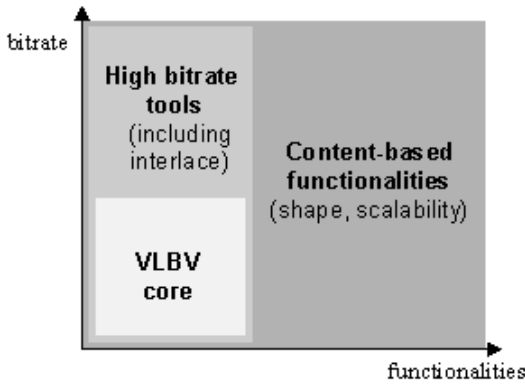


Figure 3.9: Classification of the MPEG-4 image and video coding algorithms and tools

### 3.3 Implementation

The compression method chosen in this project is based on the MPEG-4 Part 2 (Visual) with Simple Profile.

#### 3.3.1 MPEG-4 codec

The popular MPEG-4 Xvid codec is used. Xvid is an open-source research project focusing on video compression and is a collaborative development effort. All its code is released under the terms of the GNU General Public License (GPL).

The Xvid video codec implements MPEG-4 Simple Profile and Advanced Simple Profile standards with features such as: *B* frames, global and quarter pixel motion compensation and lumi masking, among others. It allows compression and decompression of digital video, in order to reduce the required bandwidth of video data for transmission over computer networks, or efficient storage on CDs or DVDs.

#### 3.3.2 Performance

The performance of the MPEG-4 codec has been tested by compressing two video files, which are the ones that have been used for the underwater video experiments. The video files have different resolutions, and two different compression factors have been chosen, one with high compression for the low resolution file, and the other with lower compression performance for the high resolution video.

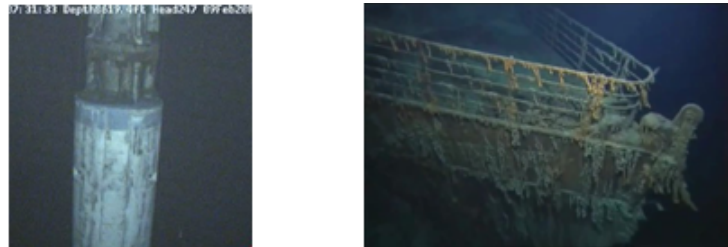


Figure 3.10: Lower quality video (left) and higher quality video (right)

The low quality (LQ) video consists of a pipe inspection footage and has been recorded with a resolution of  $256 \times 256$  pixels. Along with the higher compression factor, it represents a quite appropriate set of parameters for a real-time video transmission.

The high quality (HQ) video is taken from a Titanic shipwreck inspection and has a resolution of  $480 \times 320$  pixels. As an example of a transmission of higher quality video with current techniques, it has been compressed with a slightly lower compression factor.

The table 3.1 shows a comparison of different parameters for the modulated videos, along with an assessed real-time frame rate that could be supported for such files with two sets of realistic modulation parameters. The table 3.2 contains the information about the modulation parameters (1) and (2).

	Pipe inspection	Titanic footage
Recorded video duration (s)	1.67	20
Modulated signal duration (s) with (1)	2.61	42.41
Modulated signal duration (s) with (2)	4.14	70.61
Number of frames	50	319
Recorded frame rate	30	30
Real-time frame rate (1)	19.16	7.52
Real-time frame rate (2)	12.08	4.52

Table 3.1: Frame rate study

	Bandwidth (kHz)	Subcarrier modulation	FEC coding	Data rate (kbps)
Configuration (1)	115	8-PSK	BCH(63,30)	151
Configuration (2)	115	8-PSK	BCH(63,18)	91

Table 3.2: OFDM system parameters



# Chapter 4

## OFDM fundamentals

Single-carrier equalization [14] is a method that has been used for virtually all systems that attempted image or video transmission through an underwater acoustic channel. This method has also been used in previous work done at the MIT Sea Grant College Program [10], where pre-packaged video images were transmitted at a very high bit rate of 150 kbps, but only over a stable, 10 m long vertical path.

Research in the area of underwater acoustic communications over the past several years has resulted in demonstrating a different type of bandwidth-efficient modulation and detection method, which uses multiple carriers instead of a single carrier. In its basic form, this method is known as Orthogonal Frequency Division Multiplexing (OFDM).

Because of its simplicity, OFDM has found application in many wireline (DSL) and wireless radio systems (digital audio and video broadcast, wireless LAN) and is being considered for the fourth generation mobile cellular systems. Its application to underwater acoustic systems has been addressed recently.

### 4.1 General description

Modulation is the process of transforming a message signal to make it easier to work with. In telecommunications, signal modulations are chosen taking into account some parameters, such as implementation complexity, supported data rate, and robustness against channel and noise effects.

Multi-carrier modulation is an attractive alternative to single-carrier broadband modulation on channels with frequency-selective distortion. It is based on the idea of dividing the total available bandwidth into many narrow subbands, such that the channel transfer function appears constant (ideal) within each subband. By doing so, the need for time-domain channel equalization is eliminated. Instead, the subbands have to be separated in the frequency domain, which is efficiently performed using only the Fast Fourier Transform (FFT). This efficient implementation using the FFT can be executed for multi-carrier modulation and detection when used with rectangular pulse shaping.

The modulation technique on which the project is based is the Orthogonal Frequency Division Multiplexing (OFDM) scheme and its ability to convey the information modulated in multiple subcarriers using a basic modulation scheme, achieving an adequate transmitter/receiver complexity, appropriate capacity, and providing numerous possibilities for channel compensation.

OFDM is a frequency-division multiplexing (FDM) scheme utilized as a digital multi-carrier modulation

method. A large number of closely-spaced orthogonal subcarriers are used to carry data. The data is divided into several parallel data streams or channels, one for each subcarrier. Each subcarrier is modulated with a conventional modulation scheme (such as Quadrature Amplitude Modulation -QAM- or Phase Shift Keying -PSK-) at a low symbol rate, maintaining total data rates similar to conventional single-carrier modulation schemes in the same bandwidth. Fig. 4.1 shows the utilization of the available bandwidth for a 7 subcarriers OFDM signal.

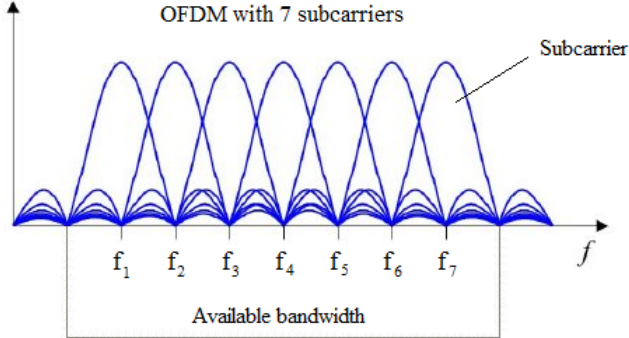


Figure 4.1: Bandwidth utilization for an OFDM signal

## 4.2 Orthogonality

One of the main features of OFDM is that the subcarriers are chosen to be orthogonal to each other. That means that in the center frequency of the subcarrier  $k$ ,  $f_k$ , the other subcarriers' amplitude is null (see Fig. 4.1). The consequence of this fact is that cross-talk between subchannels is avoided and inter-carrier guard bands are not necessary. This leads to a simplification of the design for both the transmitter and receiver, as a separate filter for each subchannel is not required (unlike other FDM schemes).

The orthogonality principle requires a subcarrier spacing of  $\Delta f = \alpha/T$  Hz (as shown in Eq. 4.1), where  $T$  is the useful symbol duration in seconds, and  $\alpha$  is a positive integer (typically 1). Hence, the total useful bandwidth is  $B = K\Delta f$  Hz, where  $K$  is the total number of subcarriers.

$$\langle \phi_k(t), \phi_m(t) \rangle = \int_0^T e^{j2\pi(k-m)\Delta f t} dt = \frac{e^{j2\pi(k-m)} - 1}{2\pi\Delta f(k-m)} = \delta(k - m) \quad (4.1)$$

One of the most important advantages of orthogonality between subcarriers is that it allows high spectral efficiency, as almost the full available frequency band can be utilized.

A disadvantage that results from the use of orthogonality is the need for highly accurate frequency synchronization between the transmitter and the receiver. The frequency deviation that OFDM systems can tolerate is very small, as the subcarriers will no longer be orthogonal, causing Inter-Carrier Interference (ICI), or cross-talk between subcarriers.

Frequency offsets are typically caused by Doppler shifts due to motion, or mismatched transmitter and receiver oscillators. While Doppler shift alone may be compensated for by the receiver, the situation is worsened when combined with multipath, as reflections will appear at various frequency offsets, which is much harder to correct.

### 4.3 Modulation using FFT

Due to the orthogonality of OFDM subcarriers, the modulator and demodulator can be efficiently implemented using the FFT algorithm on the receiver side, and the inverse FFT, or IFFT, on the transmitter side. As it has been claimed, on the transmitter side the IFFT of a signal  $X(k)$ , where  $k$  denotes the frequency component index, is

$$x(l) = \frac{1}{K} \sum_{k=0}^{K-1} X(k) e^{j2\pi kl/K}, \quad l = 0, \dots, K-1 \quad (4.2)$$

where  $K$  designates the number of frequency components, and  $x(l)$  is the resulting sampled signal, which is formed by the sum of the modulated frequency components  $X(k)$  (at their corresponding digital frequency  $k/K$ ). To retrieve again the digital frequency components, the inverse equation must be used:

$$X(k) = \sum_{l=0}^{K-1} x(l) e^{-j2\pi kl/K}, \quad k = 0, \dots, K-1 \quad (4.3)$$

which corresponds to the  $K$ -point FFT of  $X(k)$ .

The transmission side is shown in Fig. 4.2, where an IFFT applied to the subcarrier complex constellation points is enough to assess the time domain sequence. A complementary receiver is easily implemented by performing an FFT on the received modulated signal, retrieving the complex symbols for each subcarrier.

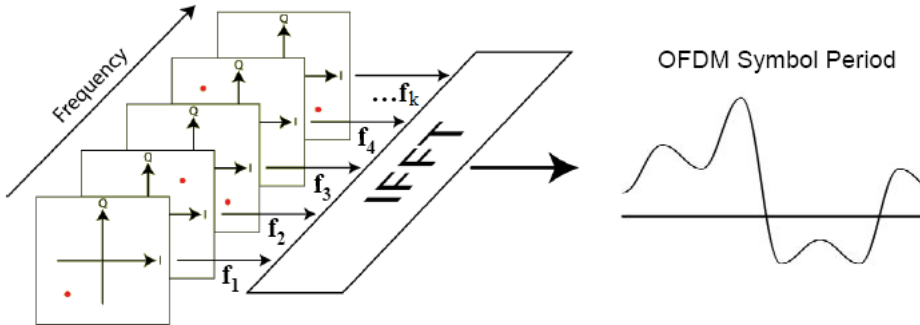


Figure 4.2: Efficient transmitter implementation using IFFT

### 4.4 Guard time

One of the advantages of the OFDM scheme is that, since the data in each block is divided into  $K$  parallel symbol streams that are transmitted at a low symbol rate, the system may become more robust against Inter-Symbol Interference (ISI) caused by the multipath channel.

As the duration of each symbol is longer than in a single high rate stream, the insertion of a guard time between the OFDM blocks (or symbols) is feasible, thus reducing the possible ISI. In addition, the guard interval also eliminates the need for a pulse-shaping filter, and it reduces the sensitivity to time synchronization problems.

## 4.5 Equalization

The need for highly complex time domain equalizers is avoided in OFDM system implementations. The fact that a number  $K$  of narrow-band channels is used to deliver the symbols helps mitigate the effects of frequency-selective channel conditions, such as fading caused by multipath propagation. Within a subcarrier band the channel is considered constant (flat) if the number of subcarriers  $K$  is large enough, hence making channel equalization far simpler than in single-carrier systems.

If differential detection or differential modulation (such as DPSK or DQPSK) is applied to the subcarriers, equalization can be completely omitted, since these non-coherent schemes are insensitive to slowly changing amplitude and phase distortion.

## 4.6 Advantages

The main advantage of the OFDM modulation scheme in terms of practical implementation is that it enables channel equalization in the frequency domain, thus eliminating the need for potentially complex time-domain equalizers.

OFDM modulation techniques have been used both in wired and wireless systems due to its advantages. Among them, the following must be mentioned:

- Simple and effective channel equalization in the frequency domain
- High spectral efficiency
- Robustness against Inter-Channel Interference (ICI)
- Robustness against Inter-Symbol Interference (ISI) and fading caused by the multipath channel
- Efficient implementation using the FFT, avoiding the need for complex subchannel filters
- Low sensitivity to time synchronization errors

## 4.7 Disadvantages

The major disadvantages of OFDM are:

- Sensitivity to frequency offsets
- High Peak to Average Ratio (PAR), with a subsequent difficulty to optimize the transmission power

The major difficulty in applying OFDM to an underwater acoustic channel is the signal's sensitivity to frequency offsets, which imposes strict synchronization requirements. Motion-induced Doppler effect in an acoustic channel creates a frequency offset that is not uniform across the signal bandwidth. This fact is in stark contrast to the frequency distortion in radio systems, and, hence, many of the existing synchronization methods cannot be used directly. Instead, dedicated methods have to be designed. Such methods have been proposed over the past several years, and demonstrated good performance in initial trials with real data transmitted over a few kilometers at bit rates on the order of 10 kbps within comparable acoustic bandwidths [15–17].

# Chapter 5

## OFDM transmitter

One of the most important parts of the project is designing a concrete system that can reach the desired performance under experimental conditions. To do so, some practical considerations must be taken into account and, given that information, the implementation is then designed to best perform with the available hardware.

The implemented OFDM system is defined in this chapter, and the chosen system model is introduced. In addition, the different implementation parts are explained.

### 5.1 System model

The model used on the transmitter side consists of a typical OFDM system with  $K$  subchannels, where the input data stream (in the video case, the MPEG-4 coded video file) is scrambled to uniformize the power allocation and randomize the values “0” and “1” in the input data stream. After that, the channel coding is performed and the data stream that comes out of the coder is serial-to-parallel converted into  $K$  streams  $d_k(n)$ ,  $k = 0, \dots, K - 1$ . These streams are then interleaved and used to form the signals

$$u_k(t) = \sum_n d_k(n) e^{jk\Delta\omega(t-nT')} g(t - nT') \quad (5.1)$$

where the following apply:

- The signal  $g(t)$  is a rectangular pulse in time with unit amplitude and duration  $T$
- $T' = T + T_g$ , where  $T_g$  is the guard interval, which is longer than the multipath spread
- $\Delta\omega = 2\pi\Delta f$ , where  $\Delta f = 1/T$  is the carrier spacing

The synchronization preamble in baseband and the guard times are included to the signal  $\sum_{k=0}^{K-1} u_k(t)$  to create the signal  $z(t)$ , and then a frequency shift is applied so that the modulated signal is given by

$$s(t) = \operatorname{Re}\{z(t)e^{j\omega_0 t}\} \quad (5.2)$$

where  $f_0$  is the lowest subcarrier frequency, and  $f_k = f_0 + k\Delta f$  denotes the  $k$ -th subcarrier frequency. The symbol rate is  $R = K/(T + T_g)$  symbols per second (sps), and the signal bandwidth is defined as  $B = K\Delta f$ . The resulting bandwidth efficiency is given by  $R/B = 1/(1 + T_g/T)$  sps/Hz.

The system model flowchart is shown in Fig. 5.1. A final consideration must be commented, which is that some Peak to Average Ratio (PAR) reduction techniques have been implemented and do not appear in the scheme, as depending on the chosen technique they take place before the IFFT block or after it. These specific techniques that are included in the implemented system to make a better use of the available transmission power are explained in Sec. 5.2.6.

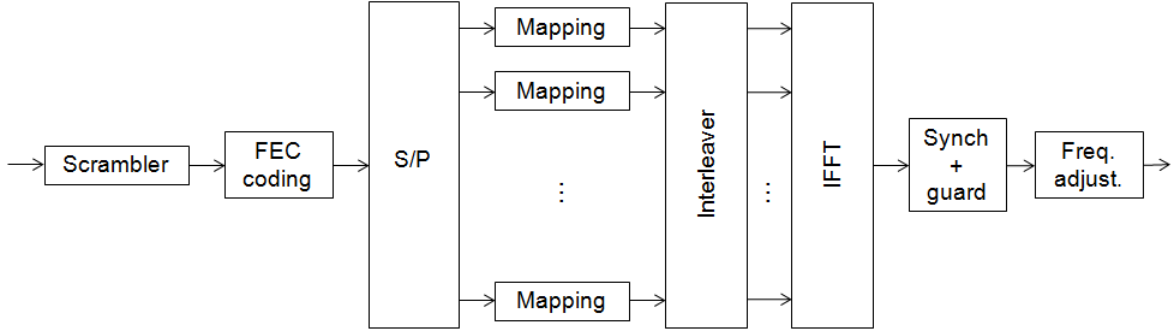


Figure 5.1: Transmitter scheme

## 5.2 Transmitter implementation

In this section, the most important parts of the designed transmitter implementation are discussed. In addition, specific information about the theoretical fundamentals along with some practical considerations are given.

### 5.2.1 Scrambling

Scrambling or randomizing binary sequences eliminates the correlation between the different bits of a data stream. This means that after the scrambler block the sequence of bits will appear random, with a similar amount of “0” and “1” values, thus avoiding long “0” or “1” bursts that pass into the FEC coder and give as a result the same coded word.

This method is successfully implemented by applying a logical XOR operation between (1) the data bits that come from the source coder (in the video case an MPEG-4 coder) and (2) a pseudo-random scrambling sequence of a certain length (in the practical implementation its size is 1.25 MB) that is repeated in case the data is longer than the chosen sequence. The procedure is illustrated in Fig. 5.2.

It must be noted that the applied procedure can be easily decoded by applying a logical XOR operation between (1) the scrambled data bits that are received from the channel and (2) the same pseudo-random sequence that was used to scramble the bits on the transmission side.

The scrambling algorithm, apart from providing further coding of the signal to increase the security and protection of the established communication, has proven to reduce the Peak to Average Ratio (PAR) of the resulting OFDM signal (see Sec. 5.2.6), as it has the effect of decorrelating the constellation points that

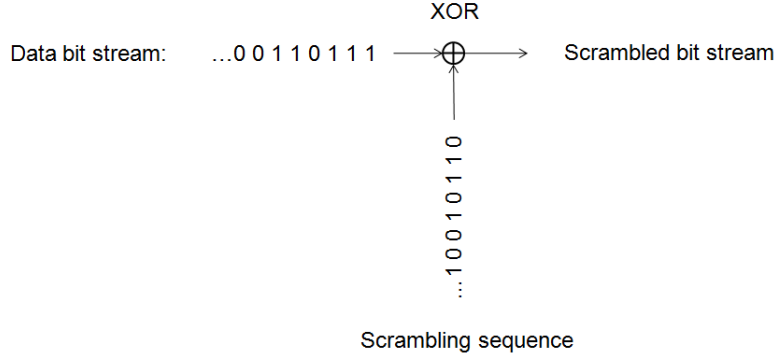


Figure 5.2: Scrambler scheme

come out from the subcarrier mapper. An example of its effect is shown in Fig. 5.3, where the first peak present when scrambling is not used is eliminated in the case it is enabled.

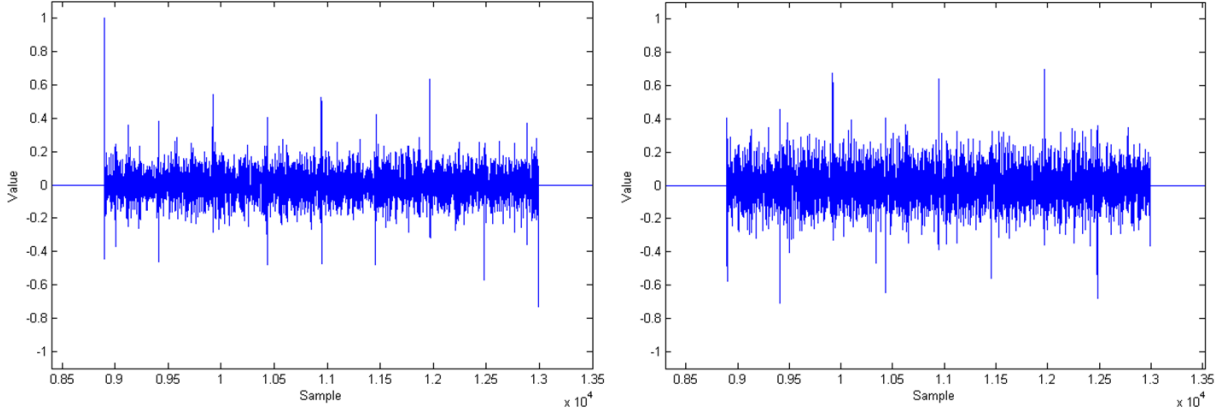


Figure 5.3: Scrambling effect on PAR reduction: (left) OFDM sample block with non-scrambled bits, and (right) OFDM sample block with scrambled bits

### 5.2.2 FEC coding

The long packet delays due to the low speed of propagation in underwater environments suggest the avoidance of packet retransmissions due to errors. Given the conditions of the channel, the inclusion of Forward Error Correcting (FEC) codes is strongly necessary given the conditions of the channel, as they provide error correction capability and avoid such critical circumstances.

FEC coding is a system of error control for data transmission, whereby the transmitter adds redundant data to its messages, so that a specific amount of random errors in the received bit sequences can successfully be corrected by the decoder. To make best use of the FEC coder, the possible error bursts due to momentary bad channel conditions or highly attenuated frequency bands must be minimized, and that is why the system must also include an interleaver block.

The channel coding field is a very active one, as there is a two-fold approach when designing an appropriate coding technique: first, it has to provide the desired error correction capability, and second, it has to provide

enough coding and decoding speed so as not to affect the transmission timing. There are different types of coders depending on the implementation:

1. Block codes: this family of codes work on fixed-size blocks (packets) of bits or symbols of predetermined size. Practical block codes can generally be decoded in polynomial time to their block length.
2. Convolutional codes: this family of codes work on bit or symbol streams of arbitrary length. They are most often decoded with the Viterbi algorithm, though other algorithms are sometimes used. Viterbi decoding allows asymptotically optimal decoding efficiency with increasing length of the convolutional code, but at the expense of exponentially increasing complexity.

As it has been mentioned above, there are numerous types of codes. Some of the most popular include the BCH (Bose, Ray-Chaudhuricodes and Hocquenghem code), which are known by its decoding ease, the Low Density Parity Check (LDPC) codes, which are highly-efficient block codes, and the Turbo codes, that combine multiple convolutional codes and an interleaver to produce a block code.

The type of error correcting code (ECC) that has been chosen is the BCH code, due to the following facts: its coding and decoding efficiency, the fact that it has been used in previous successful OFDM system implementations for underwater environments, and the implementation ease as it comes in a MATLAB built-in package.

The BCH codes are polynomial codes over a finite field with a particularly chosen generator polynomial from which the codewords are produced. It is also a cyclic code. These codes are multiple error correcting codes and a generalization of the Hamming codes.

The codewords are formed by taking the remainder after dividing a polynomial representing the information bits by a generator polynomial. The generator polynomial is selected to give the code its characteristics. All codewords are multiples of the generator polynomial [18].

For the practical implementation, a set of BCH codes with different redundancies and error capability has been tested. The characteristics of these codes are summarized in Tab. 5.1. Different channel utilization is possible depending on the chosen code, as the implementation allocates an integer number of codewords in each OFDM block for direct demodulation and decoding.

The ratio that assesses the channel utilization given a BCH code is  $N/(N + 1)$ , where  $N$  is the codeword length of the specific code. The system is designed so that  $K/(N + 1)$ , where  $K$  is the total number of subcarriers, is an integer. This ratio also represents the number of subcarriers that are not used, which are equispaced and may be used to carry pilots.

		BCH code								
		7/4	15/11	31/21	63/51	63/30	63/18	63/10	127/120	255/239
Coding ratio		1.75	1.36	1.48	1.24	2.10	3.50	6.30	1.06	1.07
Ch. utilization (%)		88	94	97	98	98	98	98	99	100
Correction (bits)		1	1	2	2	6	10	13	1	2

Table 5.1: BCH coding characteristics

To test the behavior of the selected codes, some Additive White Gaussian Noise (AWGN) has been artificially added to generated OFDM signals and the decoded Bit Error Rate (BER) has been evaluated and contrasted with theoretical curves (with positive matches). The results are shown in Fig. 5.4.

In practical experiments, the most appropriate BCH code has to be chosen by evaluating the achieved

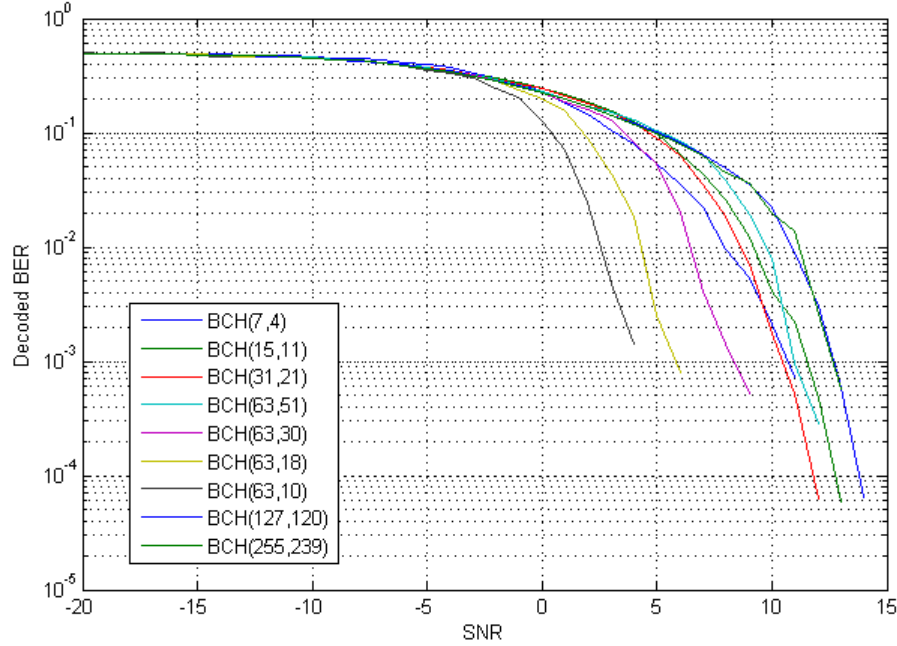


Figure 5.4: Decoded BER vs. SNR for an OFDM system with  $K=16384$ , 8-PSK subcarrier modulation, and AWGN

BER results for different coding ratios, such that the code with minimal redundancy that achieves a targeted decoding performance is selected (as illustrated in Sec. 8.3.2).

### 5.2.3 Subcarrier mapping

The modulations chosen in the current research to modulate the subcarriers are the Quadrature Amplitude Modulation (QAM) and the Phase Shift Keying (PSK) ones.

- Phase Shift Keying (PSK) is a digital modulation scheme that conveys data by changing, or modulating, the phase of a reference signal (the carrier wave). The constellation points chosen are usually positioned with uniform angular spacing around a circle.

These PSK types have been implemented (see constellation points in Fig. 5.5):

- Quadrature PSK (QPSK): Circle constellation of 4 points with 2 bits assigned to each point.
- 8-PSK: Circle constellation of 8 points with 3 bits assigned to each point.

Note that when differential detection is performed, the PSK mapped points are further processed to retrieve the transmitted constellation, including a  $45^\circ$  shift of the QPSK constellation, which is necessary to maintain the 4 points constellation (for more details on the differential detection algorithm and the transmitter modifications see Sec. 6.5.1).

- Quadrature Amplitude Modulation (QAM) is a digital modulation scheme that conveys data by changing, or modulating, both amplitude and phase of a reference signal. It is usually implemented as two amplitude modulation schemes for two added carriers, which are out of phase with each other by  $90^\circ$ .

These QAM types have been implemented (see constellation points in Fig. 5.6):

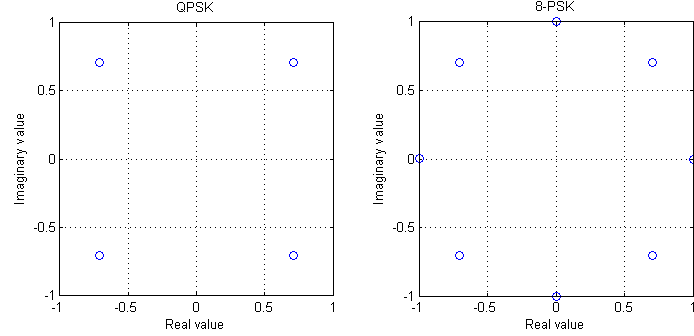


Figure 5.5: PSK modulation constellations

- 16-QAM: Squared constellation of 16 points with 4 bits assigned to each point.
- 32-QAM: Non-squared constellation of 32 points with 5 bits assigned to each point.
- 64-QAM: Squared constellation of 64 points with 6 bits assigned to each point.

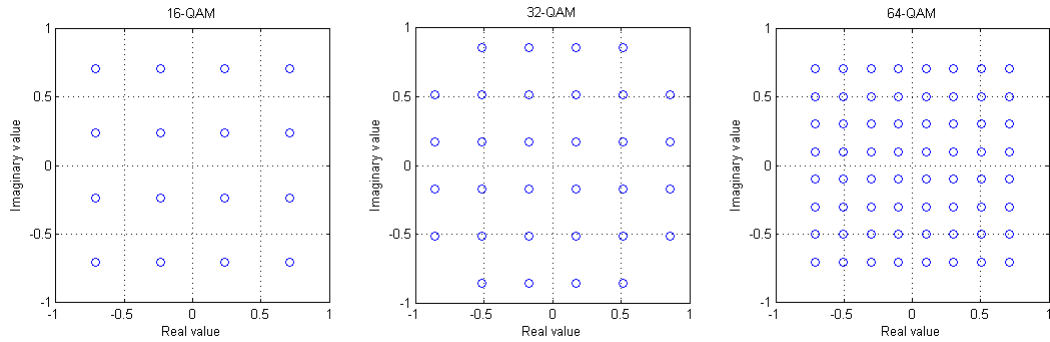


Figure 5.6: QAM modulation constellations

In practice, as higher is the density of points in the constellation, higher is the probability that the symbols are wrongly detected in the receiver due to the phase shift and amplitude scaling of the complex points after passing through the channel. That is why the performance of the different modulation types must be tested in the real conditions and appropriate constellations must be chosen (as shown in Sec. 8.3.3).

#### 5.2.4 Frequency interleaving

As it has been stated in the previous section, the error correction capability of channel coding techniques is optimized when combined with interleaving. In this case, the interleaving is performed in the frequency domain, across the  $K$  subcarriers. The concept of interleaving is graphically shown in Fig. 5.7.

The objective of the interleaving scheme is to separate as much as possible the different parts of a codeword (in this case the bits corresponding to the symbols in each subcarrier) in the frequency domain. It aims at reducing the impact of highly attenuated or distorted frequency bands due to channel characteristics such as multipath propagation or in-band noise, hence avoiding error bursts within a single codeword.

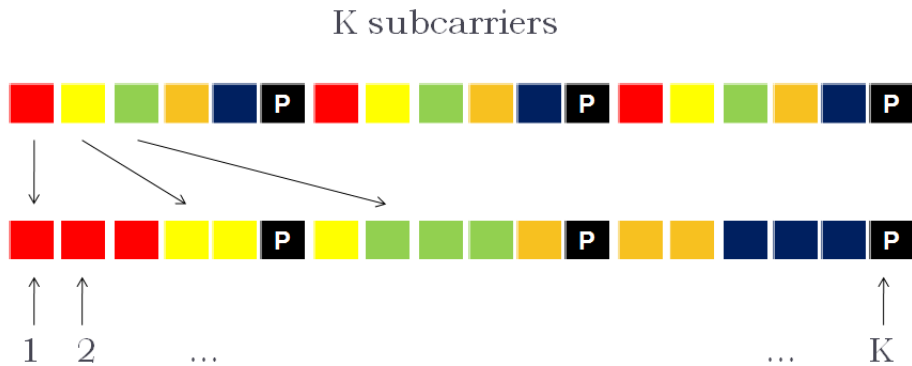


Figure 5.7: Interleaving concept. The data carriers are shown in different colors and the  $P$  channels represent pilots

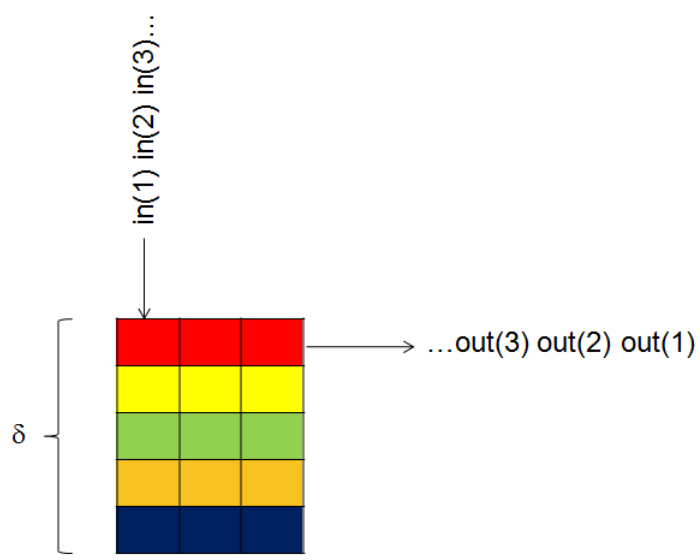


Figure 5.8: Interleaving matrix and interleaving depth

In the implemented system, the interleaving depth  $\delta$  (see Fig. 5.8), given in number of subcarriers, may be assessed from the following equation:

$$\delta = K \cdot \frac{N}{(N + 1) \cdot n_d} \quad (5.3)$$

where  $K$  is the total number of subcarriers,  $N$  is the codeword length, and  $n_d$  is a factor that indicates a certain number of symbols, that corresponds to an integer number of codewords. This last parameter is chosen in accordance to the detection algorithm, so that the symbol decision is optimized.

As a practical example, the designed interleaving depth  $\delta$  for a system with  $K = 16384$  subcarriers that uses a  $\text{BCH}(63,18)$  code is  $\delta = 256$  subcarriers. Considering a bandwidth of 115 kHz, it corresponds to a frequency band of 1.8 kHz.

### 5.2.5 IFFT modulation

Once the mapped subcarriers' symbols are interleaved, the OFDM temporal blocks are assessed using the IFFT algorithm. Despite it having been discussed in Sec. 4.3, a final consideration must be made about the practical implementation of this procedure.

As it may be expected, some oversampling is required in order to assure the correct demodulation of the OFDM blocks. According to the Nyquist sampling theorem, the sampling frequency,  $f_s$ , must accomplish the relation  $f_s > 2f_h$ , where  $f_h$  is the highest frequency component of the transmitted signal. In this case,  $f_h$  is the highest frequency of the band-pass signal (after frequency adjustment, see Sec. 5.2.8).

In the practical case, further oversampling is recommended due to the inherent complexity of underwater communications, and an oversampling ratio of between 3 and 4 is advised.

To correctly count for the oversampling, the IFFT algorithm does not operate with a number of samples  $K$  (the total number of subcarriers), but it operates with a number of samples  $\gamma K$ , where  $\gamma$  is the oversampling ratio, and  $(\gamma - 1)K$  zeros have been appended to the  $K$  subcarriers' symbols.

Thus, the IFFT algorithm performs the following equation:

$$y(l) = \sum_{k=0}^{N_s-1} \check{d}(k) e^{j2\pi kl/N_s}, \quad l = 0, \dots, N_s - 1 \quad (5.4)$$

where  $N_s$  is the number of samples during a symbol time, given by  $T f_s$ , and  $\check{d}(k)$  is a vector of  $N_s$  samples, which contains the subcarriers' symbols in the first  $K$  positions, and the  $(\gamma - 1)K$  appended zeros. The previous equation is efficiently calculated by multiplying the  $N_s$ -point IFFT of  $\check{d}(k)$  by  $N_s$ .

### 5.2.6 Peak to Average Ratio reduction

One of the major disadvantages in OFDM systems is its inherent difficulty to control the signal amplitude in the time domain. As the waveform shape is determined by the output of the IFFT applied to the subcarriers' symbols, which at the same time depend on the sequence of bits from the FEC coder (see Fig. 5.1), the shape of the signal can vary considerably from block to block.

The main consequence of this block-to-block variation is the existence of peaks in the signal that establish a limit in the maximum power of the transmitted signal. In other words, the peaks are transmitted at the maximum power and the rest of the signal is transmitted at a much lower power.

One of the possible suboptimal solutions for this problem is to assume a certain in-band distortion caused by the non-linear response of the chosen power amplifier. In this case, the amplifier input voltage is defined so that the peaks of the signal are transmitted with slightly higher power than the limit of the linear region of operation, thus gaining some power, but introducing distortion.

The present distortion is due to intermodulation products among subcarriers, and causes spectral growth of the multicarrier signal. As a result, the frequency synchronization is affected, and, as it has been previously commented, OFDM systems are very sensitive to these maladjustments.

Because of the importance of such issue in OFDM implementations, and being even more critical in underwater communications (where the attenuation caused by the channel is higher than in radio environments, and the signal amplitude is too weak), the reduction of the signal variation through time is a very active field of research. Such variation can be evaluated by the Peak to Average Ratio (PAR). The concept of PAR reduction is illustrated in Fig. 5.9.

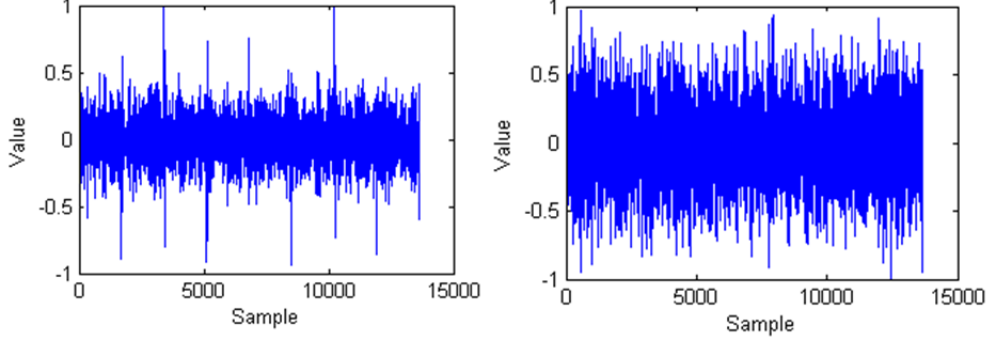


Figure 5.9: PAR reduction idea: original OFDM signal (left), and PAR reduced OFDM signal (right), using the symbol interleaving technique

The PAR of a signal is defined as the ratio between the maximal power of the signal and its average power, as

$$PAR = \frac{\max_{0 \leq t < T} |s(t)|^2}{\frac{1}{T} \int_0^T |s(t)|^2 dt} \quad (5.5)$$

where  $s(t)$  is the transmitted OFDM signal, and  $T$  is the symbol duration time. The PAR is also commonly given in dB, as  $10\log(PAR)$ .

Numerous techniques to reduce this ratio have been proposed in the last years. Some of the most popular ones are: clipping and filtering, symbol interleaving, in-band tone reservation, and out-of-band tone insertion.

All the previously mentioned techniques have been included in the current OFDM system, and the resulting PAR has been evaluated. In the following subsections these techniques are discussed, and its performance is tested and quantized.

### Clipping and filtering

The simplest technique that can be used to limit the PAR of a signal is the clipping and filtering technique. It is based on an amplitude clipping of the signal samples that are over a certain chosen threshold. The samples whose amplitude exceeds that threshold are clipped and the amplitude set to the maximum amplitude level, as

$$\bar{s}(t) = \begin{cases} s(t) & \text{if } |s(t)| \leq A \\ A \cdot e^{j\arg(s(t))} & \text{if } |s(t)| > A \end{cases} \quad (5.6)$$

The effects of the clipping are not only the reduction of the PAR, but a quantizable in-band and out-of-band distortion is introduced in the signal due to the variation of the signal in the time domain. It is at this point that filtering is advised to avoid the out-of-band distortion, so that no power is wasted by the hardware components.

Fig. 5.10 shows the implementation that has been selected. In it, the clipping is followed by a band-pass Finite Impulse Response (FIR) filter that effectively attenuates the components which are located outside the operational frequencies. A similar implementation and performance study is shown in [19]. Some other possible implementations include IFFT/FFT blocks to perform the filtering.

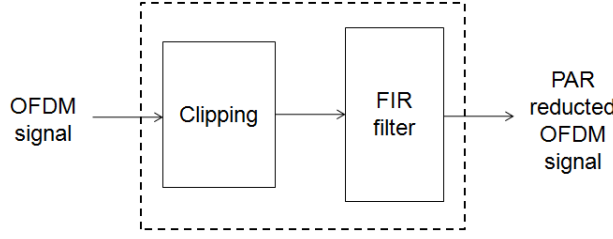


Figure 5.10: Clipping and filtering block diagram

Both the clipping threshold and the filter have been chosen according to practical tests, for which the performance of the detection algorithm has been tested for different filter type/parameters and clipping threshold values. Some of the selected parameters are summarized in Tab. 5.2.

Filter type	FIR
Order	128
Gain at $W_N$ (dB)	-6
Clipping threshold (%)	0.002

Table 5.2: Clipping and filtering parameters

The parameter  $W_N$  is used to represent the edges of the pass band, and the clipping threshold is defined as the percentage of samples that are clipped among the total number of samples of the OFDM signal. No amplitude value has been established as OFDM signals can vary, and the distortion that can be tolerated is correctly limited using the implemented solution.

### Symbol interleaving

The high correlation in the subcarriers' symbols that are used as input for the IFFT block has been demonstrated to cause high PAR signals. Due to that, several techniques have been designed so as to decorrelate

the complex points that have a direct impact on the time-domain shape of the signal. One of the most effective is the symbol interleaving technique.

In this technique, a set of  $M$  interleavers is used to reorder the symbols that are sent to the IFFT modulator. Given the  $K$  symbols that modulate the subcarriers,  $X = [X_0, X_1, \dots, X_{K-1}]$ , a one-to-one rearrangement,  $\{n\} \leftrightarrow \{\pi(n)\}$  where  $\pi(n) \in \{0, 1, \dots, K-1\}$ , results in the interleaved symbols,  $X = [X_{\pi(0)}, X_{\pi(1)}, \dots, X_{\pi(K-1)}]$  (Fig. 5.11 illustrates the concept). This procedure is performed for each interleaver, and hence the sequence with a lower PAR is selected for transmission [20].

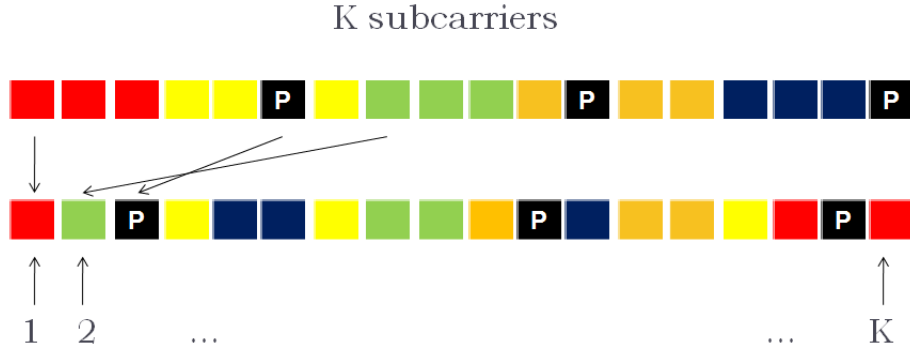


Figure 5.11: Symbol interleaving technique

One of the major concerns of this implementation has to do with the generation of the interleavers. As each OFDM signal is different, there is no exact method to know which kind of combinations will result in lower PAR. That is why  $M$  randomly generated combinations are used, being  $M$  a parameter that has to be set taking into account the practical performance of the system (in this case 32 interleavers has proved to provide enough improvement).

Another issue is the side information that should be transmitted to let the receiver know which interleaver has been used for each OFDM symbol. This problem is avoided in the current research project by using pilot symbols in each OFDM block (despite increasing the processing complexity).

The algorithm in reception calculates the Medium Square Error (MSE) between the pilot symbols that are retrieved from each interleaver and the transmitted pilot symbols (a parameter that is known by the receiver as it is set prior to transmission). Then, the receiver selects the interleaver that provides a lower MSE, as it is shown in Fig. 5.12.

Other possible interleaving implementations include the bit interleaving technique, where the bits, instead of the mapped symbols, are used as an input for the interleaving algorithm [20].

### In-band tone reservation

As it has been commented in the previous sections, the OFDM signal peaks are a direct consequence of the symbols used to modulate the transmitted signal. Thus, the rearrangement of these symbols (as in the interleaving method) successfully provides a PAR reduction to the OFDM signal if an appropriate change is made.

The in-band tone reservation technique aims at modifying the shape of the time-domain signal by selecting the symbols that will be transmitted on several subcarriers [21, 22], so that the PAR of the resulting OFDM signal is reduced. The main idea is quite similar to the previous technique's one in the sense that it makes

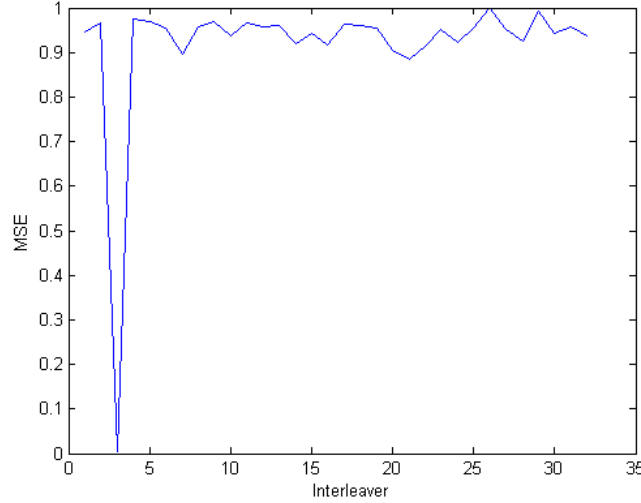


Figure 5.12: Interleaver detection. Normalized MSE with  $M=32$  interleavers (8-PSK,  $K=16384$ )

changes to the symbols in order to improve the PAR. However, in this case no side information is required (nor further receiver complexity), because the selected subcarriers do not bear data information.

In the current research, the PAR-reducing subcarriers for the in-band tone reservation technique are equispaced, and are the ones that remain unused and may be configured as pilots with other setups (as explained in Sec. 5.2.2). The concept is illustrated in Fig. 5.13.

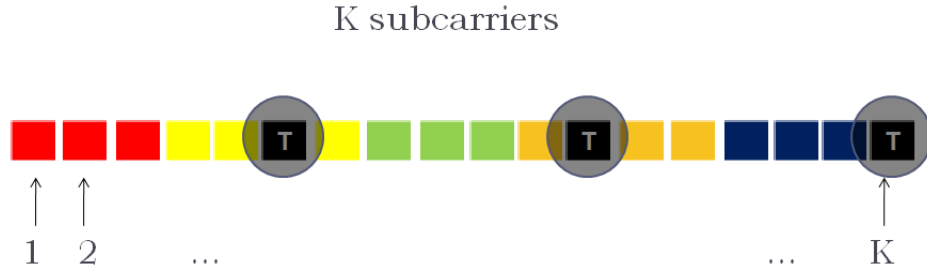


Figure 5.13: In-band tone reservation concept. The control tones are circled and marked with a “T”

The PAR control tones are decided among a number  $M$  of randomly generated control symbols' sequences. The algorithm selects the sequence of control tones that provides the best OFDM signal PAR. Again, there are some parameters that can be optimized to provide the best performance.

One is the number of sequences,  $M$ , which results in higher improvement as more random sequences are used. In the current system implementation,  $M = 32$  has been chosen as it provides an appropriate performance and do not imply a high transmitter complexity.

Another parameter to take into account is the constellation from which the control symbols are taken. Some experiments have been done with similar results for different constellation points, so that the same constellation as the one used for the transmitted data symbols is used.

### Out-of-band tone insertion

In this technique, an out-of-band control signal is generated apart from the original multicarrier OFDM signal. The purpose of this method is to provide the targeted PAR reduction once both the control signal and the data bearing signal are added. A block diagram of this implementation is shown in Fig. 5.14.

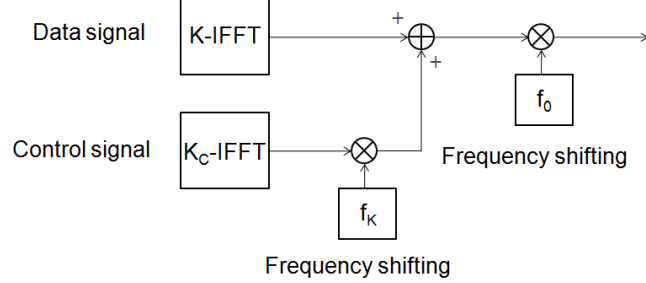


Figure 5.14: Out of band tone insertion (OTI) block diagram

The control signal outside the useful bandwidth is given by

$$s_c(t) = \sum_{k=0}^{K_c-1} c_k e^{j2\pi(K+k)\Delta f t}, \quad t \in [0, T] \quad (5.7)$$

where  $K$  is the total number of subcarriers inside the useful bandwidth,  $c_k$  are the control tones, and  $K_c$  is the number of control tones. The control tones are placed immediately above the useful bandwidth, as it is the configuration that has been proven to work more effectively [23]. An example Power Spectral Density (p.s.d.) of the resulting signal is shown in Fig. 5.15.

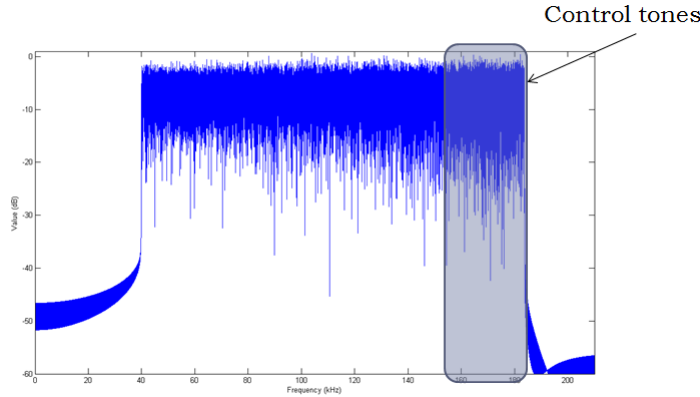


Figure 5.15: Power Spectral Density (p.s.d.) of an OFDM signal with random OTI

The main issue while implementing the Out-of-band Tone Insertion (OTI) technique is the selection of the control tones. There exists an optimal method to assess the control coefficients,  $c_k$ , as well as a suboptimal gradient technique algorithm that aims to compute the control sequence with a lower complexity (both of them data-dependent [23]). Nonetheless, in the current system implementation they have proven to require too much computing time (e.g. one hour for a 10-second OFDM signal with  $K=16384$ ,  $B=115$  kHz and the gradient technique).

Due to the high computational complexity of the data dependent methods, a matrix of randomly generated control sequences has been designed. Again, the sequence that provides a higher improvement is selected, and the number  $M$  of control sequences is chosen to result in an appropriate performance and a low degree of computational complexity (in the current research 128 control sequences are used).

Another key decision must be made regarding the number of control tones. After some tests were done, a number of control tones higher than 12% the number of in-band subcarriers has proved to be necessary. Moreover, the constellation, or modulation alphabet, that is used to modulate the control tones can be selected. Again, it has been set to the data carriers' one.

The main advantage of the OTI technique is the fact that no side information must be transmitted along with the data information, so that there is no data rate loss at any targeted PAR reduction capability.

The main drawback of this method is the power loss while amplifying the signal, as the control tones do not carry useful information but must be amplified in order to take advantage of the achieved low PAR. Once the signal comes out of the amplifier, the control tones can be removed by filtering, so that the signal that is transmitted only occupies the useful bandwidth.

In the current research, the last filtering is done by the transducer response, which highly attenuates the signal past the highest subcarrier frequency.

## Performance

Different PAR techniques have been applied to a compressed video file while generating the transmission OFDM signal, and the performance of the implemented PAR reduction methods has been evaluated.

To measure the PAR improvement capability of the different techniques, the Complementary Cumulative Distribution Function (CCDF) is used. It represents the probability that the resulting PAR is above a certain threshold,  $\text{Prob}(\text{PAR} > \text{PAR}_0)$ .

The CCDF has been evaluated over the total number of generated OFDM blocks, and the results are shown in Fig. 5.16.

It must be noted that the best performance is achieved with symbol interleaving technique, while the tone reservation method and the OTI random technique achieve similar results with the selected parameters. Lastly, the clipping effect can be seen in the clipping and filtering method's curve (a fast decay is observed at the point where clipping occurs).

### 5.2.7 Synchronization and guard time

Time synchronization in an OFDM system is extremely important in order to correctly locate the OFDM blocks for demodulation. Its purpose is to provide the correct timing for the system to retrieve the transmitted data, thus avoiding any Inter-Symbol Interference (ISI), or even a completely wrong detection due to an inaccurate synchronization.

In the current implementation, proper timing information is retrieved from the synchronization preamble, which is based on a pseudo-random sequence of bits whose length is 127. It is quadrature modulated using the center frequency of the desired band, and its time duration is given by  $127/B$ , where  $B$  is the total bandwidth.

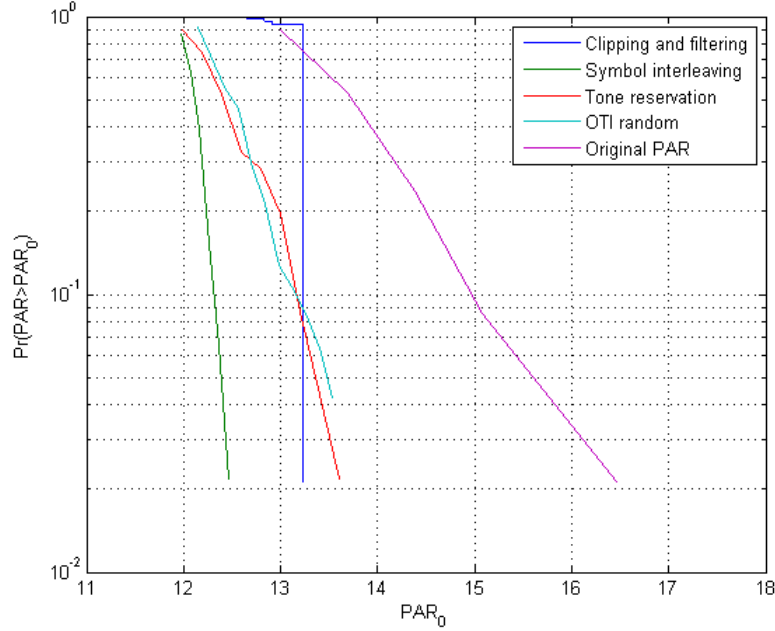


Figure 5.16: CCDF of an OFDM signal for different PAR techniques (8-PSK,  $K=16384$ ,  $B=115$  kHz)

The synchronization preamble is transmitted with the highest power to maximize the probability of detection, and it is also designed to have good correlation properties (only a main peak is the result of an autocorrelation of the modulated synchronization preamble). A preamble example with its autocorrelation is shown in Fig. 5.17.

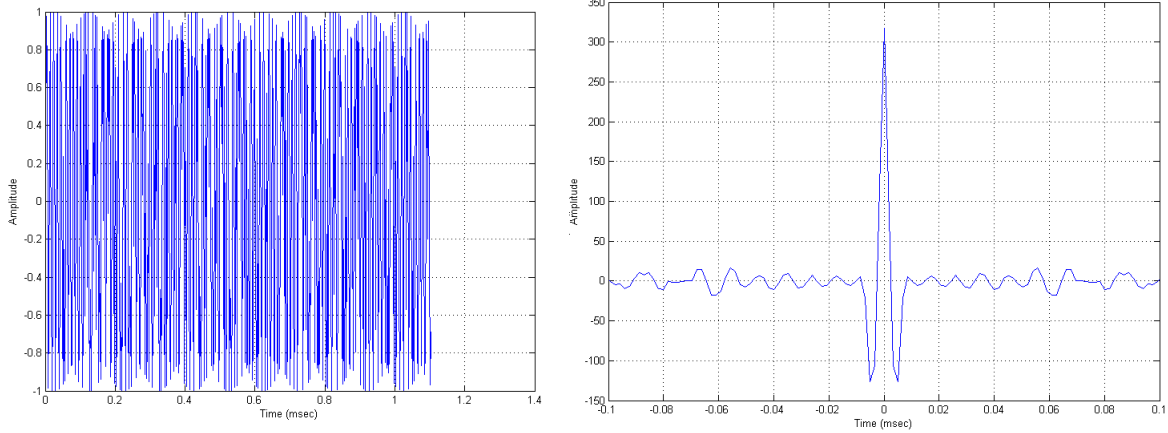


Figure 5.17: Synchronization preamble (left), and its autocorrelation (right)

The implementation also allows for resynchronizations within a single file transmission, so that after a specific amount of time another synchronization preamble is transmitted to reacquire the signal timing.

Another important fact to take into account when generating an OFDM signal is the capacity to absorb the multipath propagation due to channel characteristics. There may be situations when the channel impulse response is lower than 5 msec, and others when some arrivals are observed 10 msec later than the main one. The ability to avoid the ISI caused by the overlap of one symbol with the latest arrivals of the previous one

is determined by the guard time,  $T_g$ .

Typical coherence times for the underwater channel are of several milliseconds, being 2 msec the observed time for the majority of the practical underwater experiments conducted during this research. That is why a guard time of 10 msec has been chosen to avoid any ISI interference.

Some transmitted and received signal plots that illustrate the multipath propagation effects on the signals are shown in Fig. 5.18. In the time-domain plots the vertical axis shows the amplitude of the signal, and in the frequency domain plots the horizontal axis shows the time, the vertical axis shows the frequency, and the color shows the power of the signal (yellow designates higher power, and purple lower power).

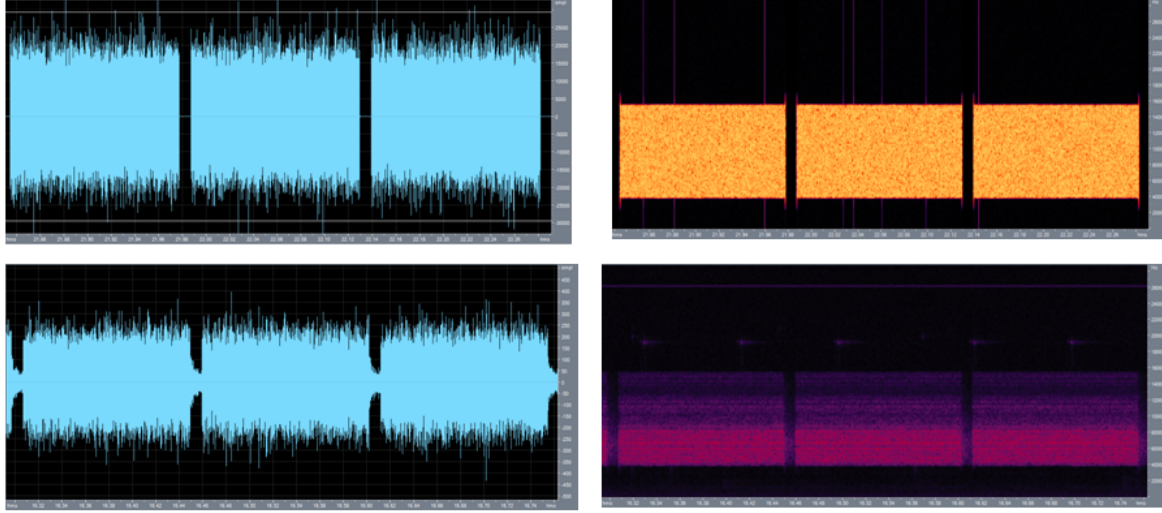


Figure 5.18: Transmitted time domain signal (top left), received time domain signal (bottom left), transmitted frequency domain signal (top right), and received frequency domain signal (bottom right)

### 5.2.8 Frequency adjustment

Despite underwater communications are not yet regulated, the generated baseband OFDM signals need to be shifted in frequency to the desired frequency band to avoid the noise present in the channel at low frequencies. However, the usable frequency band can not be extended beyond the limits given by the attenuation curves (as it has been commented in Chap. 2).

In practice, the frequency band is chosen after some field measurements are done, so that the specific attenuation under practical conditions and possible external noise sources are determined. Moreover, hardware characteristics must be taken into account, specifically the transducer-hydrophone frequency responses.

Regarding the noise, the lowest possible subcarrier frequency for the experimental underwater tests has been set to 40 kHz. Considering the attenuation and, in this case, the transducer non-flat frequency response (see Fig. 7.8), the highest possible subcarrier frequency has been set to 155 kHz.

The total available bandwidth for communication purposes is then set to 115 kHz in this practical situation, which provides more than enough frequency range to achieve high data rates.

To illustrate the frequency shift, the power spectral density (p.s.d.) of a sample transmitted OFDM signal before and after the shift is plotted in Fig. 5.19. Finally, the resulting signal which is sent to the

transmitter circuitry is shown in Fig. 5.20.

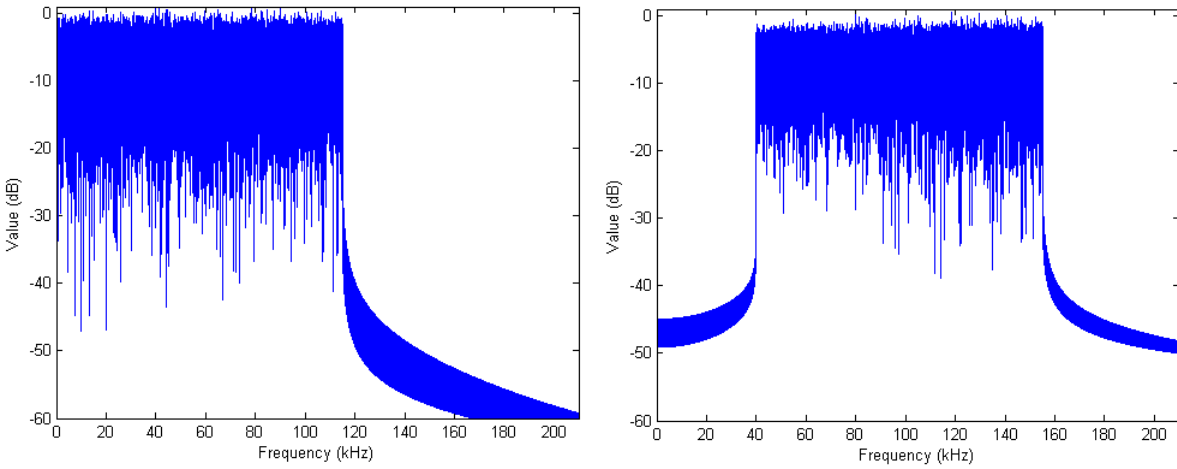


Figure 5.19: OFDM signal p.s.d. ( $K=16384$ , 8-PSK,  $B=115\text{kHz}$ ) before frequency adjustment (left) and after (right)

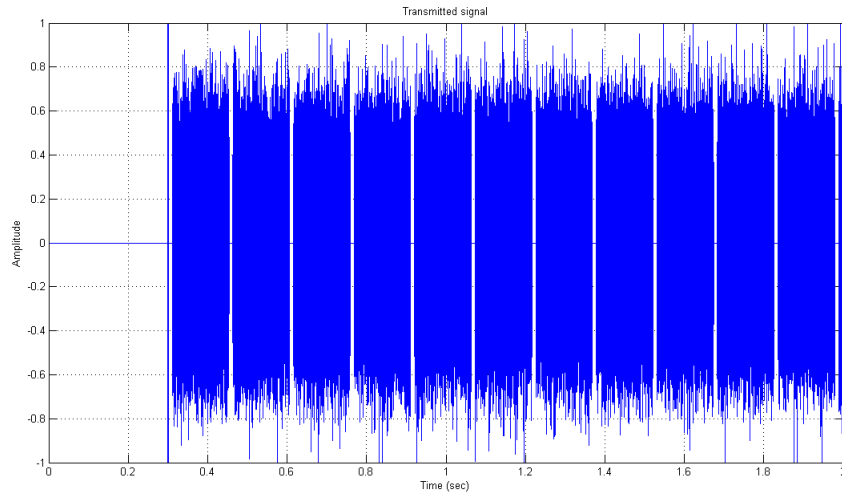


Figure 5.20: Sample transmitted OFDM signal with  $K=16384$ , 8-PSK, and  $B=115\text{kHz}$ . Synchronization preamble and OFDM blocks



# Chapter 6

## OFDM receiver

The OFDM system receiver is designed according to the characteristics of the underwater channel. The frequency selectivity, the non-uniform Doppler Effect, and the time-varying multipath in the considered channel is taken into account to choose the most appropriate techniques.

The implemented system is introduced and the most important parts are explained in depth. In addition, the methods to quantify the performance of the system are commented.

### 6.1 Receiver design

The OFDM system receiver has been designed according to the transmitter model commented in Sec. 5.1, and its block diagram is the one shown in Fig. 6.1.

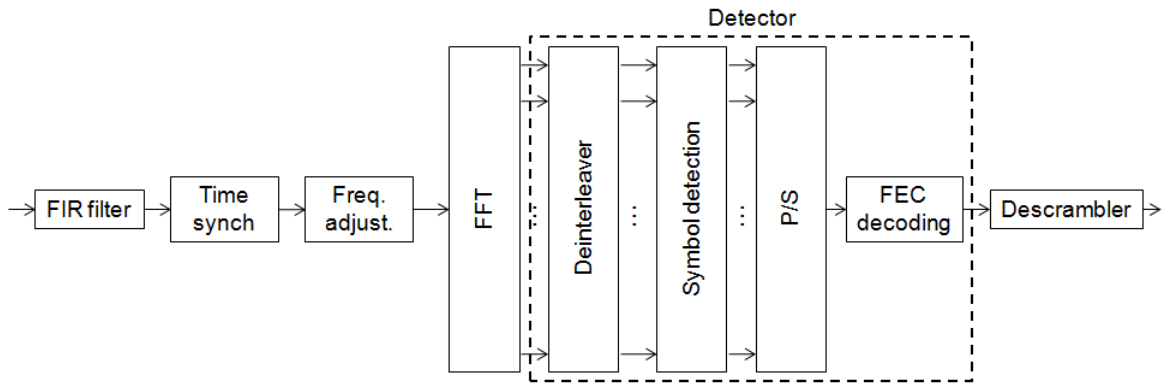


Figure 6.1: Receiver scheme

Once the receiving side hardware receives the OFDM signal from the channel, some band-pass FIR filtering is applied to it in order to assure a successful synchronization and minimize the out band noise. After the filtering is performed, a time synchronization algorithm provides an accurate reference for the reception of the OFDM blocks.

It must be noted that the synchronization is performed before converting the signal to baseband, although

it could be done after the signal is shifted to baseband without a change in the achieved results.

It is at that point that the OFDM blocks are downshifted in frequency, and the FFT demodulation calculates the complex raw constellation points.

The detector performs the post-FFT algorithm to retrieve the constellation points by cancelling the channel effects. In it, the deinterleaving, parallel-to-serial conversion and FEC decoding are included, so that the output is directly a sequence of detected scrambled bits. All the mentioned blocks are included inside the detector to decrease the implementation complexity, as the coherent detector algorithm performs a coding-oriented detection to better estimate the channel (see Sec. 6.5.2).

Finally, the descrambler assesses the detected bits (which in the case of the video files are passed to the MPEG-4 decoder to display the detected video).

## 6.2 FIR filtering

The selected band-pass filter is designed according to the signal useful bandwidth and it aims to remove the out-of-band noise so that the signal looks clean before applying the synchronization technique. Despite the signal did not present much interference in the experimental readings, it is highly recommendable to include this kind of filter, as other transmissions or external noise sources could affect the signal shape due to out-of-band components.

The type of filter and the key parameters are shown in Tab. 6.1. The parameter  $W_N$  is used to represent the edges of the pass band (as in the filter used to clip and filter in Sec. 5.2.6), as

$$W_N = [f_{low}, f_{high}], \text{ where } f_{low} = \frac{F_0 - 0.055B}{F_s}, \text{ and } f_{high} = \frac{F_{K-1} + 0.055B}{F_s} \quad (6.1)$$

where  $B$  represents the useful bandwidth of the OFDM signal,  $F_0$  and  $F_{K-1}$  represent the first and last subcarrier frequencies,  $F_s$  is the sampling frequency, and the calculated edges,  $W_N$ , are digital frequencies in the range [0...1/2].

Filter type	FIR
Order	128
Gain at $W_N$ (dB)	-6

Table 6.1: Filter parameters

To illustrate the effects of the implemented filtering, the power spectral densities (p.s.d) of the received signal and the transfer function of the filter is shown in Fig. 6.2, and a sample received signal before and after filtering can be seen in Fig. 6.3.

## 6.3 Time synchronization

The synchronization algorithm that has been included in the OFDM system receiver consists of a cross-correlation computation between the received signal after the FIR filtering application and the synchronization preamble (which is known at the receiver end).

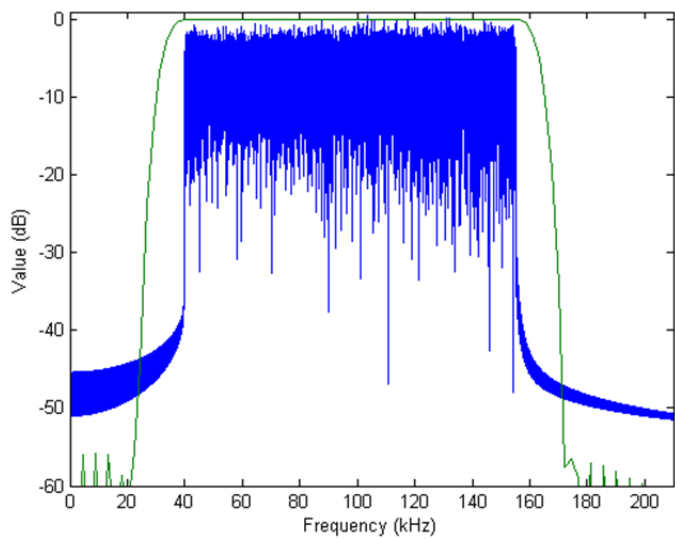


Figure 6.2: Power spectral density (p.s.d.) of the received signal and the FIR filter response ( $B=115$  kHz). The vertical axis indicates the signal power related to the maximum power in dB

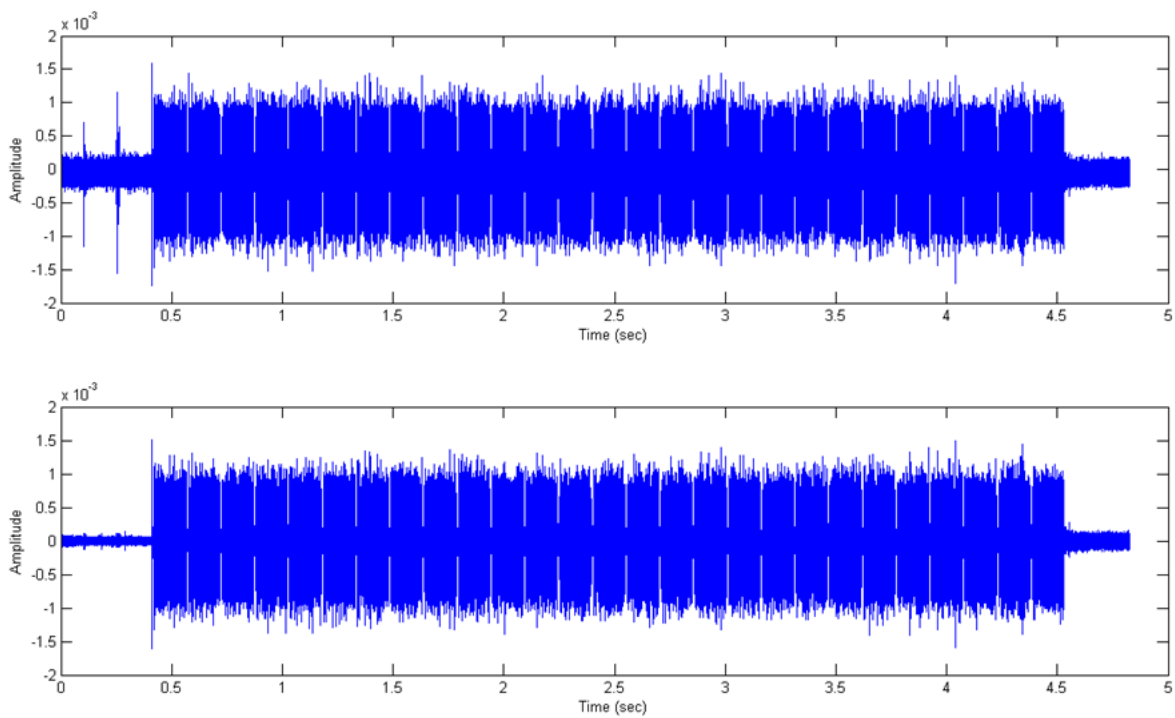


Figure 6.3: Received signal before filtering (top), and after filtering (bottom) with  $B=115$  kHz, 8-PSK,  $K=16384$

Due to the properties of the selected preamble (see Sec. 5.2.7), the result of the cross-correlation algorithm shows a high peak where the preamble is detected in the received signal, with high probability (if no in-band and high distorting noise is present).

The cross-correlation is computed for a length of  $N_{synch} + N_{pause}$ , where  $N_{synch}$  is the number of samples of the synchronization preamble, and  $N_{pause}$  is the number of samples between the preamble and the first OFDM block. The implementation selects the start of the received portion of signal to synchronize by checking the amplitude of the signal. When the signal reaches a 70% of its highest value, it is assumed that in this part the synchronization preamble is received.

The results of the synchronization algorithm for a sample received signal in a 200 meters underwater link are shown in Fig. 6.4.

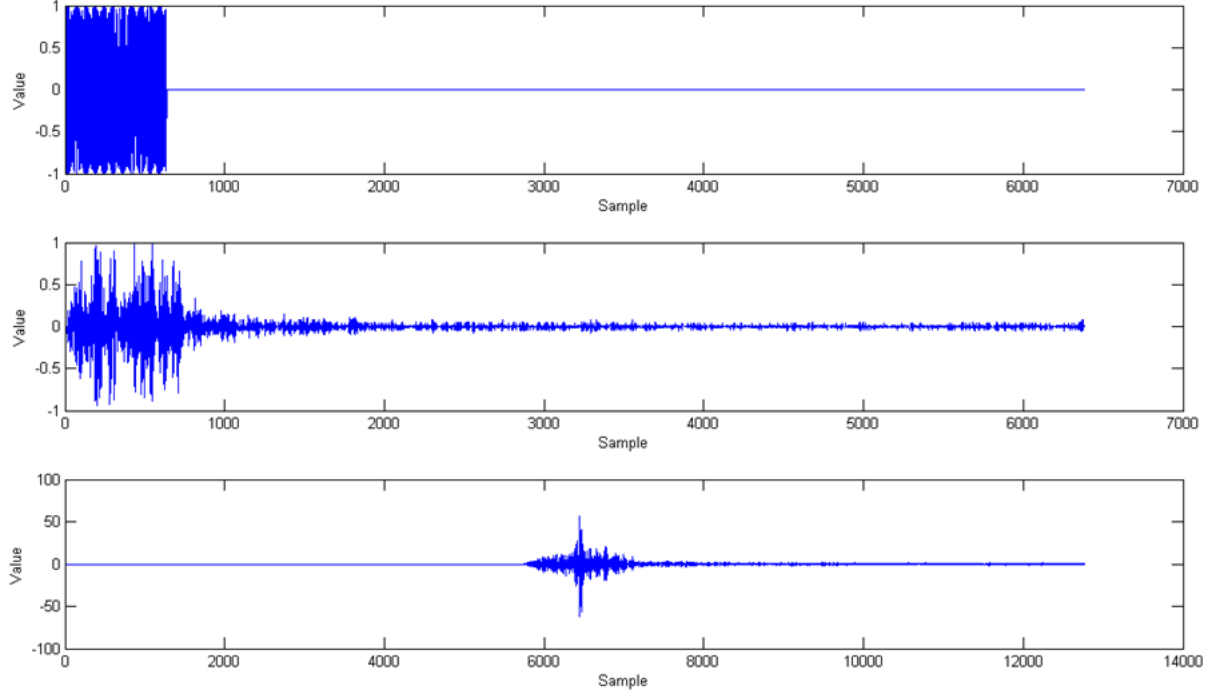


Figure 6.4: Synchronization preamble followed by a pause (top), received signal after filtering used as the input of the synchronization algorithm (center), and cross-correlation between preamble and signal (bottom). OFDM parameters:  $B=115$  kHz, 8-PSK,  $K=16384$

## 6.4 FFT demodulation

The FFT algorithm is used to retrieve the subcarriers' received symbols before channel treatment, by using the complementary method to the IFFT modulator. The applied equation is

$$y(k) = \sum_{l=0}^{N_s-1} s_r(l) e^{-j2\pi kl/N_s}, \quad k = 0, \dots, N_s - 1 \quad (6.2)$$

where  $N_s$  is the number of samples during a symbol time, and  $s_r(l)$  is the received sampled signal. An

efficient implementation is possible by computing the  $N_s$ -point FFT of the received signal  $s_r(l)$ .

As it has been commented in Sec. 5.2.5, the signal is oversampled by a factor  $\gamma$ , which means that the retrieved signal after FFT demodulation includes the  $K$  subcarriers received symbols plus  $(\gamma - 1)K$  appended zeros (which may not be zeros at the receiver due to the channel response and noise). That is why, to retrieve the useful part of the signal  $y(k)$ , the first  $K$  values are chosen and passed to the post-FFT detection algorithms.

A sample constellation is shown in Fig. 6.5. The channel and noise effects are not yet treated by the post-FFT algorithms, and hence the transmitted 8-PSK subcarrier constellation points can not be retrieved at this point.

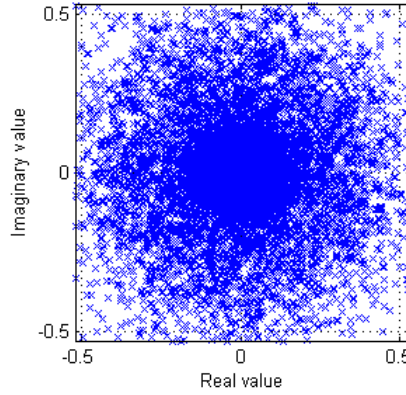


Figure 6.5: Constellation after FFT demodulation. Link: 200m, underwater. OFDM parameters:  $B=115$  kHz, 8-PSK,  $K=16384$

## 6.5 Detection

The current system implementation includes two types of detectors: a differentially coherent detector based on a differential detection among the subcarriers, and a coherent detector based on the calculation of phase and channel estimates used to correct the effects of the Doppler-distorting, multipath channel.

### 6.5.1 Differentially coherent detector

The differentially coherent algorithm used to successfully detect the data transmitted on the received OFDM blocks is based on a differential detector that does not rely on the retrieval of phase and channel estimates. This fact is in stark contrast to the coherent detection algorithms, which are based on the assumption of a block-to-block dependency for the assessment of the detection estimates, thus providing a detection technique that can deal with sudden channel changes or high motion (which could cause a coherent detector to lose track from then on).

#### Algorithm Description

**Transmitter** The differential detector algorithm requires further encoding of the transmitted constellation. That is, given the subcarrier mapped symbols for each block,  $b_k(n)$ , the transmitting side coder calculates

the differentially encoded symbols that must be transmitted for each subcarrier,  $d_k(n)$ , as

$$d_k(n) = d_{k-1}(n)b_k(n), \quad k = 0, \dots, K - 1 \quad (6.3)$$

where the first subcarrier symbol is initialized as  $d_{-1}(n) = 1$ . Note that the input QPSK symbols,  $b_k(n)$ , need to be on + constellation to assure that only 4 possible complex points are the output of the differential coder (also in + constellation). Thus, a  $45^\circ$  shift is required from the mapped constellation. Sample differential encoded constellations are shown in Fig. 6.6.

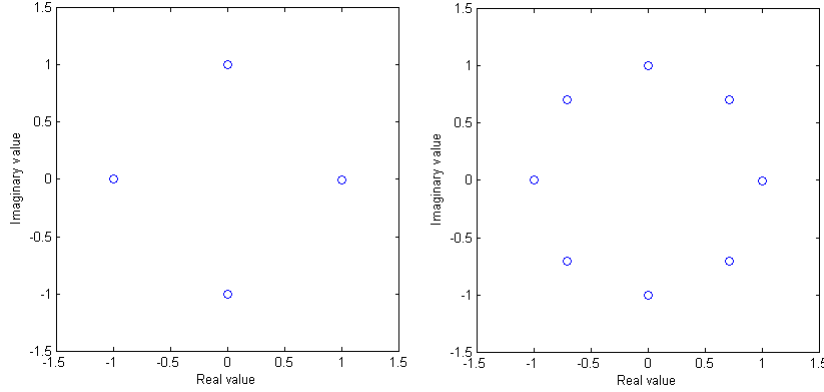


Figure 6.6: Differential encoded QPSK constellation (left) and 8-PSK constellation (right)

After the differential coding is performed, the  $d_k(n)$  symbols are passed to the IFFT modulator (Sec. 5.2.5).

**Receiver** The receiver gets the subcarriers' complex points in the OFDM blocks contained in the received signal, once the FFT demodulation is performed. The received values,  $y_k(n)$ , can be decomposed as

$$y_k(n) = H_k(n)d_k(n)e^{j\theta_k(n)} \quad (6.4)$$

where  $H_k(n)$  represents the channel effect (a complex value for each block  $n$  and subcarrier  $k$ , containing the amplitude attenuation and the phase shift), and  $\theta_k(n)$  represents the phase shift due to the motion-induced Doppler effect.

As it can be easily retrieved from the previous equation, taking into account the assumption that the channel estimates,  $H_k(n)$ , and the phase estimates,  $\theta_k(n)$ , are similar between adjacent subcarriers, the mapped symbols,  $b_k(n)$ , can be extracted by applying the following equation:

$$\frac{y_k(n)}{y_{k-1}(n)} = \frac{H_k(n)d_k(n)e^{j\theta_k(n)}}{H_{k-1}(n)d_{k-1}(n)e^{j\theta_{k-1}(n)}} \approx \frac{d_k(n)}{d_{k-1}(n)} = b_k(n) \quad (6.5)$$

In the case that multiple receivers are used, an average between the points obtained with all of them is performed. A sample detected constellation is shown in Fig. 6.7, before and after the decision is made.

A couple of last comments must be made about the differential detector, regarding (1) the data rate of a differential detection transmission and (2) the possible input constellations.

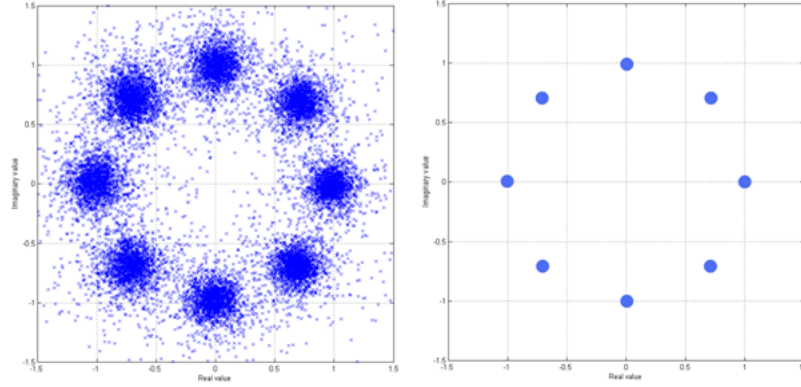


Figure 6.7: Detected constellation (left) and decided values (right) with differential detection. OFDM parameters:  $B=115$  kHz, 8-PSK,  $K=16384$

Regarding (1), the fact that there is one subcarrier in each OFDM block used to initialize the algorithm directly implies that there is one subcarrier unused in the OFDM transmission. In the practical implementation, there is no reduction in data rate for the implemented system as a pilot is relocated on that first subcarrier to avoid the loss in data rate.

Finally, with reference to (2), the differential detector can only be used with PSK constellations, as the applied algorithm does not take into account amplitude differences, and the encoding scheme is not designed to deal with QAM constellations (the differentially encoded symbols would result in a sequence of complex points with gradually increasing amplitude).

### 6.5.2 Coherent detector

The coherent algorithm used to perform the detection of the received OFDM blocks is the *Low Complexity OFDM Detector for Underwater Acoustic Channels* [15]. It is an adaptive algorithm for OFDM signal detection on Doppler-distorted, time-varying multipath channels. It focuses on a low complexity post-FFT signal processing using adaptive channel estimation over the blocks. Non-uniform Doppler compensation across subbands is performed using a single adaptively estimated parameter representing the Doppler rate for each block.

#### Algorithm Description

After the application of the FFT algorithm, the received symbol values for each subcarrier  $k$  in the block  $n$ ,  $\mathbf{y}_k(n)$ , are stored as a column vector that contains the complex points for each receiving element. Once these values are assessed, the algorithm performs the following steps (experimental underwater detection examples are provided in the referenced figures):

- Assessment of a first data estimate  $\hat{d}_{k1}(n)$  using MMSE combining of the different receivers for each subcarrier  $k$  in the block  $n$ . To do so, it uses the phase offset  $\hat{\theta}_k(n-1)$  and the channel frequency-domain coefficient  $\hat{\mathbf{H}}_k(n-1)$  calculated in the previous block, along with a normalization parameter  $\hat{\gamma}_k(n-1)$  according to the amplitude of the channel coefficient (see Fig. 6.8).

$$\hat{d}_{k1}(n) = \hat{\gamma}_k(n-1) \hat{\mathbf{H}}'_k(n-1) \mathbf{y}_k(n) e^{-j\hat{\theta}_k(n-1)} \quad (6.6)$$

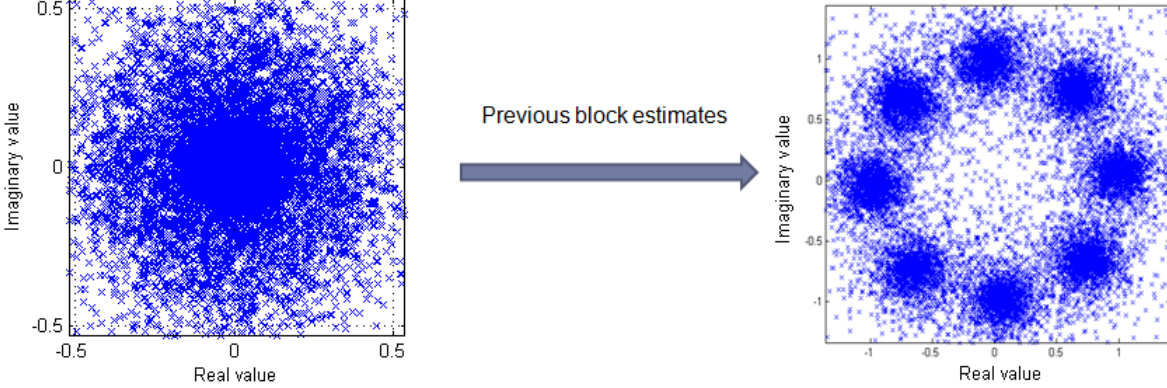


Figure 6.8: Constellation after FFT (left), and  $\hat{d}_{k1}$  estimates (right) for an OFDM signal with  $K=16384$ ,  $B=115$  kHz, and 8-PSK subcarrier modulation

2. Calculation of an angular offset  $\Delta\hat{\theta}_k(n)$  between the assessed  $\hat{d}_{k1}(n)$ , and either the pilot symbols that were transmitted in the block, or a second estimate that corrects the block-to-block motion by using the Doppler coefficient from the last block. The performed steps are:

(a) (if no pilots are included) Retrieval of the estimate  $\hat{d}_{k2}(n)$ , given by the following equation:

$$\hat{d}_{k2}(n) = \hat{\gamma}_k(n-1)\hat{\mathbf{H}}'_k(n-1)\mathbf{y}_k(n)e^{-j\check{\theta}_k(n)} = \hat{d}_{k1}(n)e^{-j\hat{a}(n-1)\omega_k T'} \quad (6.7)$$

(b) Calculation of the reference for the angular offset measurement,  $\bar{d}_k(n)$ . Considering that  $d_k(n)$  are the transmitted symbols, and  $\tilde{K}(n)$  is the pool of pilot subcarriers, it is given by

$$\bar{d}_k(n) = \begin{cases} d_k(n) & \text{if } k \in \tilde{K}(n) \\ \text{decision}[\hat{d}_{k2}(n)] & \text{otherwise} \end{cases} \quad (6.8)$$

(c) Finally, the angular offset is assessed by evaluating the following scalar product:

$$\Delta\hat{\theta}_k(n) = \langle \hat{d}_{k1}(n) \bar{d}_k^*(n) \rangle \quad (6.9)$$

3. Assessment of the Doppler coefficient  $\hat{a}(n)$  (Fig. 6.9) from the angular offsets  $\Delta\hat{\theta}_k(n)$  by calculating the mean over the considered channels (being  $K$  the total number of subcarriers).

$$\hat{a}(n) = \frac{1}{K} \sum_{k=0}^{K-1} \frac{\Delta\hat{\theta}_k(n)}{\omega_k T'} \quad (6.10)$$

Alternatively, the implementation can use only the pilot channels for phase tracking purposes, so that the  $\hat{d}_{k2}(n)$  estimate do not have to be computed, and the previous mean,  $\hat{a}(n)$ , is performed over the pilot subcarriers.

4. Calculation of the phase offset  $\hat{\theta}_k(n)$  (Fig. 6.10) for each subcarrier using the Doppler coefficient  $\hat{a}(n)$ .

$$\hat{\theta}_k(n) = \hat{\theta}_k(n-1) + \hat{a}(n)\omega_k T' \quad (6.11)$$

5. Retrieval of a second more accurate data estimate,  $\hat{d}_k(n)$ , using MMSE combining of the different receivers for each subcarrier  $k$  in the block. This estimate includes the correction of the possible tilt of the constellation due to the motion-induced Doppler distortion (see Fig. 6.11).

$$\hat{d}_k(n) = \hat{\gamma}_k(n-1)\hat{\mathbf{H}}'_k(n-1)\mathbf{y}_k(n)e^{-j\hat{\theta}_k(n)} = \hat{d}_{k1}(n)e^{-j\hat{a}(n)\omega_k T'} \quad (6.12)$$

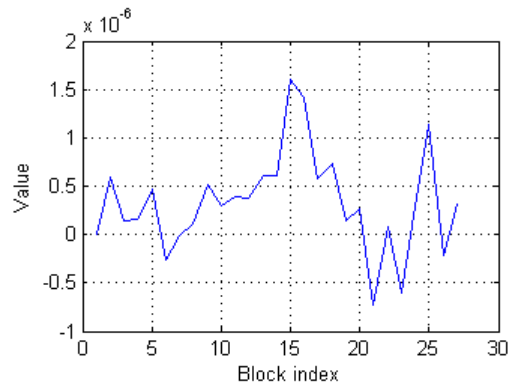


Figure 6.9:  $\hat{a}$  estimates for an OFDM signal with  $K=16384$ ,  $B=115$  kHz, and 8-PSK subcarrier modulation

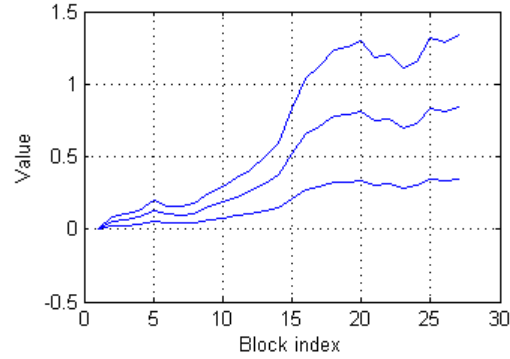


Figure 6.10:  $\hat{\theta}_k$  estimates in radians for an OFDM signal with  $K=16384$ ,  $B=115$  kHz, and 8-PSK subcarrier modulation. The plot includes the estimates for  $k=0$ ,  $k=8191$  and  $k=16383$

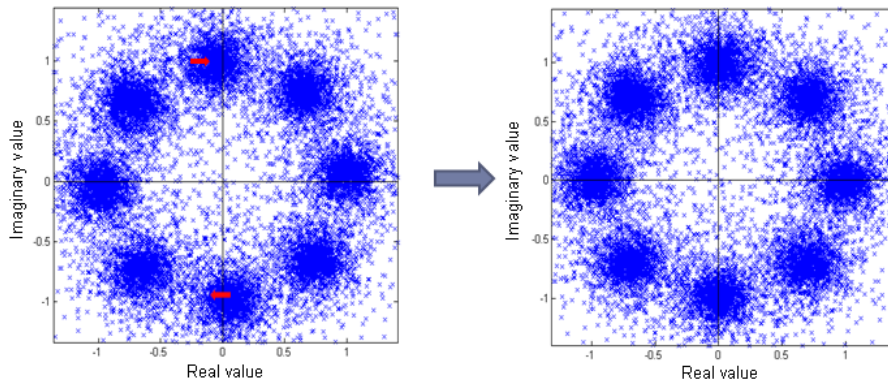


Figure 6.11:  $\hat{d}_{k1}$  estimates (left) and phase corrected  $\hat{d}_k$  estimates (right) for an OFDM signal with  $K=16384$ ,  $B=115$  kHz, and 8-PSK subcarrier modulation

6. Coding-oriented detection. The symbols are detected in blocks of multiple codewords so that the data bits can be directly retrieved and some errors corrected (see Fig. 6.12).

$$\tilde{d}_k(n) = \begin{cases} d_k(n) & \text{if } k \in \tilde{K}(n) \\ \text{decision}[\hat{d}_k(n)] & \text{otherwise} \end{cases} \quad (6.13)$$

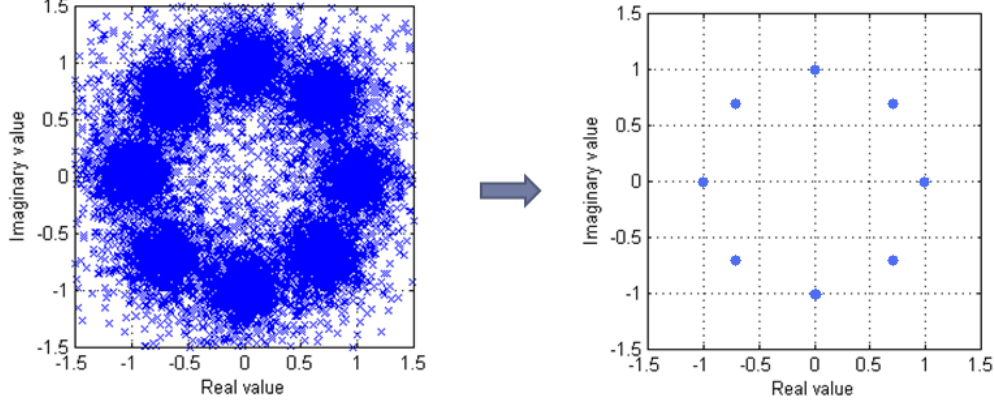


Figure 6.12: Phase-corrected  $\hat{d}_k$  estimates (left) and symbol decisions (right) for an OFDM signal with  $K=16384$ ,  $B=115$  kHz, and 8-PSK subcarrier modulation

7. Calculation of the channel estimates  $\hat{\mathbf{H}}_k(n)$  as explained in the next section.
8. Assessment of the normalization parameters  $\hat{\gamma}_k(n)$  from the received values  $\mathbf{y}_k(n)$ , the assessed phase offsets  $\hat{\theta}_k(n)$ , and the second set of data estimates  $\hat{d}_k(n)$ . A high SNR regime is supposed, so the noise variance  $\sigma_z^2$  is omitted.

$$\hat{\gamma}_k(n) = \left( \sigma_z^2 + \hat{\mathbf{H}}'_k(n) \hat{\mathbf{H}}_k(n) \right)^{-1} \approx \left( \hat{\mathbf{H}}'_k(n) \hat{\mathbf{H}}_k(n) \right)^{-1} \quad (6.14)$$

The algorithm is initialized using  $\hat{\mathbf{H}}_k(1) = \mathbf{y}_k(1)d_k^*(1)$ ,  $\hat{a}(1) = 0$  and  $\hat{\theta}_k(1) = 0$ . For a correct performance, the receiver must know the transmitted symbols  $d_k(1)$  to accurately initialize the channel estimates, so a training sequence is transmitted in the first OFDM block.

### Channel Estimation Algorithm

A low-complexity channel estimation algorithm known as *Sparse Channel Estimation* [16] is used in the time domain. Sparsing of the channel impulse response leads to an improved performance, reducing the error variance. In this case, instead of implementing the complete algorithm, which includes the selection of the number of samples  $L \leq K$  of the impulse response of the channel, the full-sized impulse response is used by choosing  $L = K$ .

The channel estimates to be used in the next block must be calculated after the assessment of the detected symbols using the coherent detector algorithm. To do so, the channel estimation technique performs the following steps (experimental underwater channel examples are shown in the referenced figures):

1. Calculation of the first frequency-domain channel estimates from the received values  $\mathbf{y}_k(n)$ , the phase offsets  $\hat{\theta}_k(n)$  and the set of data decisions and pilots  $\tilde{d}_k(n)$  (see Fig. 6.13).

$$\mathbf{X}_k(n) = \mathbf{y}_k(n)e^{-j\hat{\theta}_k(n)}\tilde{d}_k^*(n), \quad k = 0, \dots, K-1 \quad (6.15)$$

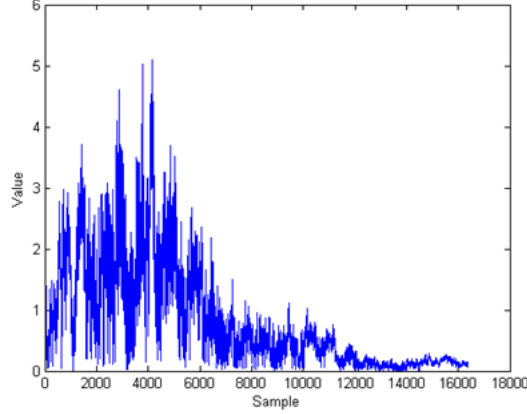


Figure 6.13: Channel frequency-domain estimates  $\mathbf{X}_k$  for an OFDM signal with  $K=16384$ ,  $B=115$  kHz, and 8-PSK subcarrier modulation

2. Application of the IFFT algorithm to get the first time-domain channel estimates  $\mathbf{x}_l(n)$  from  $\mathbf{X}_k(n)$  (see Fig. 6.14).

$$\mathbf{x}_l(n) = \frac{1}{K} \sum_{k=0}^{K-1} \mathbf{X}_k(n) e^{+j2\pi kl/K}, \quad l = 0, \dots, K-1 \quad (6.16)$$

3. Application of the sparsing by simply truncating the time-domain channel coefficients (see Fig. 6.14). A threshold  $\alpha_c$  is defined so that every time-domain channel coefficient below this value is set to zero. After the truncation is performed, the new time-domain channel response  $\tilde{\mathbf{x}}_l(n)$  is taken.

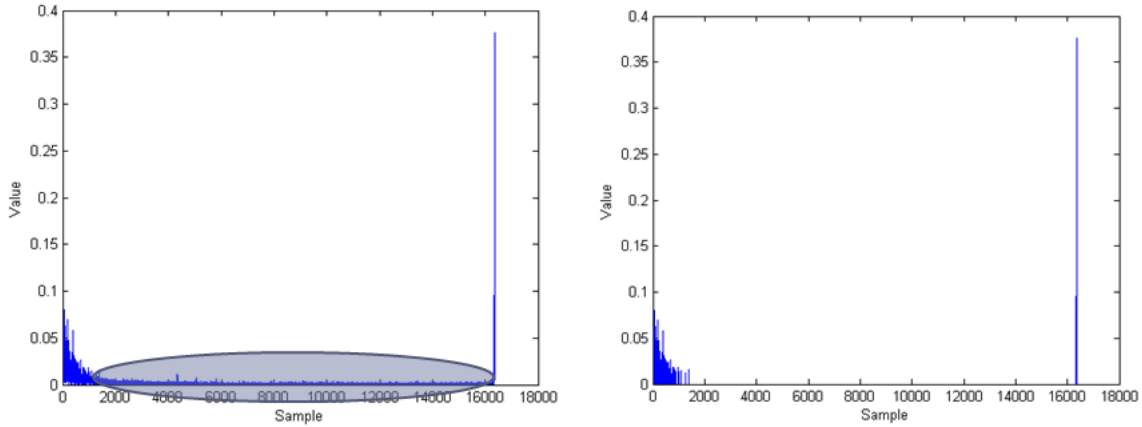


Figure 6.14: Channel time-domain estimates  $\mathbf{x}_l$  (left) and truncated coefficients  $\tilde{\mathbf{x}}_l$  (right) for an OFDM signal with  $K=16384$ ,  $B=115$  kHz, and 8-PSK subcarrier modulation

4. Adaptive channel estimation to calculate the time-domain channel estimates applying the following algorithm (see Fig. 6.15):

$$\hat{\mathbf{h}}_l(n+1) = \lambda \hat{\mathbf{h}}_l(n) + (1 - \lambda) \tilde{\mathbf{x}}_l(n) \quad (6.17)$$

5. Application of the FFT algorithm to get the final frequency-domain channel estimates used in the next block (see Fig. 6.15):

$$\hat{\mathbf{H}}_k(n) = \sum_{l=0}^{K-1} \hat{\mathbf{h}}_l(n) e^{-j2\pi kl/K}, \quad k = 0, \dots, K-1 \quad (6.18)$$

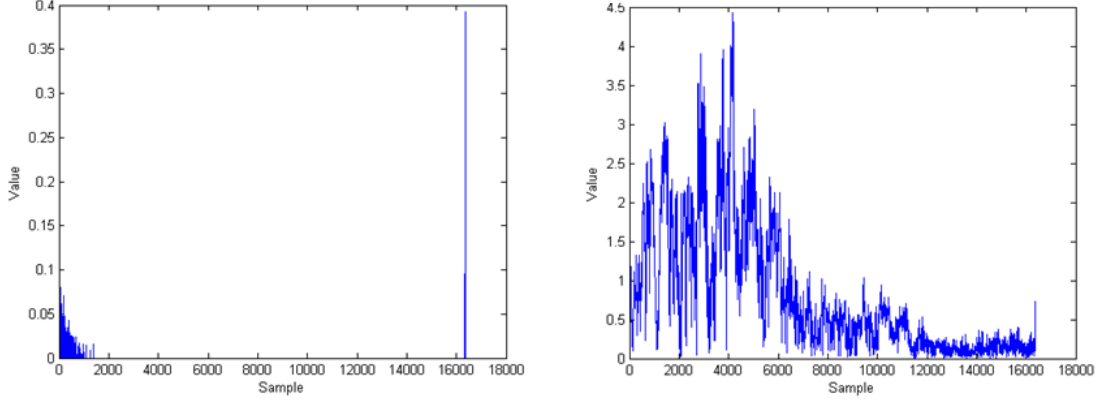


Figure 6.15: Channel updated time-domain estimates  $\hat{\mathbf{h}}_l$  (left) and final frequency-domain estimates  $\hat{\mathbf{H}}_k$  (right) for an OFDM signal with  $K=16384$ ,  $B=115$  kHz, and 8-PSK subcarrier modulation

## 6.6 Performance analysis

The performance of the system is quantified by using the concepts of (1) Mean Square Error (MSE) of the retrieved constellation points, and (2) Bit and Symbol Error Rates (BER and SER).

### 6.6.1 MSE

Regarding the MSE, it indicates the distance from the detected symbols (before a decision is made) to the transmitted complex points in the constellation (see Fig. 6.16). Two types of MSE are evaluated, one that indicates the performance depending on the frequency subcarriers (MSE-frequency), and another that indicates the performance over the transmitted OFDM blocks (MSE-time).

The MSE-time calculation is evaluated over the  $K$  subcarriers, for each OFDM block, as

$$MSE_t(n) = \frac{1}{K} \sum_{k=0}^{K-1} |d_k(n) - \hat{d}_k(n)|^2 \quad (6.19)$$

And the MSE-frequency gives the mean square error over  $N$  received OFDM blocks, as

$$MSE_f(k) = \frac{1}{N} \sum_{n=1}^N |d_k(n) - \hat{d}_k(n)|^2 \quad (6.20)$$

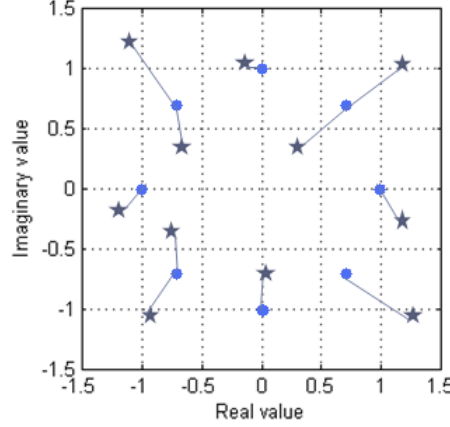


Figure 6.16: MSE concept. Detected symbols before decision,  $\hat{d}_k$  (grey stars), and transmitted symbols,  $d_k$  (blue circles)

The system performance can be then evaluated over time, while the subcarriers' performance can also be studied (normally those subcarriers that are received with more energy will have lower MSE). Sample MSE plots are shown in Fig. 6.17 and Fig. 6.18 for the underwater channel. Excellent performance is achieved when the MSE is below -5 dB, while otherwise the results can vary depending on the FEC coding.

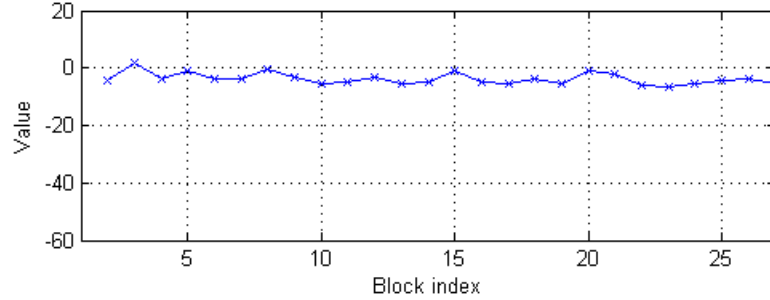


Figure 6.17: MSE-time in dB (8-PSK subcarrier modulation,  $K=16384$ ,  $\text{BCH}(63,18)$ ,  $B=115$  kHz)

### 6.6.2 Bit and Symbol Error Rates

The Bit Error Rate (BER) is calculated as the total number of wrong bits divided by the amount of transmitted bits. It is assessed for both the coded sequence (before the FEC decoding is performed) and the decoded sequence of bits. This last result gives a direct indication of whether the transmitted sequence is correctly retrieved or not.

Sample BER plots are shown in Fig. 6.19. The coded BER is higher than the decoded BER, as it may be expected.

The Symbol Error Rate (SER) is calculated as the total number of wrong symbols (before the coding-oriented decision is performed) divided by the total amount of symbols in the transmission. It is both assessed over the frequency subcarriers and the OFDM blocks, so as to give an indication of the error performance along the transmission time, as well as for the different subcarriers.

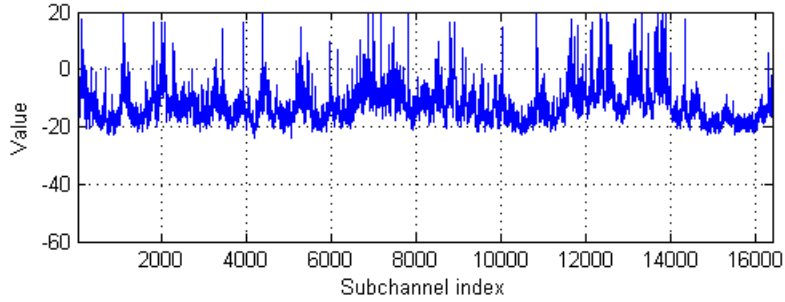


Figure 6.18: MSE-frequency in dB (8-PSK subcarrier modulation,  $K=16384$ ,  $\text{BCH}(63,18)$ ,  $B=115$  kHz)

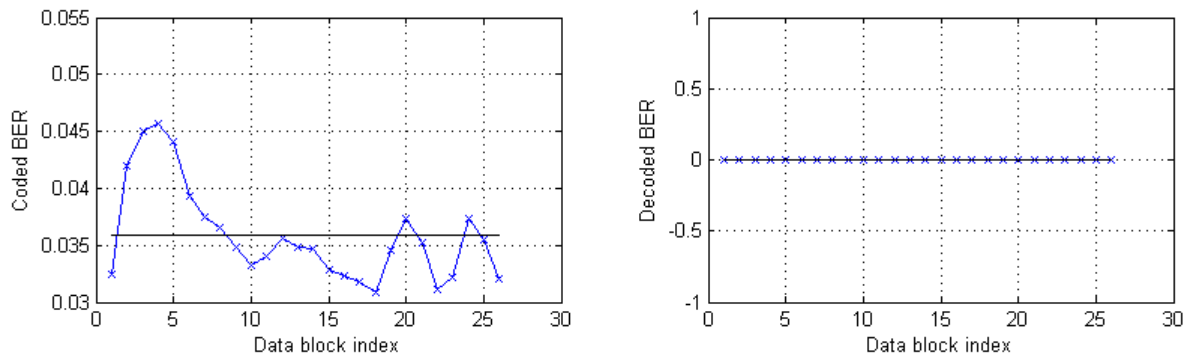


Figure 6.19: Coded sequence BER (left) and decoded sequence BER (right). The black solid line represents the mean BER. OFDM parameters: 8-PSK subcarrier modulation,  $K=16384$ ,  $\text{BCH}(63,18)$ ,  $B=115$  kHz

Sample SER plots are given in Fig. 6.20 for the same case than the previous BER ones. As it may be expected, the SER is higher than the coded BER (as there are more bits than symbols and a wrong bit directly implies that a wrong symbol decision was made). Very bad performance is observed in those subcarriers that are highly attenuated by the multipath channel.

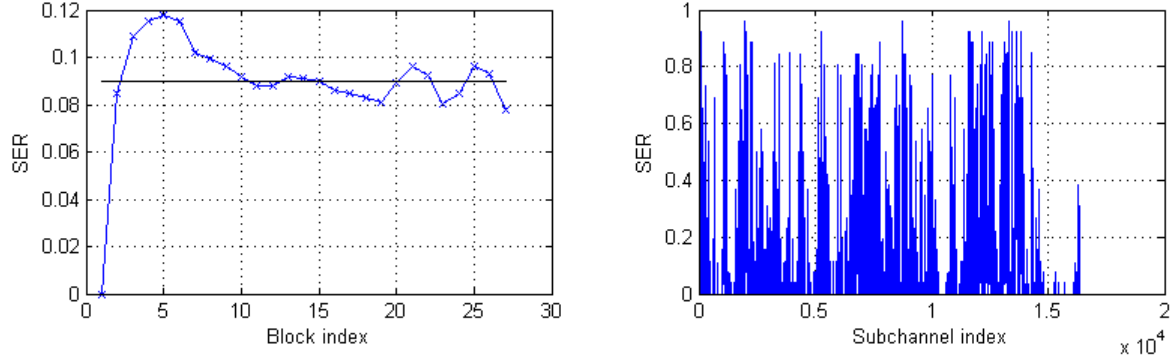


Figure 6.20: SER-time (left) and SER-frequency (right). The black solid line represents the mean SER. OFDM parameters: 8-PSK subcarrier modulation,  $K=16384$ ,  $BCH(63,18)$ ,  $B=115$  kHz



# Chapter 7

## System deployment

Once the modulation and demodulation algorithms have been implemented, they must be coupled with the source coding technique (in this case the MPEG-4 encoder/decoder) and the transmitting and receiving side hardware components. The overview of the complete implemented system is shown in Fig. 7.1.

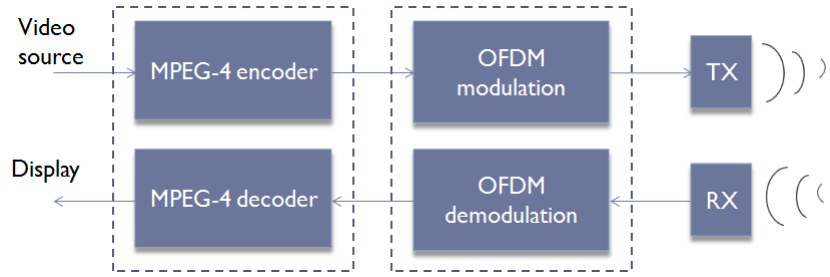


Figure 7.1: System model

In this chapter, some explanations are provided regarding the transmitting and receiving side hardware, and the practical deployment for both in-air tests and underwater experiments. In addition, the OFDM signal parameters that have been used for the sets of experiments are discussed.

### 7.1 Air tests

The first experiments are performed in an in-air acoustic testbed. The purpose of the in-air tests is to prove the correct performance of the system under a variety of situations, such as static conditions between transmitter and receiver or motion between them, among others. The main advantage of these tests is that the channel conditions can be controlled, as the transmitter and receiver can be positioned manually and the channel between them can be directly checked.

#### 7.1.1 Deployment

The deployment used for the in-air tests is shown in Fig. 7.2 for the transmitting side, and Fig. 7.3 for the receiving side.



Figure 7.2: Air tests transmission block diagram

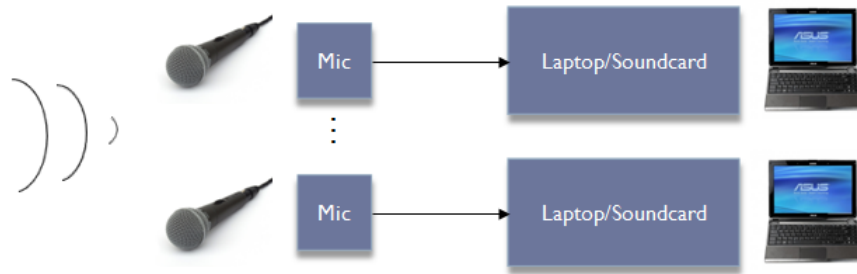


Figure 7.3: Air tests reception block diagram

The wavefiles that contain the OFDM signals are generated using the developed MATLAB application (user's manual provided in Annex A) at the transmitting side laptop, and then the GNU Radio interface (a set of tools for the creation of Software Defined Radios, SDR, which uses the Universal Software Radio Peripheral, USRP, as an interface with the transmitting and receiving hardware) is used to send the signal to the laptop speaker.

On the receiving side, the signal is acquired by a number of microphones (one in the case of only one receiving element, or more if spatial diversity is used), and the laptop soundcard acts as an interface with the MATLAB application, which records the signal and demodulates it.

### 7.1.2 Hardware

The hardware components that have been used for the implementation are described in this section. They are:

- Laptop/GNURadio: The transmitting side laptop is used to generate the wavefiles with MATLAB and then, once the signals are stored, the GNU Radio platform is used to send the wavefiles to the USRP board. This last step involves the use of a Python script to transmit the files to the USRP and from it to the transmitting hardware, which in this case is a laptop speaker.
- USRP LFTX: The Universal Software Radio Peripheral (USRP) board is used as an interface that allows the transmission of the generated acoustic signals by using a high sampling rate (in this project 1 Mbps is used) of the analog wavefile provided by the laptop computer. More information about the USRP board can be found in [24].
- Speaker: The speaker that is used for the tests is a normal laptop speaker connected to the USRP transmitter connector.

- Microphones: Commercial microphones are used to receive the OFDM signal from the air.
- Laptop/Soundcard: The receiving laptops' soundcards are used to retrieve the signals from the microphones. Specifically, MATLAB is used to record the signals, and proceed to the posterior demodulation (once all the signals are transferred to one of the laptops, if spatial diversity is applied).

### 7.1.3 OFDM parameters

The OFDM signal useful bandwidth is mainly limited in this setup by the laptop soundcard sampling rate, which is the typical 44.1 kHz used for sound applications. The transmission bandwidth is 11.025 kHz, from 1 kHz to 12.025 kHz, avoiding then a narrow low frequency band from 0 to 1 kHz due to high noise components, and meeting the oversampling requirements (a factor of between 3 and 4 is suggested).

The OFDM parameters that have been used for the in-air tests are summarized in Tab. 7.1. The achieved data rates are also specified in Tab 7.2.

# subcarriers	FFT size	carrier spacing	OFDM symbol duration	bandwidth efficiency
$K$	$N_s = 4K$	$\Delta f = B/K$ [Hz]	$T = 1/\Delta f$ [ms]	$R/B = T/(T + T_g)$ [sps/Hz]
1024	4096	10.77	92.9	0.90

Table 7.1: OFDM signal parameters used for the experiment ( $B = 11.025\text{kHz}$ ,  $T_g = 10\text{ms}$ )

Modulation	BCH code								
	7/4	15/11	31/21	63/51	63/30	63/18	63/10	127/120	255/239
QPSK	9.95	13.69	13.06	15.86	9.33	5.60	3.11	18.66	18.59

Table 7.2: Data bit rates with 1024 subcarriers (in  $\text{kbps}$ )

## 7.2 Underwater tests

Once the algorithms are tested and the in-air experiments provide successful results, the system is tested in the underwater channel. The video files are transmitted using different configurations and parameters, and the performance of the detection algorithms is tested for several distance ranges. Moreover, the limits in terms of data rate and useful bandwidth are reached to achieve an optimal performance with the selected hardware.

### 7.2.1 Deployment

The illustrative block diagram for the underwater tests is shown in Fig. 7.4 for the transmitting side, and Fig. 7.5 shows the receiving side block diagram.

A deployment picture is shown in Fig. 7.6, where the transducer and hydrophone structures are illustrated. A weight cylinder is used to stabilize the transducer and avoid the drift caused by the waves, while a similar structure with a cinder block and a floating buoy is used to deal with vibrations on the receiving side, caused by the combined action of the waves and the boat movement.

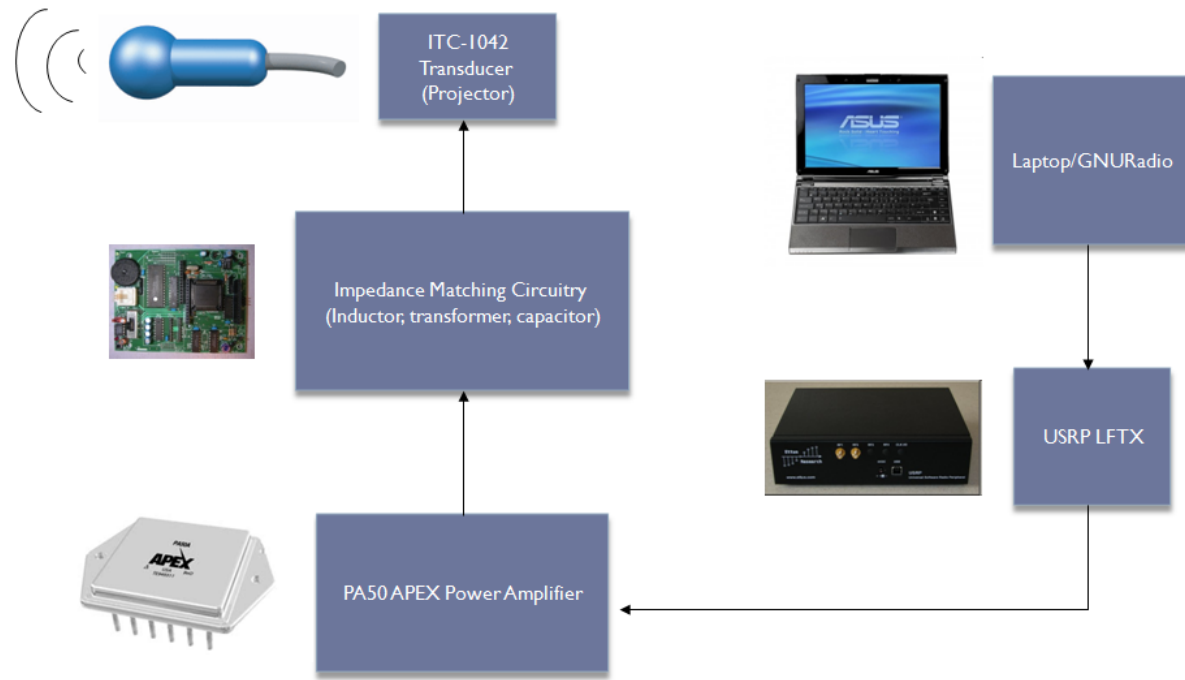


Figure 7.4: Underwater tests transmission block diagram

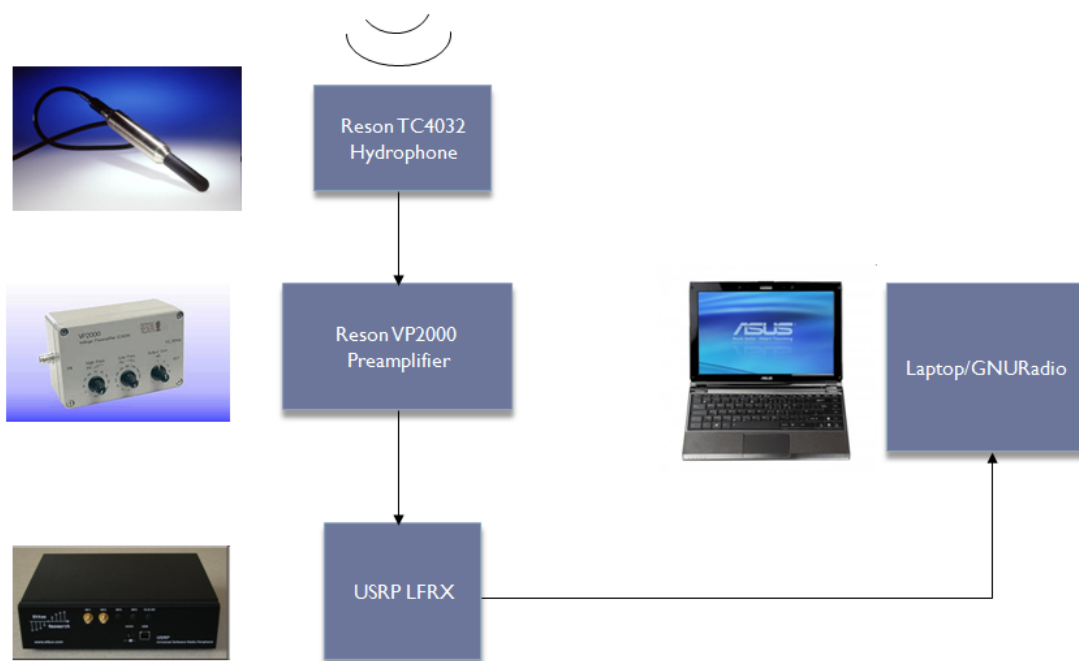


Figure 7.5: Underwater tests reception block diagram

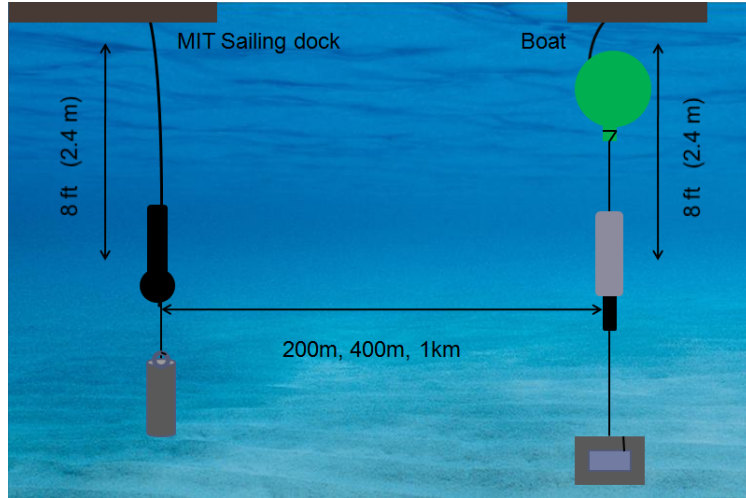


Figure 7.6: Underwater tests deployment

### 7.2.2 Hardware

The hardware components that have been used for the underwater implementation are:

- Laptop/GNURadio: Exactly as in the in-air tests, the transmitting side laptop is used to generate the wavefiles with MATLAB (the application manual is provided in Annex A) and then, once the signals are stored, the GNU Radio platform is used to send the wavefiles to the USRP board. A Python script is used to transmit the files to the USRP and from it to the transmitting hardware, which in this case is the PA50 APEX power amplifier coupled with the transducer by an impedance matching circuit. On the receiving side, the laptop receives the wavefile from the USRP via another GNU Radio Python script, and the demodulation is performed.
- USRP LFTX: As in the in-air case, the USRP board is used as an interface that allows the transmission of the generated acoustic signals by sampling at 1 Mbps the analog wavefile provided by the laptop computer. More information about the USRP board can be found in [24].
- PA50 APEX power amplifier: The signal transmitted by the USRP board is further amplified by the PA50 APEX power amplifier, to adjust the signal power to the transmission requirements in the underwater channel. The power response of the PA50 APEX power amplifier is shown in 7.7. For frequencies lower than 200 kHz, the output voltage is maximized.
- Impedance matching circuitry: Prior to sending the signal to the transducer, an impedance matching circuit adjusts the signal for maximum power transmission to the transducer. It involves the use of capacitors, inductors and transformers.
- ITC-1042 transducer: The selected transducer is an omnidirectional ITC-1042, which is a broadband piezoelectric device whose main advantage is the high output power compared to other commercially available models. Its directivity pattern and Transmitting Voltage Response (TVR) are shown in Fig. 7.8. As it can be observed in the TVR plot, the response has a resonance frequency, and it decays at lower and higher frequencies, thus limiting the transmission bandwidth (mainly at the high frequency end, which is not observed in the plot).
- Reson TC4032 hydrophone: The Reson TC4032 ultra-wideband omnidirectional hydrophone has been chosen for the reception of the acoustic OFDM signal. Its most important characteristic is the high

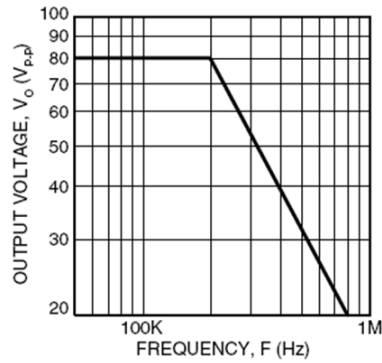


Figure 7.7: Power response of the PA50 APEX power amplifier

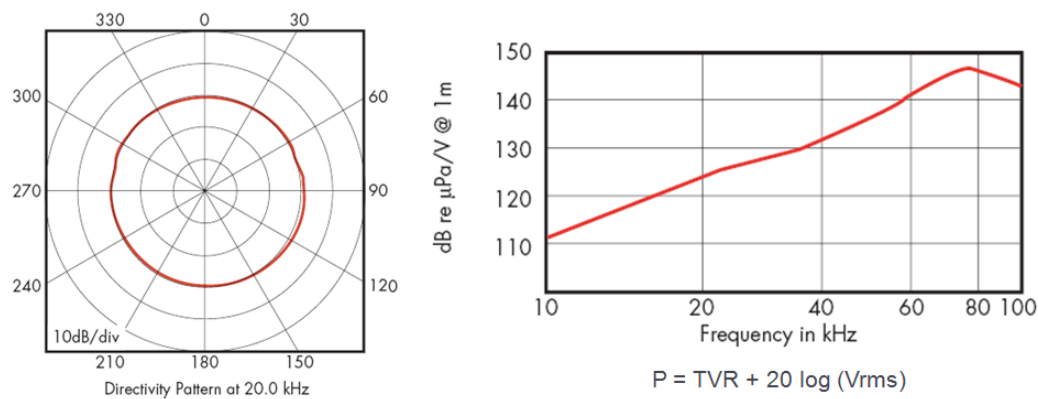


Figure 7.8: Directivity pattern (left) and Transmitting Voltage Response (TVR) (right) of the ITC-1042 transducer

sensitivity at a wide range of frequencies (it can typically operate in the 10-150 kHz range), which makes it appropriate for the transmission of low-power signals or its use in high attenuated channels. The horizontal directivity pattern and receiving sensitivity is provided in Fig. 7.9.

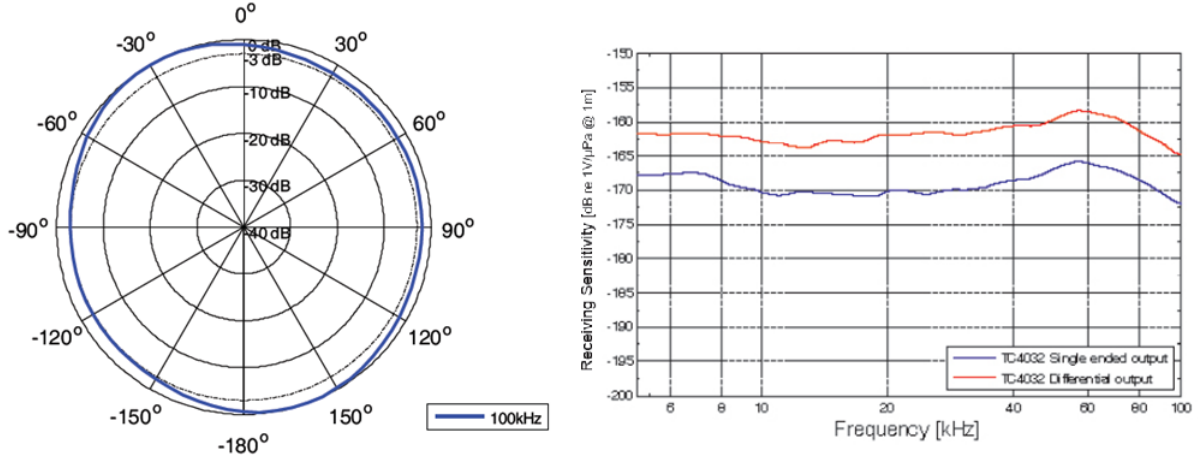


Figure 7.9: Horizontal directivity pattern (left) and receiving sensitivity (right) of the Reson TC4032 hydrophone

- Reson VP2000 preamplifier: Once the signal is picked by the hydrophone, the Reson VP2000 preamplifier receives it, and filtering is performed. The characteristics of the high-pass and low-pass filters are given in Fig. 7.10. As it can be seen, the filter response is adjustable depending on the signal frequency components.

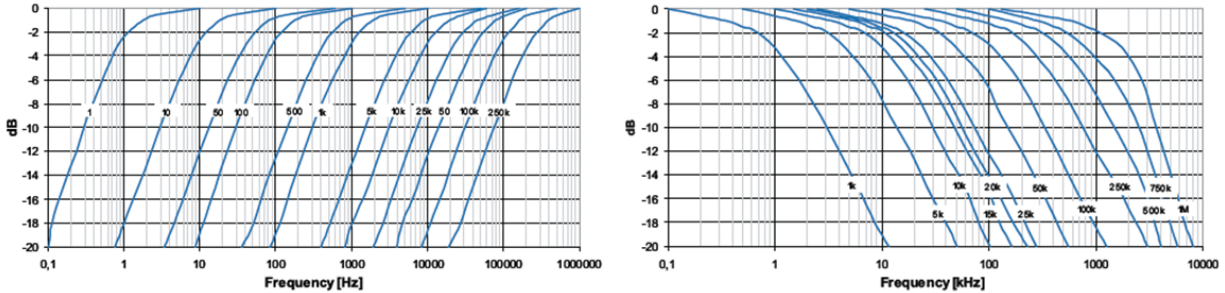


Figure 7.10: High-pass filter (left) and low-pass filter (right) frequency responses of the Reson VP2000 preamplifier

- USRP LFRX: In the underwater setup, the USRP board is also used on the reception side. Again, it acts as an interface that allows the reception of the acoustic signal by sampling at 1 Mbps the analog wavefile provided by the Reson VP2000 preamplifier, and transmitting it to the receiving side laptop computer.

### 7.2.3 OFDM parameters

The underwater experiments fully utilize the USRP high sampling rate capabilities, both on the transmission side and the reception side. As a result of that, the frequency allocation is not limited by the maximum

sampling rate, which in this implementation is as high as 1 Mbps. Thus, the signal is allocated from 40 kHz to 155 kHz (with a useful bandwidth of 115 kHz), taking into account both the low frequency noise characteristics, and high attenuation at high frequencies, along with the transducer-hydrophone pair frequency responses (as it was commented in Sec. 5.2.8).

Regarding the number of subcarriers,  $K=16384$  is the ideal case for the undertaken transmissions, as a higher data rate is achieved. In spite of that, the case  $K=8192$  has also been used in several situations due to:

1. The separation between subcarriers,  $\Delta f$ , is larger, and, as a consequence, the frequency synchronization is not as critical (the Inter-Carrier Interference, ICI, is not as pronounced).
2. The symbol time is smaller, and hence the assumption that the channel estimates and the phase estimates do not differ much from one block to the next is more accurate.

The OFDM parameters that have been used for the underwater tests are summarized in Tab. 7.3. The achieved data rates are also specified in Tab 7.4. The two different values for the number of subcarriers are taken into consideration, and the modulation types that provide a best performance are also specified.

# subcarriers	FFT size	carrier spacing	OFDM symbol duration	bandwidth efficiency
$K$	$N_s = 5K$	$\Delta f = B/K$ [Hz]	$T = 1/\Delta f$ [ms]	$R/B = T/(T + T_g)$ [sps/Hz]
8192	40960	14.04	71.2	0.88
16384	81920	7.02	142.5	0.93

Table 7.3: OFDM signal parameters used for the experiment ( $B = 115\text{kHz}$ ,  $Tg = 10\text{ms}$ )

$K$	Modulation	BCH code								
		7/4	15/11	31/21	63/51	63/30	63/18	63/10	127/120	255/239
8192	QPSK	100.84	138.66	132.36	160.72	94.54	56.73	31.51	189.08	188.29
	8-PSK	151.27	207.99	198.54	241.08	141.81	85.09	47.27	283.62	282.44
	16-QAM	201.69	277.32	264.71	321.44	189.08	113.45	63.03	378.16	376.59
16384	QPSK	107.46	147.75	141.04	171.26	100.74	60.45	33.58	201.48	200.64
	8-PSK	161.19	221.63	211.56	256.89	151.11	90.67	50.37	302.22	300.97
	16-QAM	214.92	295.51	282.08	342.52	201.48	120.89	67.16	402.97	401.29

Table 7.4: Data bit rates with 8192 and 16384 subcarriers (in  $\text{kbps}$ )

# Chapter 8

## Experimental results

After the system is implemented and all the hardware components are selected, the experimental part of the work begins. Three types of experiments are designed to prove the correctness of the selected algorithms and test the system performance under a variety of situations.

First, some simulations are designed to provide the first results and check the system performance. After that, some in-air testing is done to further check the overall implementation with a simple channel. Finally, underwater tests are performed and a thorough analysis is provided.

The different types of tests are explained in this chapter, and multiple results support the performance explanations.

### 8.1 Simulation tests

The first experiments are performed in a simulated channel, so that the wavefiles are generated with the *WAV Generator* application (see Annex A) and the wavefile input to the detector is created with the channel simulator application (see Sec. A.1.4). The objectives of the tests are: (1) checking the performance results with different subcarrier modulations (both the signal generation and detection), and (2) checking the system performance for different simulated distances.

#### 8.1.1 Description

The channel simulator includes 3 steps: the simulation of the multipath channel, the simulation of the distance attenuation in an underwater channel, and the underwater noise addition. The block diagram is shown in Fig. 8.1.

As it can be seen in the simulator block diagram, the multipath channel (block 1) is simulated by adding the generated OFDM signal, shifted in time and scaled by a given reflection coefficient, to itself. In the undertaken simulations, 3 arrivals have been considered (at 0 msec (direct path), 1 msec, and 2 msec), with different reflection coefficients (1, 0.6 and 0.3, respectively).

The signal attenuation is then applied to the resulting wavefile (block 2 in the block diagram). The  $A(l, f_c)$  coefficient, where  $l$  is the transmission distance and  $f_c$  is the center frequency of the useful bandwidth, is

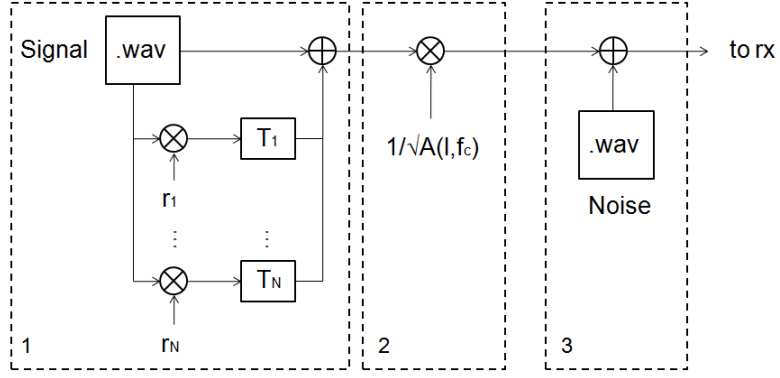


Figure 8.1: Simulator. Block diagram

calculated using the equation 2.1. The frequency-dependent attenuation through the useful bandwidth has been simplified, and a coefficient is calculated for all the subcarriers.

Finally, a real underwater noise file is added (block 3 in the block diagram) to simulate the background noise in the underwater channel. The noise file is a sample from previous underwater noise-recording experiments done in the Gulf of Mexico during the first months of 2009.

It must be taken into account the fact that no time variation is considered in the simulator implementation. One of the most important characteristics (and more difficult to detect than other ones) of the underwater channel, and any communication channels indeed, is its variation through time. As a result, the achieved performance for the simulated transmissions is much better than the one for the real underwater channel.

With reference to the OFDM parameters, the  $K=16384$  subcarriers case from the underwater testing configuration has been taken into account (see Sec. 7.2.3).

### 8.1.2 Subcarrier modulations

Five types of constellations have been tested with the channel simulator (QPSK, 8-PSK, 16-QAM, 32-QAM and 64-QAM). The selected distance is 400 m, and the detected constellations are plotted in Fig. 8.2 and Fig. 8.3.

Furthermore, a Mean Square Error (MSE) and bit error rate (BER) study has been done for the different transmissions, with the aim to quantize the detection performance for the different subcarrier modulation types. The results are shown in Fig. 8.4 and Fig. 8.5.

### 8.1.3 Distances

The next set of simulated transmissions regards the detection performance for a transmitted 8-PSK constellation at different distances between transmitter and receiver. The selected distances have been 200 m, 400 m, and 600 m. The constellation plots are shown in Fig. 8.6, while the MSE and BER are shown in Fig. 8.7 and Fig. 8.8. For the BER plot, only the non-zero curves are shown.

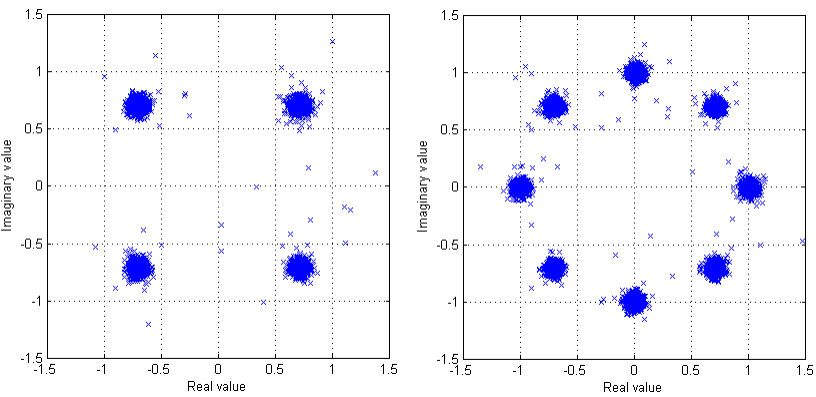


Figure 8.2: Simulated PSK constellations at 400 m. QPSK (left), and 8-PSK (right)

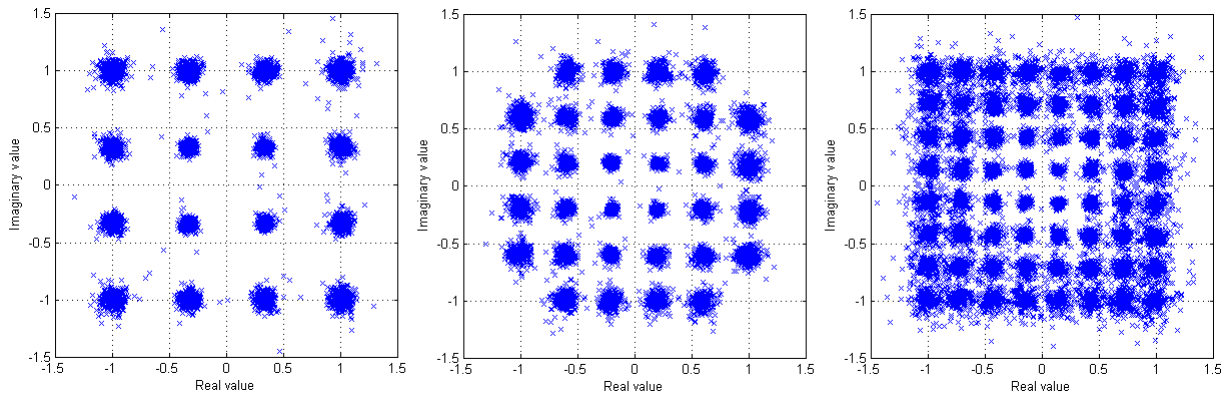


Figure 8.3: Simulated QAM constellations at 400 m. 16-QAM (left), 32-QAM (center), and 64-QAM (right)

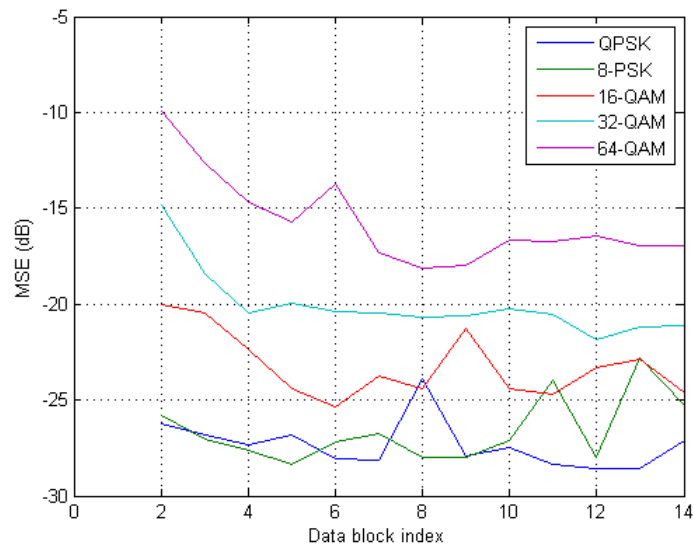


Figure 8.4: MSE-time for different modulation types at 400 m

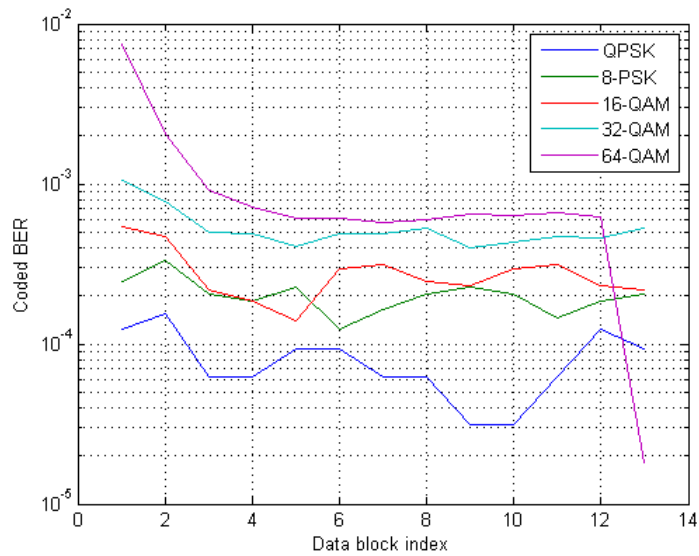


Figure 8.5: Coded sequence time BER for different modulation types at 400 m

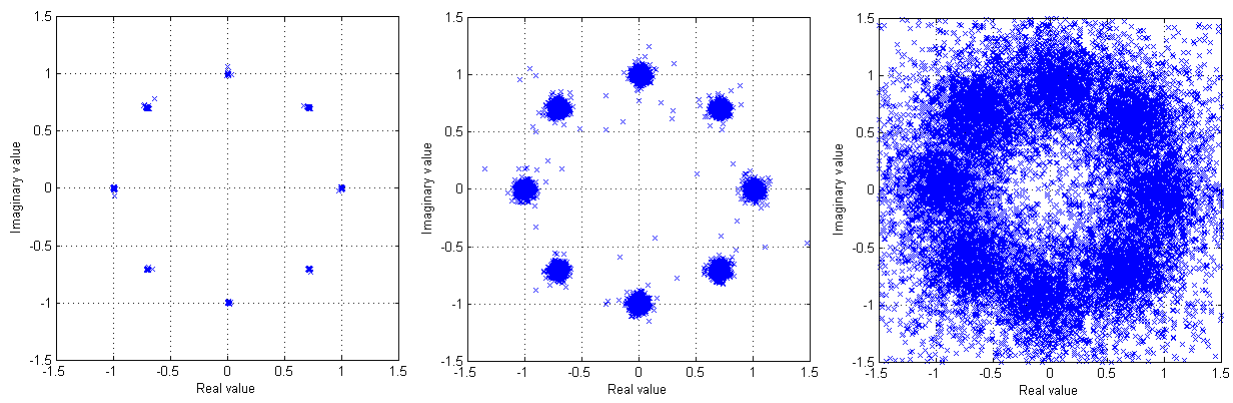


Figure 8.6: 8-PSK constellations for 200 m (left), 400 m (center), and 600 m (right)

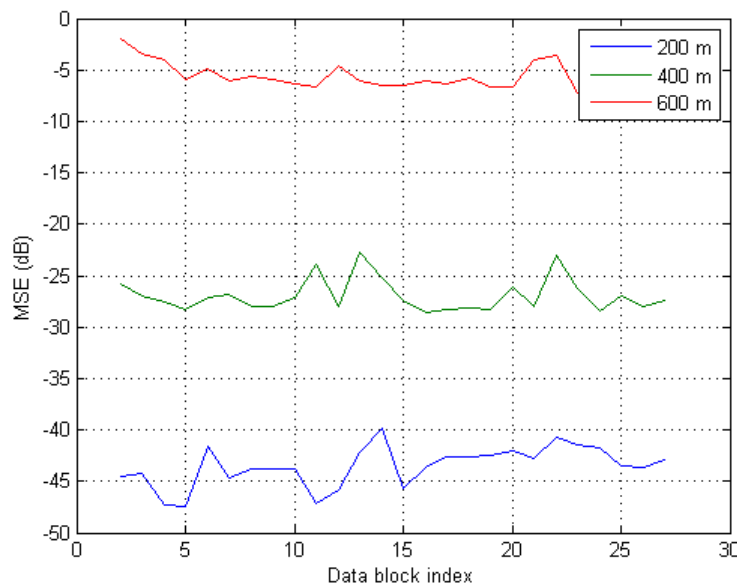


Figure 8.7: MSE-time for different distances

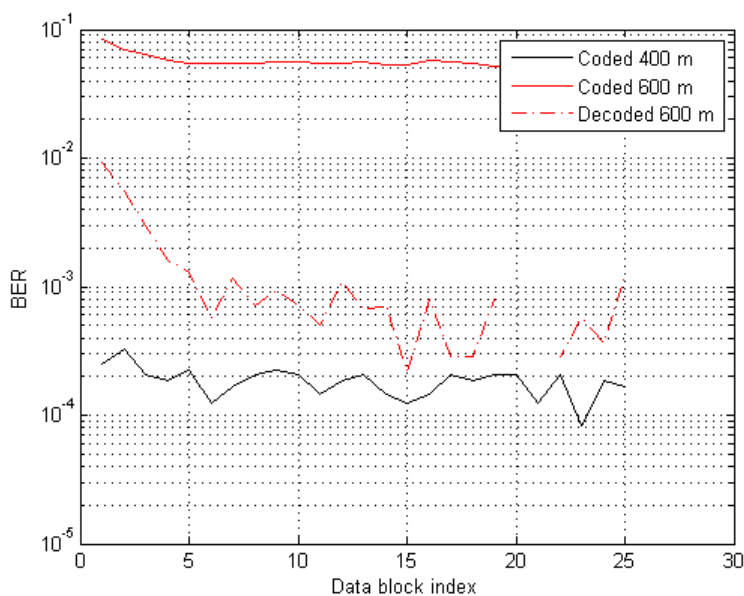


Figure 8.8: Time BER for different distances

## 8.2 Air tests

There is basically one reason why the in-air tests have been considered, which is the fact that the channel between transmitter and receiver is entirely known. Indeed, the indoor testbed provides an easy way of checking the detection performance under several channel conditions, which can be recreated by moving the transmitter (speaker) and/or receiver (microphone).

Specifically, there have been 3 approaches for the in-air tests: a multipath analysis, a motion effects study, and a performance check for multiple receivers.

### 8.2.1 Multipath

The first thing that has been studied is the correspondence between the real channel and the time domain channel estimates that are observed with the coherent detector. The channel estimates and the speaker-microphone layout are shown in Fig. 8.9.

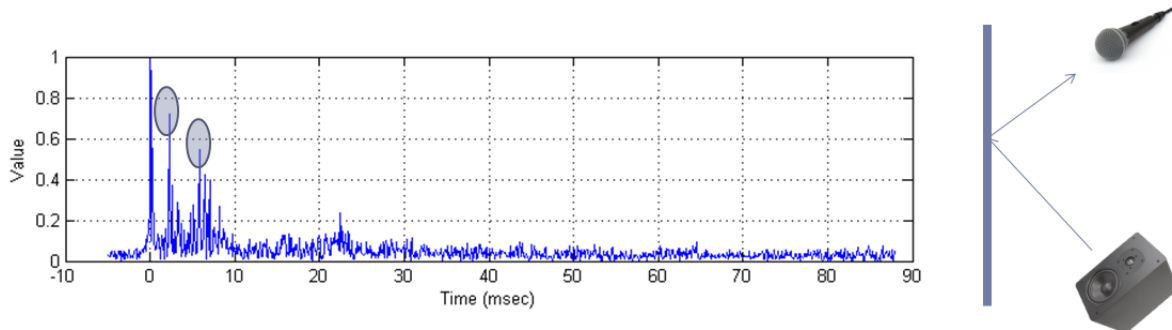


Figure 8.9: Chanel time-domain estimates (left) and experiment layout (right)

The real channel possible reflections are the ceiling and wall reflections of the laboratory. After some calculations, the correspondence is established between these reflections and the multipath arrivals seen in the channel estimates. The details are shown in Tab. 8.1.

Arrival time (msec)	Path distance (m)	Correspondence
2.18	0.74	Wall reflection
5.71	1.94	Ceiling reflection

Table 8.1: Multipath study

The following must be noted regarding the multipath absorption: as the speed of sound underwater is approximately five times the speed of sound in air, the multipath that is absorbed in a given time period for the underwater channel is for a five times longer path than the absorbed multipath in air. As a result, the conditions of the system underwater are much better, in terms of guard time design (a five times shorter guard time will be needed to absorb the same reflected paths).

### 8.2.2 Motion

The second set of tests aim at checking the motion track for different types of relative speed and acceleration between transmitter and receiver. Two sets of experiments have been designed, one with moderated motion and another with fast motion, and different behaviors have been found for the different detector types.

#### Moderated motion

The moderated motion case involves the movement of the receiver (microphone) with uniform speed towards the transmitter (speaker), followed by a gradual decrease of velocity until a stop, and then another movement with uniform speed in the opposite direction, moving away from the speaker. The experiment layout and the phase estimates are shown in Fig. 8.10.

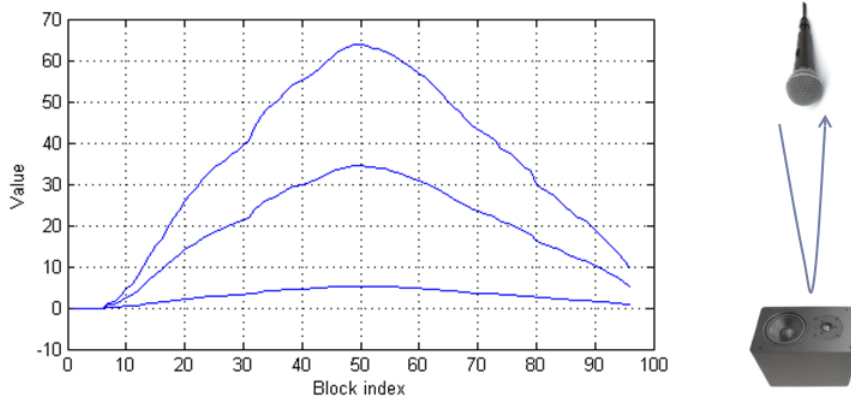


Figure 8.10: Phase estimates in radians for  $k=0$ ,  $k=511$  and  $k=1023$  (left) and experiment layout (right), with moderated motion and coherent detection

In the phase estimates plot, the increase in the phase estimates value corresponds to the approach of the microphone towards the speaker, while the decrease in the phase estimates value corresponds to the subsequent separation between them. The relative speed between transmitter and receiver is approximately 10 cm/s (1 meter movement for a 10-second transmission), and the phase tracking algorithm is, in this case, perfectly acquiring the motion-induced Doppler effect.

Finally, the BER results for both the coded and decoded sequence are shown in Fig. 8.11. As it may be expected, in the figure some increases are seen in the parts where the acceleration, or phase gradient, is high. The decoded BER is lower than the coded one, as the decoder can correct an important number of random errors.

#### Fast motion

The fast motion case involves a first static period of time, followed by a quick left-right motion of the microphone (which involves both high speed and acceleration), and another static period at the end. The phase estimates and experiment layout in this case is shown in Fig. 8.12. The detection results with the coherent detector are shown in Fig. 8.13.

As it can be seen, the decoded sequence BER for the coherent detector is null for the static period, and

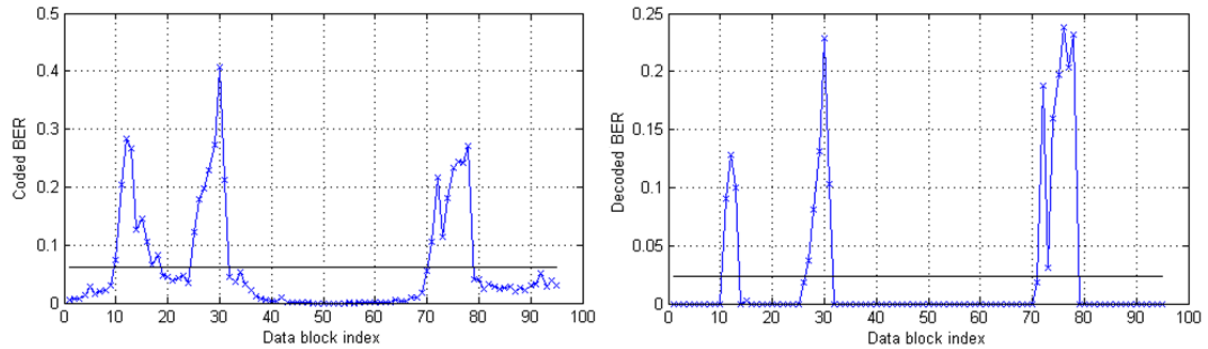


Figure 8.11: Coded sequence time BER (left) and decoded sequence time BER (right), with moderated motion and coherent detection

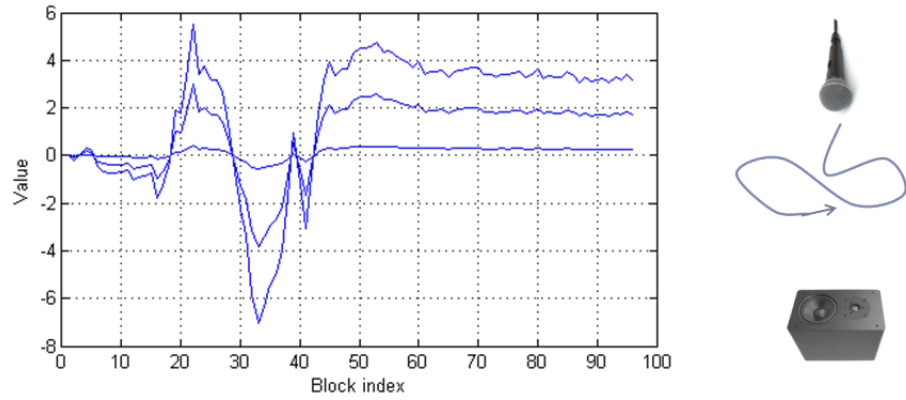


Figure 8.12: Phase estimates in radians for  $k=0$ ,  $k=511$  and  $k=1023$  (left) and experiment layout (right), with fast motion and coherent detection

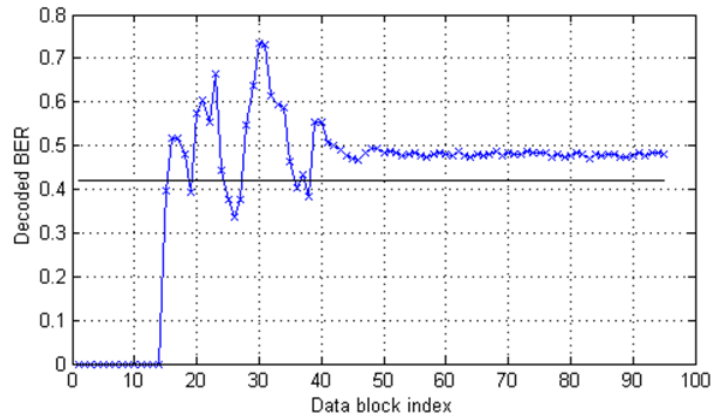


Figure 8.13: Decoded sequence time BER, with fast motion and coherent detection

then it increases to 0.5, where it remains until the end of the transmission. In this case the selected detector loses track of the channel estimates, as the motion is too high for the slow block-to-block change assumption.

An interesting change in performance is seen when the fast motion is followed by a static period with the microphone exactly put in the same location than in the beginning of the experiment. For this case, the detector can still track the channel after the motion finishes, as the adaptive algorithm has a memory of the previous channel state.

To solve the tracking problem for fast varying channels (in the first case, in which the location is changed), the differentially coherent detector is used. For the same kind of motion, the detection results with differential detection are shown in Fig. 8.14.

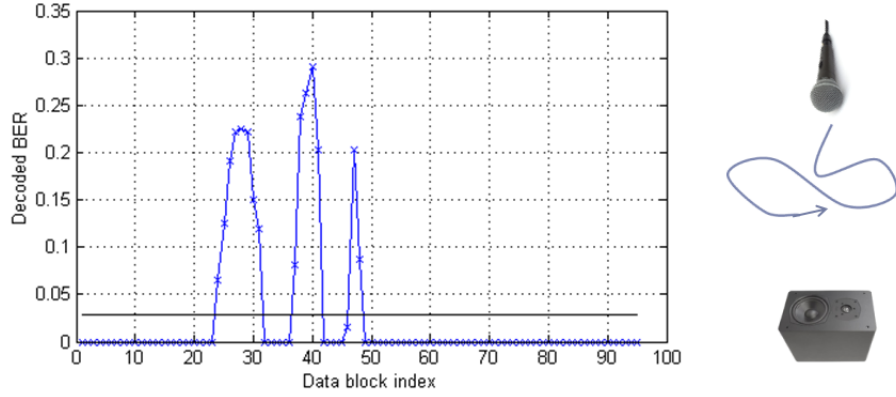


Figure 8.14: Decoded sequence time BER (left), and experiment layout (right), with fast motion and differential detection

As it may be expected, some BER peaks are seen when the highest acceleration is applied to the microphone, but after these the detector can easily get on track again, as it does not rely on the estimates for past blocks. The differential detector is then appropriate for fast motion conditions, while in static or moderated motion environments the coherent detection achieves better results.

A final comment must be made regarding the motion correspondence between the in-air transmissions and underwater environments. As it has been pointed out before, the speed of sound underwater is approximately five times the speed of sound in air, so that the relative speed that can be tolerated in an underwater implementation is five times the applied motion in-air. That is, along with the multipath absorption, another advantage of the underwater channel.

### 8.2.3 Multiple receivers

The last set of in-air experiments aim to demonstrate the performance improvement with the use of multiple receiving elements. In the practical implementation, another microphone is used to receive the same OFDM signal, and an MMSE combining of the signal is performed in the detector.

Two sets of results are evaluated. The first is for static conditions (Fig. 8.15), where an improvement of around 50% in the coded BER is observed. The second set of results (Fig. 8.16) corresponds to the fast motion case, and a BER reduction for the multiple receiving elements case is also observed even with extreme detection conditions (the high BER peaks are due to the high acceleration). The MSE curves are also lower when spatial diversity is used, representing a more accurate retrieval of the constellation.

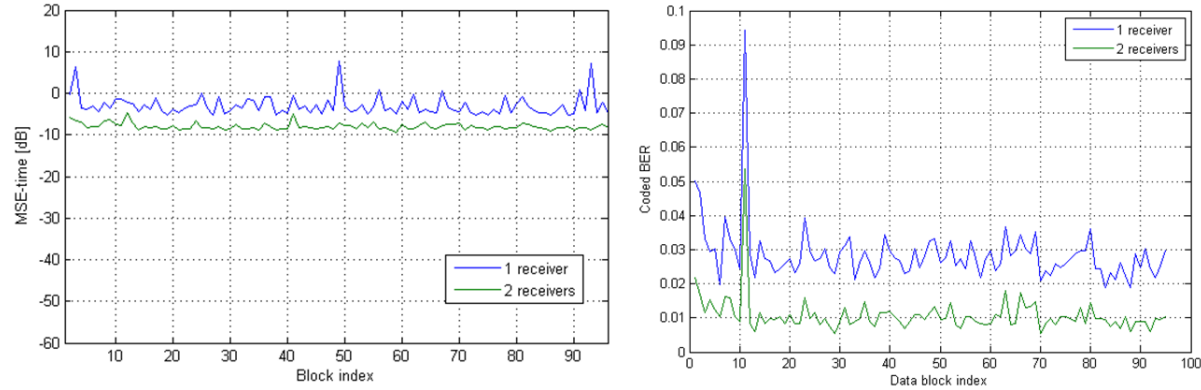


Figure 8.15: MSE-time in dB (left) and coded sequence time BER (right) with static conditions

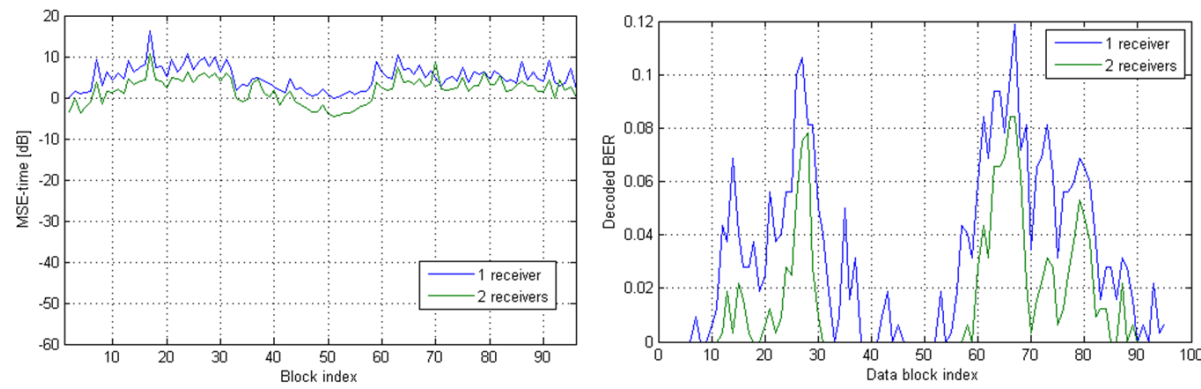


Figure 8.16: MSE-time in dB (left) and decoded sequence time BER (right) with fast motion conditions

## 8.3 Underwater tests

The underwater experiments have been conducted at the MIT Sailing Pavilion, and four main types of testing are designed, depending on the parameter of study. They are: FEC coding tests, subcarrier modulations analysis, distance experiments, and consistency tests. Before the detection performance is evaluated, some video detection considerations are discussed.

### 8.3.1 Video detection

Prior to the practical performance quantification, a targeted overall BER must be established in order to have a reference for the selection of the different parameters. That is why numerous video sequences are evaluated with different detected BER, from the first sets of preparatory experiments (with different configurations and parameters). A summary of the results is shown in Fig. 8.17.



Figure 8.17: Sample image detection. BER=0% (left), BER=0.12% (center), and BER=1.17% (right)

The conclusion after the analysis is that the detected video BER must be below 0.1% in order to have a qualitatively acceptable detection. Due to that, a target BER of  $10^{-3}$  is selected.

Before proceeding to the next experiments, it must be said that in the implemented system the FEC coding does not protect differently the headers and the video data in the MPEG-4 video stream, so that a low number of errors in the frame headers can cause the corruption of an entire image. In subsequent developments, stronger FEC coding could be applied to frame headers and other important side information, while the lighter coding could be used for the video data. By doing this, higher decoded BER could be acceptable.

### 8.3.2 FEC coding

A data sequence of 16 OFDM blocks is transmitted in a 200 meters link with different BCH codings, and the performance in terms of decoded BER is assessed. The evaluated results are shown in Fig. 8.18.

As it can be observed, the only curve that is consistently located close to the horizontal axis is the one for the  $\text{BCH}(63,30)$  code. Moreover, the curves for the  $\text{BCH}(63,18)$  and  $\text{BCH}(63,10)$  codes can not be seen as the decoded BER for these cases is always zero. Therefore, a coding ratio of 2.10 (the one for the  $\text{BCH}(63,30)$ ) is the minimum for a consistent performance.

Some explanation must be made about the decoded BER increase for the rest of the cases. As the coherent detector has been used to evaluate the different coding types, there are error propagation effects

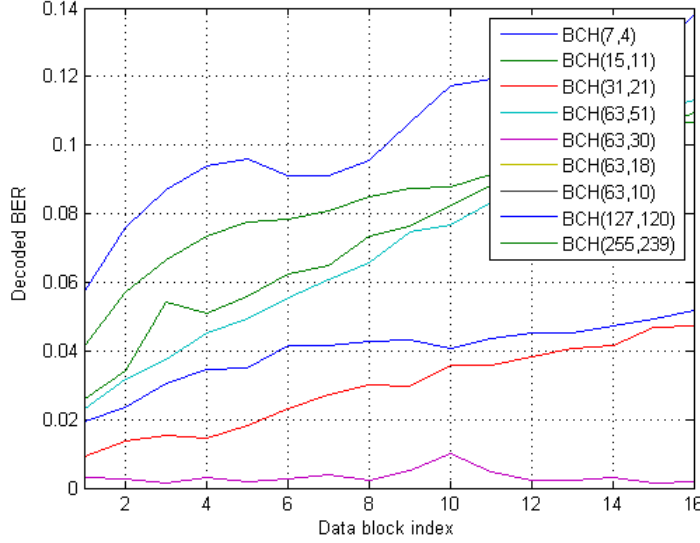


Figure 8.18: Decoded sequence time BER for different BCH codes

for those curves with too high a BER for the first data block. The consequence is that the performance degrades over time due to bad channel estimations in previous blocks, which are caused by symbol errors.

From now on, unless otherwise indicated, the FEC coding that will be used for the tests is the BCH(63,18), as it is the one that provides the targeted performance (BER less than  $10^{-3}$ ) with less needs for redundancy.

### 8.3.3 Subcarrier modulations

Once the BCH coding is evaluated and the good choices are selected, the transmitted subcarrier modulations must also be evaluated, in order to decide the type that best fits the requirements of (1) detection performance, and (2) resulting data rate. The detected PSK constellations in a 200-meter link are shown in Fig. 8.19, and the detected QAM constellations can be seen in Fig. 8.20.

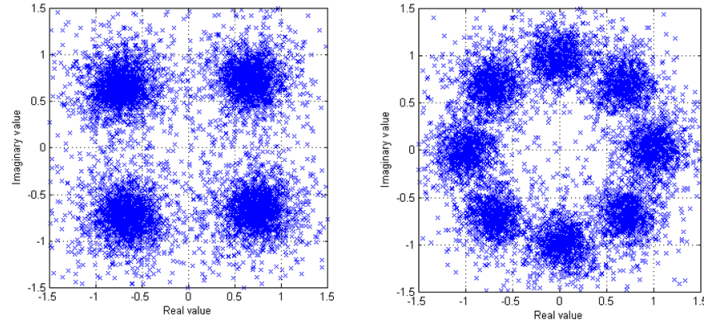


Figure 8.19: PSK constellations at 200 m with coherent detection. QPSK (left), and 8-PSK (right)

After qualitatively evaluating the detected constellations, it can be said that the PSK ones provide a better detection due to a larger spacing between the complex points, and as the density of points increase the detection worsens. For the 16-QAM constellation the density of points is still not too high and some

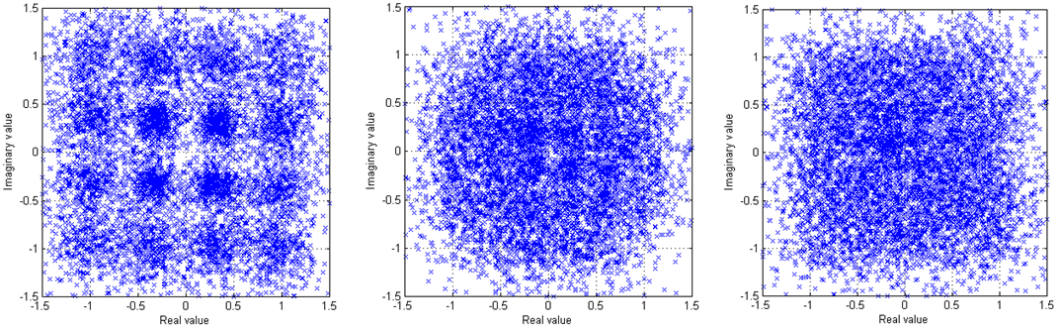


Figure 8.20: QAM constellations at 200 m with coherent detection. 16-QAM (left), 32-QAM (center), and 64-QAM (right)

degree of accuracy is observed, although the 32-QAM and 64-QAM constellation plots do not seem to provide appropriate results.

To confirm the qualitative evaluation, the MSE-time is provided in Fig. 8.21, and the BER performance is given in Fig. 8.22.

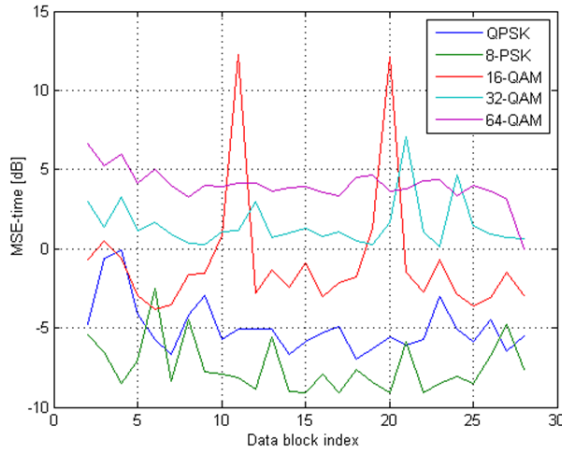


Figure 8.21: MSE-time in dB for different modulation types at 200 m

The MSE plot almost always shows higher values as higher is the density of points in the constellation, as it is expected (the wider the clouds of points in the constellation, the higher the MSE).

The BER performance is also the expected. Looking at the decoded BER, it can be checked that 32-QAM and 64-QAM definitely do not meet the requirements, while 16-QAM do not always provide the targeted performance, with BER lower than  $10^{-3}$ . The PSK constellations are the ones that must be considered for the implementation, as they always meet the decoded BER minimum value.

From now on, unless otherwise stated, the 8-PSK constellation is the one that will be used for the tests, as it provides the highest data rate, while meeting the detection requirements.

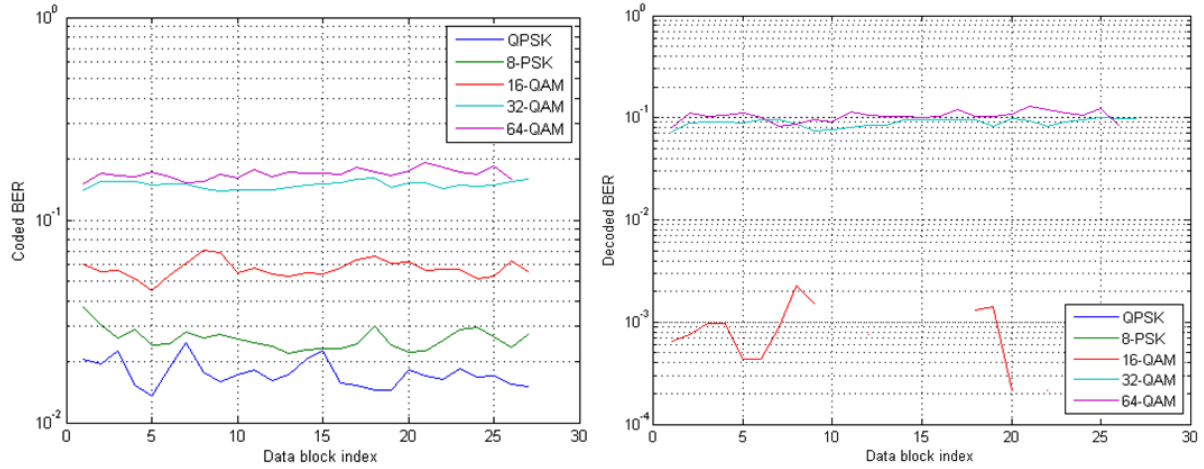


Figure 8.22: Coded sequence time BER (left) and decoded sequence time BER (right) for different modulation types at 200 m

### 8.3.4 Distances

The distance tests aim at defining the maximum distance range at which the system achieves the targeted performance. The development of these tests is possible after measuring the transmitter-receiver distance on the receiving side, which is located in a boat, with a GPS device. The main parameters to study are the power and overall performance of the system, and the channel differences.

To illustrate the power conditions at different distances, the Signal to Noise (SNR) ratio vs. subcarrier frequency is plotted for the different distances in Fig. 8.23. As it may be expected, the SNR decreases as higher is the distance. The underwater channel attenuation combined with the transducer frequency response affect the received signal, and due to that the higher frequencies are more attenuated than the lower ones.

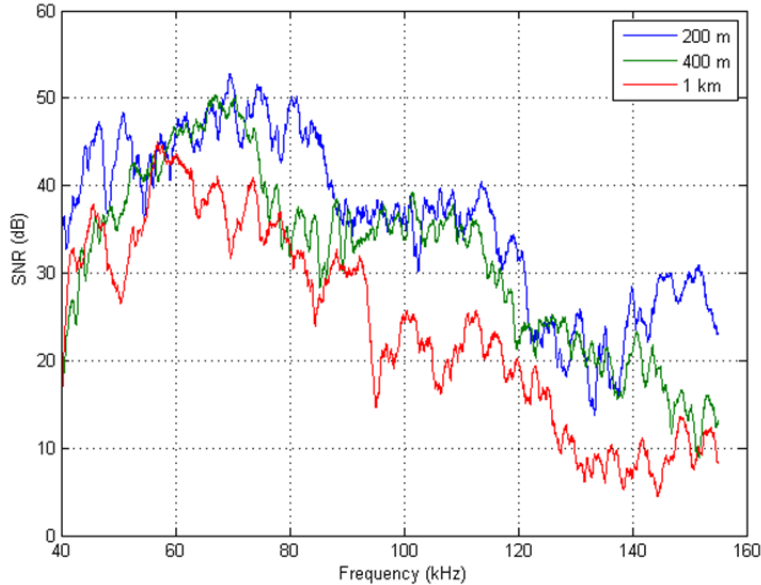


Figure 8.23: Average SNR in dB vs. frequency for different transmitter-receiver distances

To evaluate the overall performance, the MSE plot is shown in Fig. 8.24 for the attempted cases. The performance is close to the expected, as for higher distances the MSE is usually higher.

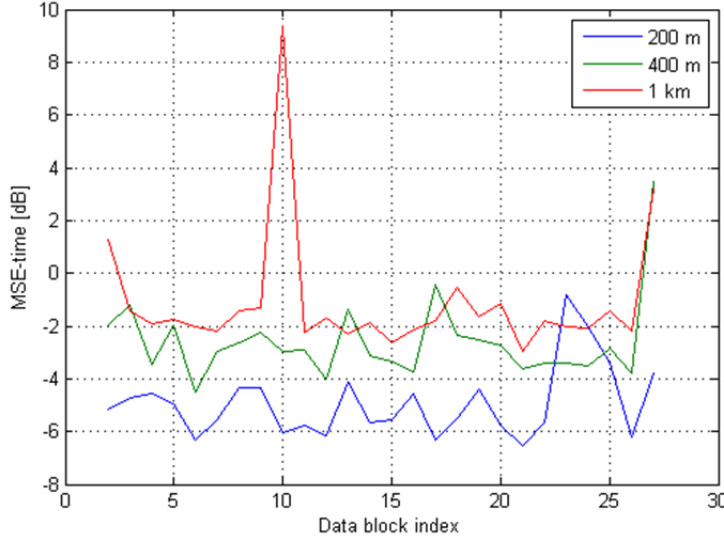


Figure 8.24: MSE-time in dB for different transmitter-receiver distances

In addition, the BER for different distances is evaluated and given in Fig. 8.25.

The trends are also the expected, with outstanding detection results for the 200-meter link, for which the decoded BER is zero. For the other cases, the BER is generally above  $10^{-3}$ , so 200 meters is selected as the maximum distance with the available hardware and practical channel conditions.

A comment about the channel conditions must be made for the 400-meter and 1-kilometer link. For these cases, a high degree of variation has been noticed from one run of tests to the next, due to the different location of the hydrophone (the location is approximately the same, but as the receiver is in a boat a different place may be chosen on different days).

### 8.3.5 Consistency

To finish the underwater experiments, a consistency study is done for the 200-meter link between transmitter and receiver. The 8-PSK constellation is chosen, and two types of BCH coding are used for the comparison: the  $\text{BCH}(63,18)$  and the  $\text{BCH}(63,30)$ . A number of consecutive video transmissions of several seconds (2.61 seconds for the lighter code and 4.14 seconds for the heavier code) are attempted, with a one-second difference between each other.

The consistency results are evaluated in terms of MSE and BER. The MSE plot is shown in Fig. 8.26, and the BER plot is provided in Fig. 8.27.

There is a correlation between the crossing of the two BCH types' lines in the MSE plot and the crossing of the coded BER curves, as the MSE provides an estimation of the detector performance. The decoded BER is always well below the targeted  $10^{-3}$  for the  $\text{BCH}(63,18)$ , while the  $\text{BCH}(63,30)$  is normally above this value.

The  $\text{BCH}(63,18)$  with 8-PSK in a 200 meters link can then be considered an appropriate choice, given

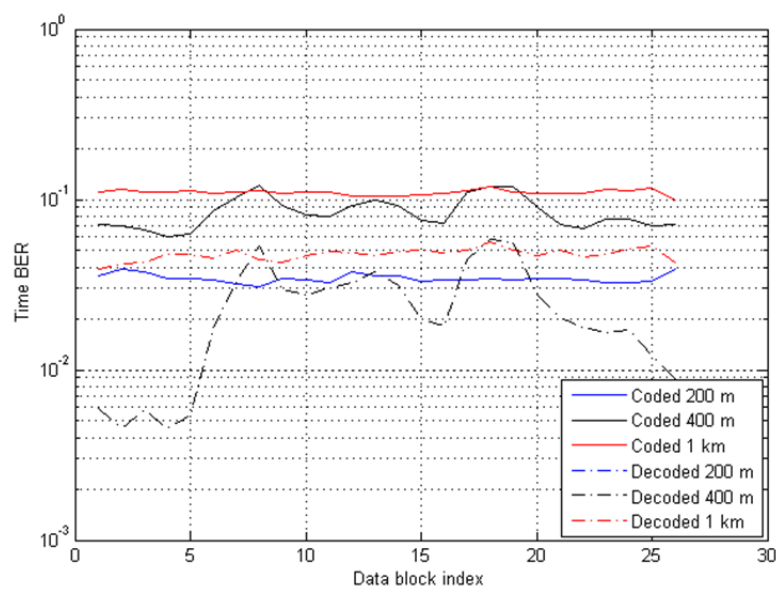


Figure 8.25: Time BER for different transmitter-receiver distances

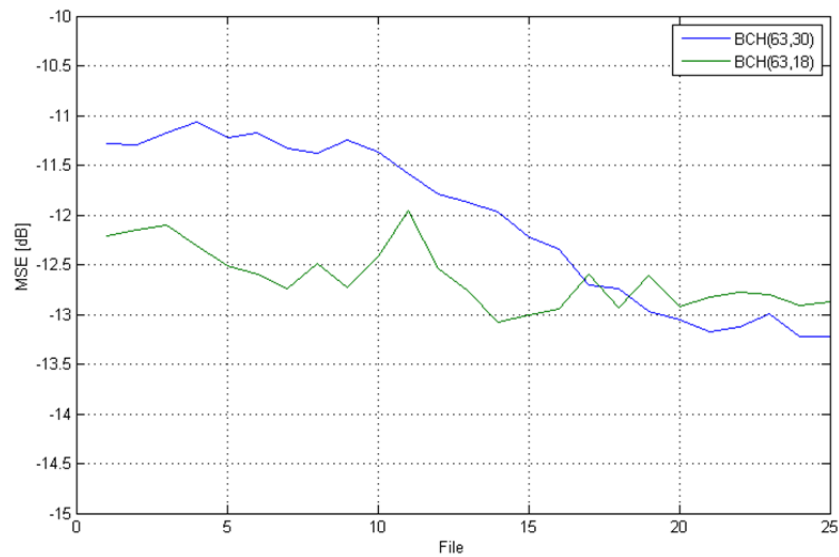


Figure 8.26: MSE-time in dB for 25 consecutive video transmissions

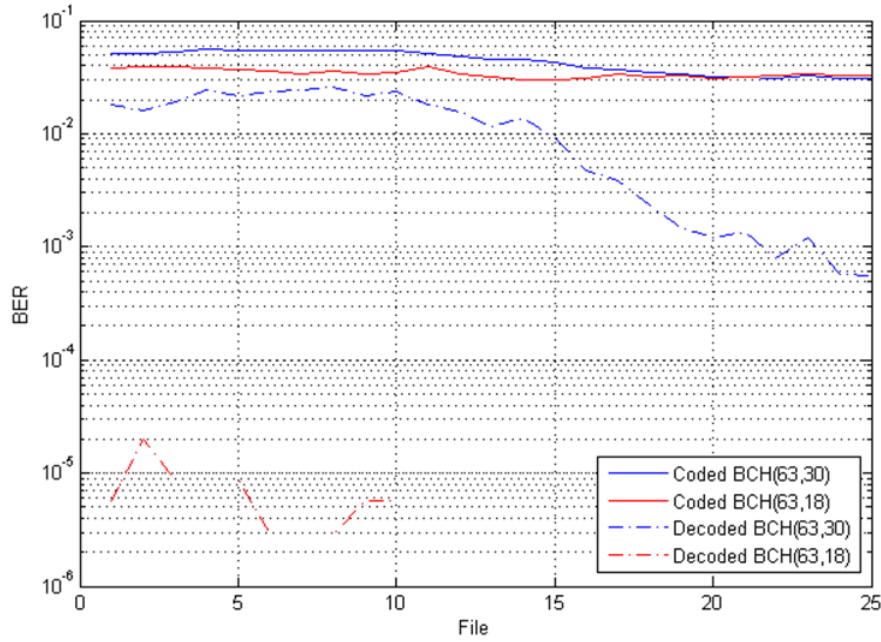


Figure 8.27: Time BER for 25 consecutive video transmissions

the consistent performance through time.

The data rate performance is also appropriate for the transmission of video data, as 91 kbps is achieved with the  $\text{BCH}(63,18)$ . The frame rate for a real-time transmission is set to about 12 fps for a low quality video (as it is commented in Sec. 3.3.2), providing a sufficient value to retrieve the motion of an underwater video, which is typically slow. If higher quality video is to be used, a decrease in the frame rate is required, as there is a compromise between frame rate and quality (this last dependent on resolution and MPEG-4 compression ratio).



# Chapter 9

## Conclusions and future work

In the light of the results from the experiments, some conclusions may be given about the success of the current research, according to the goals that were established for the project. These objectives were the transmission of video data at appropriate data rates, with satisfactory detection performance in a certain distance range.

Regarding the achieved data rates, the final OFDM system with the selected parameters exceeds the minimum 64 kbps bit rate for the transmission of the MPEG-4 low bit rate video. As a consequence of that, the goal is achieved.

With reference to the detection performance, the first video transmissions determined that a bit error rate (BER) lower than  $10^{-3}$  was necessary. The implemented system provides an even better BER than this established upper bound, which illustrates the success while qualitatively evaluating the detected files.

Finally, the distance range has been limited to 200 meters for an excellent and consistent detection. In spite of that, the performance of the system at higher distances may be better than the one suggested by the results, as the system is sensitive to channel changes. As a wide range of results was achieved for the 400-meter and 1-kilometer link, an appropriate selection of the location for the pair transducer-hydrophone might provide excellent results at these distances, too.

It must be also noted that, in contrast with previous experiments done in the field, a high bandwidth is used for the video data transmissions. The useful bandwidth is dependent on the link distance (as it is stated in Sec. 2.2.3), thus allowing the use of high frequency ranges for short distance links (in this case the maximum attempted distance is 1 kilometer).

After these few conclusions about the work, some issues to be treated in the future must be explained. They can be classified into two groups: the practical implementation modifications, and the software changes.

About the practical issues, some underwater testing is required with multiple receiving elements, as a typical underwater system has no less than 4 receivers. Furthermore, multiple transmitting elements can also be tested, in order to achieve either a higher data rate, or a better detection performance.

Further improvement can be achieved by stabilizing the transmitter-receiver setup, so that the best locations can be selected for the transducer and hydrophone. As it has been commented before, this could make a difference for the high distance cases.

Regarding the software implementation changes, online block processing must be considered in order to

directly retrieve the video data in the field, with no need for recording wavefiles and processing them offline, on the dock or in the laboratory.

Finally, some research on video compression techniques is necessary in the case that higher quality is targeted, as higher compression ratios will become indispensable, and the MPEG-4 technique cannot provide a much better compression performance than the one used in this work.

# Bibliography

- [1] M.Suzuki and T.Sasaki. Digital acoustic image transmission system for deep sea research submersible. *Proc. IEEE Oceans'92 Conference*, September 1992.
- [2] L.Berkhovskikh and Y.Lysanov. Fundamentals of ocean acoustics. *New York: Springer*, 1982.
- [3] R.Coates. Underwater acoustic systems. *New York: Wiley*, 1989.
- [4] J.Proakis T.Wang and J.Zeidler. Techniques for suppression of intercarrier interference in OFDM systems. *Wireless Communications and Networking Conference, IEEE, vol.1, pp.39-44*, March 2005.
- [5] M.Stojanovic. On the relationship between capacity and distance in an underwater acoustic communication channel. *Proc. First ACM International Workshop on Underwater Networks (WUWNet)*, September 2006.
- [6] M.Stojanovic. Capacity of a relay acoustic channel. *Proc. IEEE Oceans Conf.*, October 2007.
- [7] H.Ando J.Kojima, T.Ura and K.Asakawa. High speed acoustic data link transmitting moving pictures for autonomous underwater vehicles. *Proc. International Symposium on Underwater Technology*, April 2002.
- [8] M.Suzuki and T.Sasaki. Digital acoustic image transmission system for deep sea research submersible. *Proc. IEEE Oceans'92 Conference*, September 1992.
- [9] V.Ingle D.Hoag and R.Gaudette. Low bit-rate coding of underwater video using wavelet-based compression algorithms. *IEEE J. Oceanic Eng., vol. 22, pp. 393-400*, April 1997.
- [10] M.Stojanovic C.Pelekanakis and L.Freitag. High rate acoustic link for underwater video transmission. *Proc. IEEE Oceans'03 Conference*, September 2003.
- [11] G.Lapierre J.Trubuil and J.Labat. Real time transmission of images and data through underwater acoustic channel: The Trident system. *Proc. Geosciences and Remote Sensing Symposium*, 2004.
- [12] J.P.Beaujean. High-speed high-frequency acoustic modem for image transmission in very shallow waters. *Proc. IEEE Oceans Conf.*, June 2007.
- [13] Z.Weiquing et al. Signal processing for high speed underwater acoustic transmission of image (Marc 2007). *Proc. IEEE Oceans Conf.*, June 2007.
- [14] J.Catipovic M.Stojanovic and J.Proakis. Phase coherent digital communications for underwater acoustic channels. *IEEE Journal of Oceanic Engineering, vol.13, No.1, pp.100-111*, January 1994.
- [15] M.Stojanovic. Low complexity OFDM detector for underwater acoustic channels. *IEEE Oceans Conference*, September 2006.
- [16] M.Stojanovic. OFDM for underwater acoustic communications: Adaptive synchronization and sparse channel estimation. *Proc. International Conference on Acoustics, Speech, and Signal Processing (ICASSP'08)*, April 2008.

## BIBLIOGRAPHY

---

- [17] M.Stojanovic L.Freitag B.Li, S.Zhou and P.Willet. Multicarrier underwater acoustic communications over fast-varying channels. *IEEE Journal of Oceanic Engineering*, April 2008.
- [18] H.Wallace. Error detection and correction using the BCH code. 2001.
- [19] X.Li and L.J.Cimini. Effects of clipping and filtering on the performance of OFDM. *Communications Letters, IEEE*, vol. 2, no. 5, May 1998.
- [20] A.Jayalath and C.Tellambura. Reducing the peak-to-average power ratio of orthogonal frequency division multiplexing signal through bit or symbol interleaving. *Electronics Letters, vol. 36, no. 13*, June 2000.
- [21] B.Krongold and D.Jones. A new tone reservation method for complex-baseband PAR reduction in OFDM systems. *Acoustics, Speech and Signal Processing ICASSP'02*, 2002.
- [22] B.Krongold and D.Jones. An active-set approach for OFDM PAR reduction via tone reservation. *Signal Processing, IEEE Transactions, vol. 52, no. 2*, February 2004.
- [23] G.Rojo. Peak-to-average power ratio (PAR) reduction for acoustic OFDM systems. *Proc. IEEE Oceans'09 Conference, Biloxi, MS*, October 2009.
- [24] Firas Abbas Hamza. The USRP under 1.5X magnifying lens. *GNU Radio project*, June 2008.

# Appendix A

## User's manual

The designed OFDM system is implemented in MATLAB and Graphical User Interfaces (GUI) are created to facilitate the wavefile generation and demodulation process.

The different GUI that are included in the system are: the *WAV Generator*, which generates a wavefile for transmission; the *WAV Receiver*, which receives and demodulates the OFDM signals from a single (for a one receiver system) or multiple (for more than one receiver system) wavefiles; and the *WAV Plotter*, which plots signals from a transmitted or received wavefile.

Inside the main folder of the Acoustic Modem implementation, the GUI folder contains the different GUI that are described in this section.

### A.1 WAV Generator

The wavefile generator application aims at writing an OFDM signal to a wavefile to be transmitted to the selected channel. The GUI, input parameters, and output commands and files are explained in this section.

#### A.1.1 GUI

The designed GUI is shown in Fig. A.1. The different parameters must be selected in the checkboxes, pop-up menus, and written in the editable boxes.

#### A.1.2 Parameters

The GUI input parameters are explained in Tab. A.1.

Apart from the GUI parameters, other parameters may be changed in the implementation scripts. These are:

- Frequency range parameters: the operating frequency band is defined in the script *frequency-params.m*, which is located in the main folder of the Acoustic Modem system.

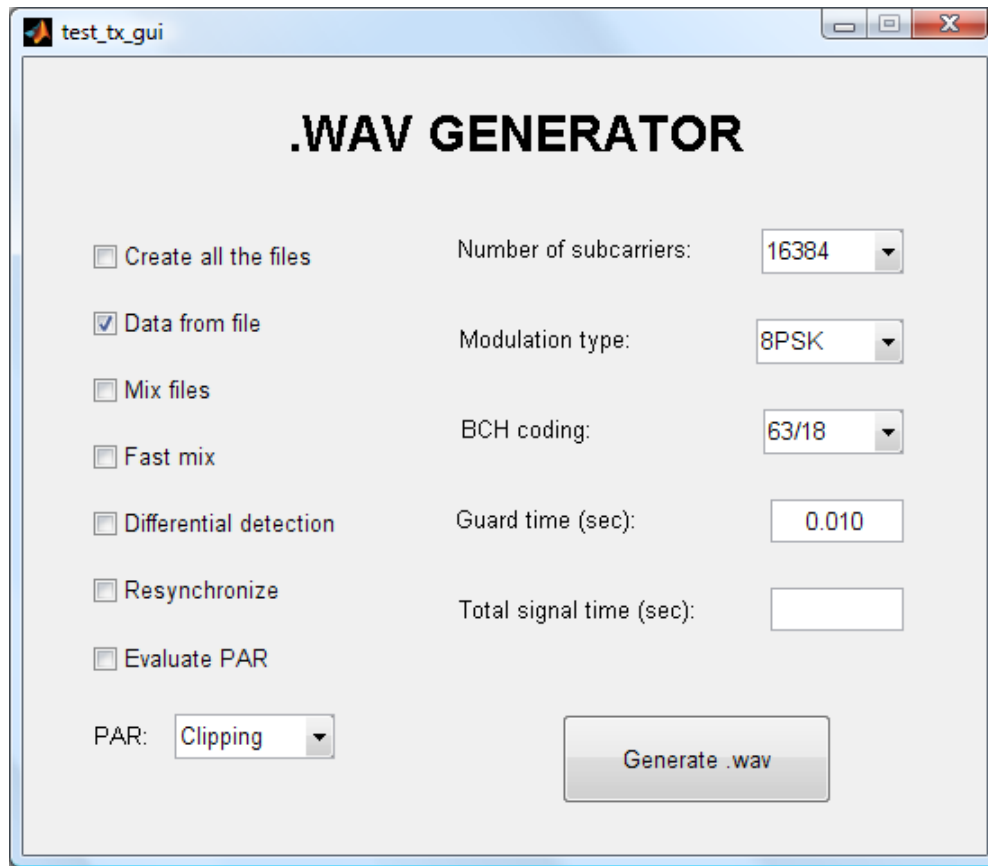


Figure A.1: WAV Generator GUI

Parameter	Input type	Explanation
Create all the files	Checkbox	Create all the defined BCH codings' files
Data from file	Checkbox	If checked, the data is taken from the chosen input file. If not checked, the data is taken from a random generator
Mix files	Checkbox	If checked, a mixed file containing the multiple BCH codings, separated in time, is created
Fast mix	Checkbox	If checked, a fast mixing process is performed. If not, a slow mixing for long signals is used
Differential detection	Checkbox	If checked, differential coding is used. If not, normal mapping is performed
Resynchronize	Checkbox	If checked, synchronization preambles are sent each 2 seconds
Evaluate PAR	Checkbox	If checked, a PAR evaluation plot is shown
PAR	Pop-up menu	PAR technique to be applied
Number of subcarriers	Pop-up menu	Number of subcarriers for the system, $K$
Modulation type	Pop-up menu	Subcarrier modulation type
BCH coding	Pop-up menu	BCH coding type
Guard time	Editable box	Guard time between OFDM blocks, in seconds
Total signal time	Editable box	Total signal time, if random data is used

Table A.1: WAV Generator input parameters

- Input data file: in the case that the data is from a file, the file that is used can be changed by running the file reader script. It is located in the *data* folder, and it is called *get\_file\_data.m*. The command line information has the following format:

```
Possible input files:
1) file_1
...
N) file_N
Choose input file: n
Reading file...
Done.
Generating scrambling sequence...
Done.
Scrambling...
Done.
Saving data...
Data saved.
```

where the possible input file names are shown from the files in the folder *data/input\_files* and the selection of one of them is followed by the scrambling of the file. The data is finally saved to be used for the transmission.

### A.1.3 Output

The command line output has the following format:

```
TEST X
*****Generating .wav*****
Total transmission time: x.xx sec
[1/6] Coding...
    Done.
[2/6] Mapping symbols in carriers...
    Block 1...Done.
    ...
    Block N...Done.
    Done.
[3/6] Creating signal...
    Synch block 1...
    Modulating...
        Block 1...Done.
        ...
        Block N...Done.
    Done.
    Adding synch...
    Done.
[4/6] Writing to file...
    Done.
[5/6] Evaluation and plots...
    Skipped.
[6/6] Filtering...
    Done.
Done.
```

And the generated files are located in the folder *sep\_tx*, for the separated BCH coding files, and the folder *sep\_rx*, in the case that some mixing is done. A sample *sep\_tx* folder is shown in Fig. A.2.

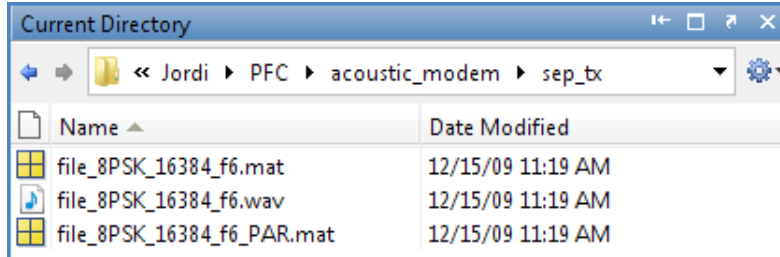


Figure A.2: Sample *sep\_tx* directory after wavefile generation

The *.wav* file contains the OFDM signal wavefile, and two *.mat* files are created: one for the data analysis, and another one for the PAR analysis.

#### A.1.4 Channel simulator

The channel simulator script is located in the *channel\_sim* folder, and it is called *channel\_simulator*. A sample command line output after the execution of the script is:

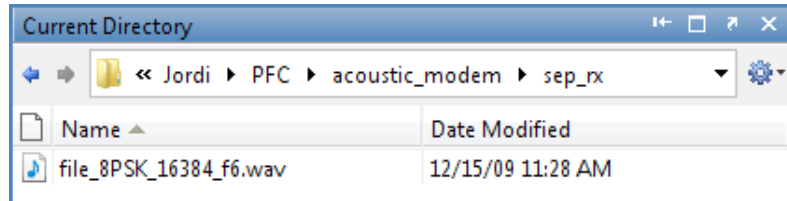
```
Possible input files:
1) filename_1.wav
...
F) filename_F.wav
Choose OFDM signal file: f
Add noise (0/1): 1
Possible input files:
1) noise_1.wav
...
N) noise_N.wav
Choose noise file: n
Add distance attenuation (0/1): 1
Distance (km): d
```

The possible input files are taken from the *sep\_tx* folder, and are offered for selection. The noise files must be stored in the *noise* folder to be detected by the application, and finally a distance parameter is requested for the attenuation.

The output wavefile is saved in the *sep\_rx* folder, under the same name than the one in the *sep\_tx* folder. A sample *sep\_rx* folder is shown in Fig. A.3.

## A.2 WAV Receiver

The wavefile receiver application is designed to take the OFDM received signal from one or multiple files (depending on the number of receivers), demodulate and decode the data. The GUI, input parameters, and output commands and files are explained in this section.

Figure A.3: Sample *sep\_rx* directory after channel simulation

### A.2.1 GUI

The designed GUI is shown in Fig. A.4. As in the generator GUI, the different parameters must be selected in the checkboxes, pop-up menus, and written in the editable boxes.

### A.2.2 Parameters

The GUI input parameters are explained in Tab. A.2.

Parameter	Input type	Explanation
Receive all the tests	Checkbox	Receive all the defined BCH codings' files
Data from file	Checkbox	If checked, the data is saved in a file. If not checked, the data is not saved
PAR	Pop-up menu	PAR technique that has been applied
Differential detection	Checkbox	If checked, differential coding is used. If not, normal mapping is performed
Separate tests	Checkbox	If checked, the mixed file is taken and the BCH types are separated. If not, the separated file is used
Resynchronize	Checkbox	If checked, synchronization pREAMbles are searched each 2 seconds
Invert signals	Checkbox	If checked, the signal is multiplied by $-1$
Make plots	Checkbox	If checked, the detection and analysis plots are shown
Save results	Checkbox	If checked, the results and plots are saved in the <i>results</i> folder
Number of subcarriers	Pop-up menu	Number of subcarriers for the system, $K$
Modulation type	Pop-up menu	Subcarrier modulation type
BCH coding	Pop-up menu	BCH coding type
Number of receivers	Pop-up menu	Number of receiving elements in the system
Output file extension	Pop-up menu	File extension for the received file
Guard time	Editable box	Guard time between OFDM blocks, in seconds
Total signal time	Editable box	Total signal time, if random data is used
Time to analyze	Editable box	Time to be analyzed, if partial detection is aimed

Table A.2: WAV Receiver input parameters

Regarding the *Invert signals* checkbox, it has been included to deal with the inversion of the transmitted signal by the USRP transmission Python script. Moreover, if partial detection is used and the specified time is larger than the file total length, full detection is applied.

Apart from the GUI parameters, other parameters may be changed in the implementation scripts. These are:

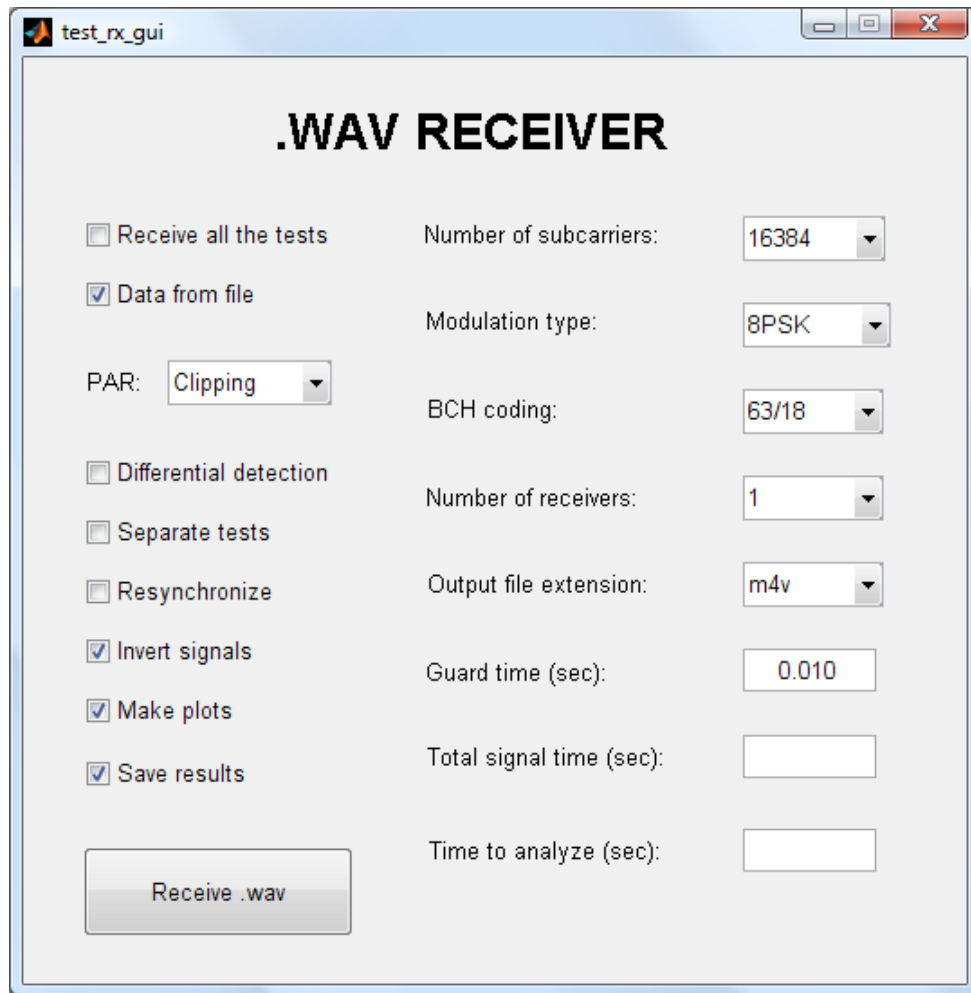


Figure A.4: WAV Receiver GUI

- Frequency range parameters: as for the *WAV Generator* application, the operating frequency band is defined in the script *frequency\_params.m*, which is located in the main folder of the Acoustic Modem system.
- Detector parameters: the detector parameters such as channel thresholds, update equations' coefficients or overlap-add coefficients can be modified in the file *data\_type.m*, which is also located in the main folder of the Acoustic Modem implementation.

### A.2.3 Output

The command line output has the following format:

```
*****Receiving ./sep_rx/filename*****
[1/3] Acquiring symbols...
    Filtering receiver 1/Nr...
    Filtering done.
    Synchronizing receiver 1/Nr...
    Synchronization done.
    Demodulating receiver 1/Nr...
    Demodulation done.
    ...
    Filtering receiver Nr/Nr...
    Filtering done.
    Synchronizing receiver Nr/Nr...
    Synchronization done.
    Demodulating receiver Nr/Nr...
    Demodulation done.
[2/3] Post-FFT detecting (PAR_type=P, Differential=D)...
    Part 1/1...
        Initializing...
        Done.
        Detecting block 1 of N...
        Done.
        ...
        Detecting block N of N...
        Done.
    Post-FFT detection done.
[3/3] Saving data...
    Data saved.

Rx done.

*****Analyzing data ./sep_rx/filename*****
[1/2] Plotting detection results...
    Detection results plotted.
[2/2] Analyzing performance...
    * Part 1/1:
    Decoded data length: D1 bytes
    Coded data length: C1 bytes
    BER after decoding: x.xxxxxxx
    BER before decoding: x.xxxxxxx
    Average MSE: x.x dB
```

where the  $N_r$  receivers are filtered (the filtered wavefile is saved in the *sep\_rx* folder), synchronized and demodulated. After the detection, an analysis is performed indicating data lengths in bytes, bit error rates (BER), and an average MSE.

The synchronization algorithm outputs the details as in Fig. A.5. Once the synchronization performance is shown, the algorithm continues with the detection.

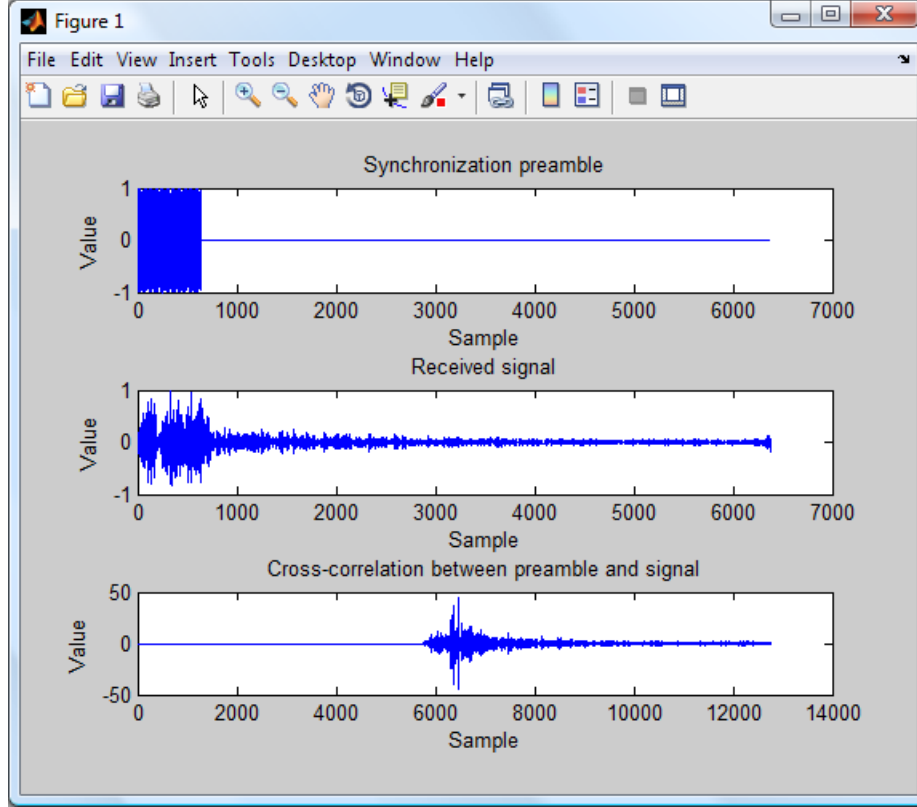


Figure A.5: Synchronization plot

The output plots are the ones shown in Fig. A.6 and Fig. A.7.

Finally, if the results are saved, they are located in the *results* folder as shown in Fig. A.8.

## A.3 WAV Plotter

The wavefile plotter is an application that allows the user to generate the plots of the OFDM signals that are transmitted and received. The file names must not be changed from the transmitted signal notation, so that the application finds the wavefiles in the corresponding directories (*sep\_tx* and *sep\_rx* folders).

### A.3.1 GUI

The designed GUI is shown in Fig. A.9. As in the previous GUI, the different parameters must be selected in the checkboxes, pop-up menus, and written in the editable boxes.

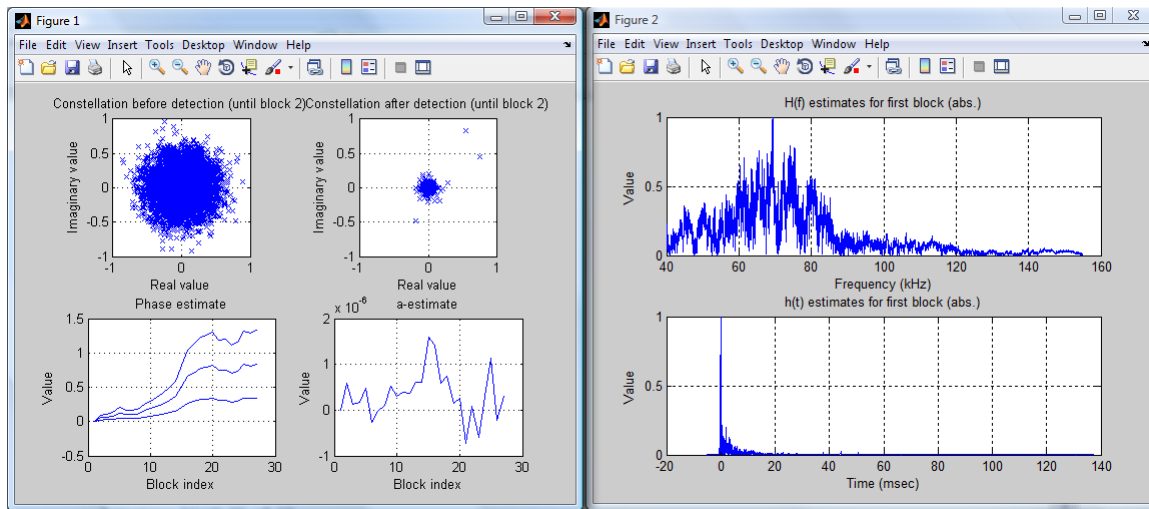


Figure A.6: Detection results (left) and channel estimates (right)

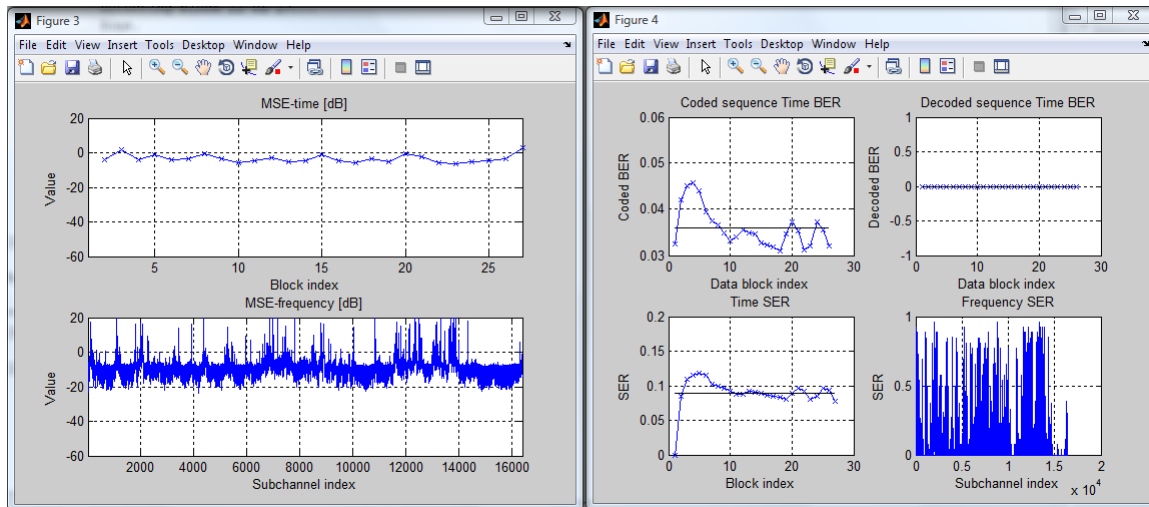
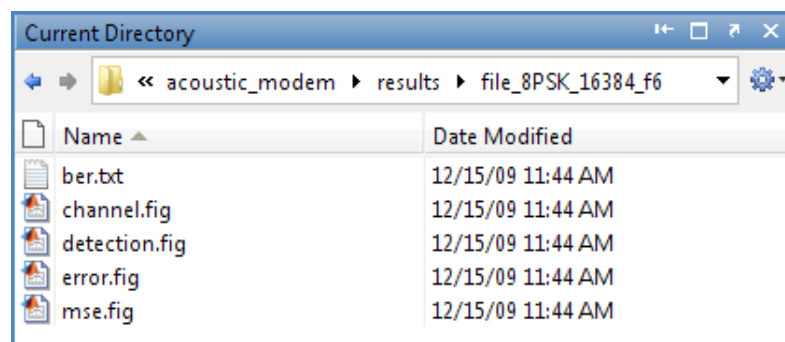


Figure A.7: MSE results (left) and error performance (right)

Figure A.8: Sample *results* directory after detection and saving

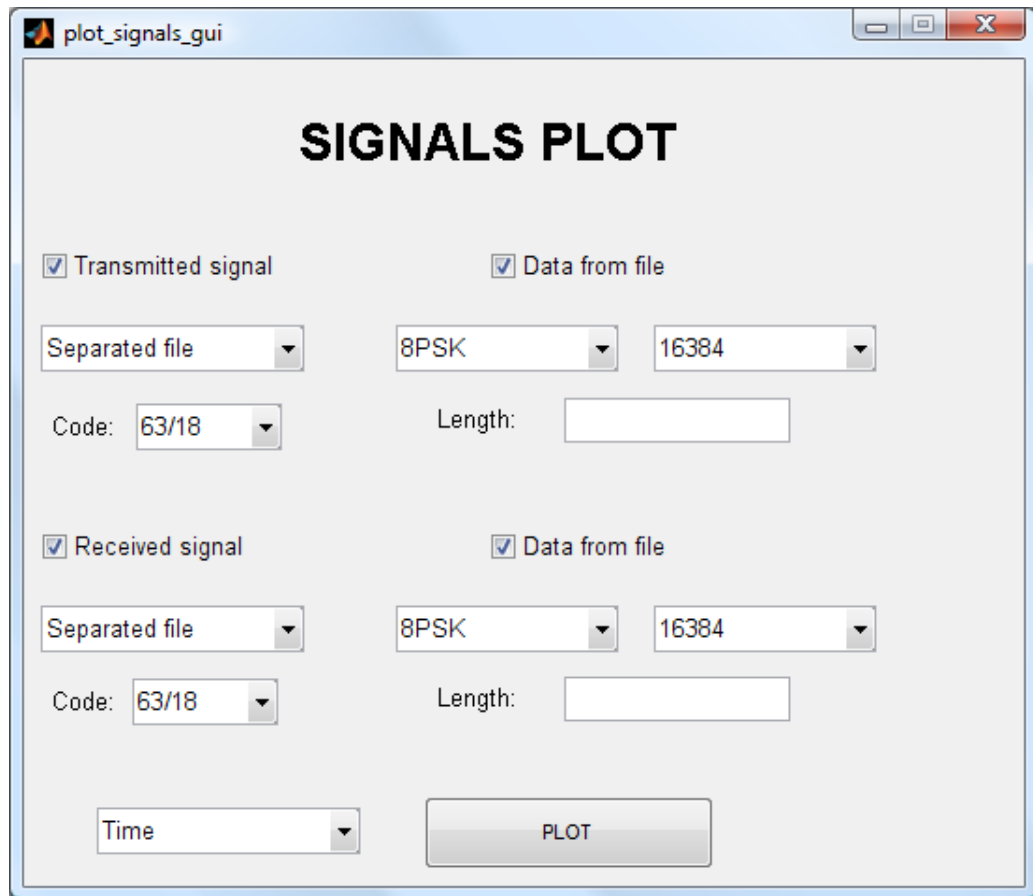


Figure A.9: WAV Plotter GUI

### A.3.2 Parameters

The GUI input parameters are explained in Tab. A.3.

<i>Parameter</i>	<i>Input type</i>	<i>Explanation</i>
Transmitted signal	Checkbox	Plot a signal from the <i>sep_tx</i> folder
Received signal	Checkbox	Plot a signal from the <i>sep_rx</i> folder
Data from file	Checkbox	If checked, the data is from a file. If not checked, the data is randomly generated
File type	Pop-up menu	The type of file (single coding type or coding types mix)
Modulation type	Pop-up menu	Subcarrier modulation type
Number of subcarriers	Pop-up menu	Number of subcarriers for the system, $K$
Code	Pop-up menu	BCH coding type
Length	Editable box	Length (samples or time) to be shown
Horizontal axis	Pop-up menu	Horizontal axis units (time -seconds-, or samples)

Table A.3: WAV Plotter input parameters

In the case that the length to be plotted is higher than the maximum length, a full signal plot is shown.

### A.3.3 Output

The wavefile plotter outputs a plot with the selected files' signals in the time or sample domain, as shown in Fig. A.10. In this example, a transmitted and received OFDM signal can be seen in the time domain.

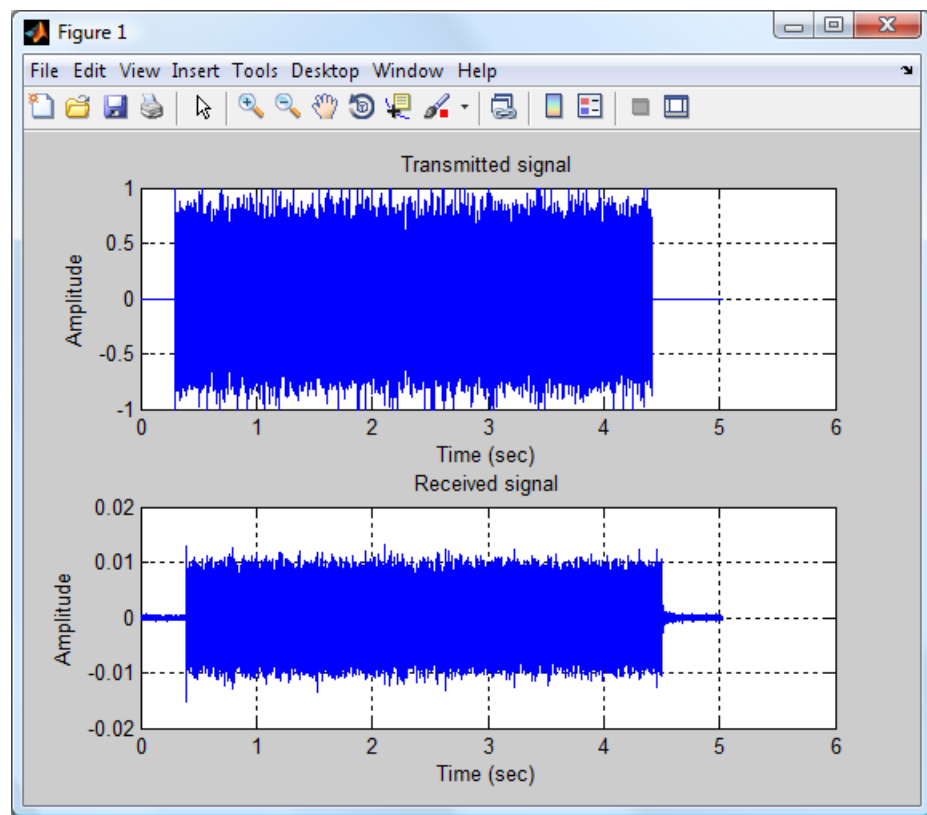


Figure A.10: Plotted OFDM signals